DISSERTATION

THE MADDEN JULIAN OSCILLATION AND TROPICAL-EXTRATROPICAL TELECONNECTIONS

Submitted by

Kai-Chih Tseng

Department of Atmospheric Science

In partial fulfillment of the requirements

For the Degree of Doctor of Philosophy

Colorado State University

Fort Collins, Colorado

Summer 2019

Doctoral Committee:

Advisor: Elizabeth A. Barnes
Co-Advisor: Eric D. Maloney

David A. Randall
Imme Ebert-Uphoff

ABSTRACT

THE MADDEN JULIAN OSCILLATION AND TROPICAL-EXTRATROPICAL TELECONNECTIONS

The Madden Julian Oscillation (MJO) excites strong variations in extratropical circulations that have important implications for subseasonal-to-seasonal (S2S) prediction. In particular, certain MJO phases are characterized by a consistent modulation of geopotential height patterns in the North Pacific and North America. Although the MJO's influence in the downstream weather has been widely explored in previous studies, the relationship between robust MJO teleconnection patterns and model prediction skills has received little attention. In this study, the reanalysis data and ensemble hindcasts from numerical weather forecast system are used to quantify the influence of robust MJO teleconnection on model prediction skills.

By calculating the pattern consistency of MJO teleconnection, the ability of MJO convection to modulate extratropical weather is quantified over different time lags and phases. The diagnostic result demonstrates that the robust MJO teleconnection in specific MJO phases/lags are also characterized by excellent agreement in the prediction of geopotential height anomalies across model ensemble members at forecast lead of up to 3 weeks. The mechanisms that lead some MJO phases to have more consistent teleconnections than others are examined by using a linear baroclinic model (LBM). The simulation results show that MJO phases 2, 3, 6 and 7 consistently generate Pacific-North America like (PNA-like) pattern on S2S timescales while other phases do not. By employing a Rossby wave source analysis, the result shows that a dipole-like Rossby wave source patterns on each side of the jet in MJO phase 2, 3, 6 and 7 can increase the pattern consistency of teleconnection due to the constructive interference of similar teleconnection signals. On the other hand, the symmetric patterns of Rossby wave source in other phases can dramatically reduce the pattern consistency due to destructive interference.

The consistency of MJO teleconnections is also characterized by an interannual variability. During the El Niño years, the pattern consistency is dramatically decreased compared to the La Niña years. Employing the numerical experiments in LBM and applying a Rossby wave ray tracing algorithm, we demonstrate two factors largely determine the interannual variability of MJO teleconnection consistency. During El Niño years, the eastward extension of subtropical jet and a less-dipole like Rossby wave source pattern on each side of the jet dramatically decrease poleward propagating wave signals. By contrast, the competing effect

between these two factors results in modest changes in pattern consistency during La Niña years. Thus, the observed consistency of MJO teleconnections is much smaller during El Niño years than La Niña years.

The dynamics associated with the pattern consistency of MJO teleconnection are addressed in the first half of this work. What is still unclear, however, is the importance of the accumulated influence of past MJO activity on these results. To examine the importance of past MJO phases in determining future states of extratropical circulations, a LBM and one of the simplest machine learning algorithm: logistic regression are used. By increasing the complexity of logistic regressions with additional informational about past MJO phases, we show that 15 additional lags before lag 0 play a dominant role in determining the future state of MJO teleconnections. This result is supported by the numerical LBM simulations. We further demonstrate that this 15-day span is characterized by a phase/lead time dependent feature, which is relevant to the dynamics of MJO teleconnections and explained in this work.

Ultimately, a particular emphasis is placed on the role of model MJO in influencing the winter climatology of extratropical circulations. The MJO is known for consistently modulating the extratropical weather. In addition, simulating the MJO continues to be a challenge for many state-of-art climate models, and it is unclear the extent to which these biases in the MJO may cause biases in midlatitude variability. By analyzing 22 climate model simulations from the Coupled Model Intercomparison Project Phase 5 (CMIP5) and the reanalysis data, we demonstrate that one of leading variability of daily geopotential height is associated with MJO activity, and can be identified without prior knowledge of MJO in both observations and CMIP5 data. This shows the dominant role of MJO in modulating extratropical circulations. However, due to this strong relationship between MJO and extratropical circulations, the model biases in the MJO convection is also reflected in the wintertime climatology of extratropical circulations.

TABLE OF CONTENTS

LIST OF TABLES

LIST OF FIGURES

CHAPTER 1

Introduction

The Madden Julian oscillation (MJO) is one of the dominant mode of variability in the tropics characterized by planetary scale circulations (zonal wave number 1-3) and intraseasonal time scales (20-100 days, *Adames and Kim* (2016)). Since the first documentation of MJO in the early 1970s (*Madden and Julian* 1971), its important role in influencing the global circulations has drawn a lot of attention from scientific communities. In the tropics, MJO is observed to virtually influence the initiation of El Niño- Southern oscillation (ENSO,*Moore and Kleeman* (1999)), the intraseasonal variability of Asia and Australia summer monsoon (*Lawrence and Webster* 2002; *Wheeler et al.* 2009), the tropical cyclone genesis in Pacific and Atlantic (*Maloney and Hartmann* 2000; *Ching et al.* 2010), the precipitation in Amazon rain forest (*Souza and Ambrizzi* 2006) and the diurnal storms in the Maritime Continents(*Kanamori et al.* 2013). In addition to tropics, the MJO's influence is spanning over extratropical regions through tropical-extratropical teleconnections. Previous studies have demonstrated the extratropical weather, including some extreme phenomena, are strongly modulated by MJO activities such as the intensity of annular modes in both hemispheres(*Flatau and Kim* 2013), the frequency of hail storms and tornadoes over the great plain(*Baggett et al.* 2018), the occurrence of anti-cyclonic blocking (*Henderson et al.* 2016) and atmospheric rives along the west coast of North America (*Mundhenk et al.* 2016).

1.1 DYNAMICS OF MJO TELECONNECTION

In this work, a particular emphasis is devoted to MJO's extratropical influence. The large-scale tropical heating in generating the extratropical response has been extensively examined since the early 1980s (*Hoskins and Karoly* 1981; *Wallace and Gutzler* 1981). By analyzing the reanalysis data and conducting numerical experiments, the coherent variation between tropical heating and extratropical geopotential height is documented (*Bjerknes* 1969; *Simmons et al.* 1983). A number of mechanisms are proposed to explain the initiation and the growth of these extratropical responses, including the barotropic conversion by the interaction between heating-induced divergent flow and the subtropical jet (*Simmons et al.* 1983) or the dynamical feedback between synoptic eddies and low-frequency variability (*Held et al.* 1988; *Jin et al.* 2006). While most of these studies focused on stationary forcing (e.g. ENSO) and steady-state response, scientists have

been also investigating the relationship between MJO and associated teleconnection signals. By conducting objective analysis (e.g. lag regression,*Black* (1997); *Matthews et al.* (2004)) and idealized simulations on linearized barotropic vorticity equation forced by a propagating MJO forcing (*Ferranti et al.* 1989), the dominant unstable modes of extratropical response is discovered (e.g. Pacific-North America pattern). With a detailed vorticity budget analysis, *Mori and Watanabe* (2008) further demonstrates the linear dynamics explain most of the triggering and growing process of the MJO-induced extratropical variability.

1.2 THE CONSISTENCY OF MJO TELECONNECTION PATTERNS

The MJO has long been recognized as one of the most important source of predictability on subseasonal-to-seasonal timescales (S2S, 2-5 weeks,*Hamill and Kiladis* (2014)), which fills the gap of low prediction skills from the traditional perspective of mid-latitude medium range weather forecast(*Vitart et al.* 2017). However, previous studies have demonstrated that the MJO's modulation in the extratropical weather is characterized by a MJO phase-dependent feature due to the circumnavigating nature of MJO convection (*Henderson et al.* 2016; *Seo and Lee* 2017). The MJO heating periodically changes the sign in the regions from Indian ocean to warm pool Pacific, which is also reflected in the tropical-extratropical teleconnections. This feature introduces additional uncertainty for leveraging the MJO for S2S predictions. Thus, even steady progress in the knowledge of MJO teleconnections has been made in the past decades, what is still unclear, is the relationship between the phase-dependent, consistent modulation of MJO teleconnection and model prediction skills. Taking this question as the start point, we thoroughly examine the consistency of MJO teleconnection patterns from different perspectives including observational diagnosis, predictions and mechanisms in this thesis.

1.3 SCOPE OF THIS WORK

There are seven chapters of research in this dissertation.

In chapter 2, a diagnostic metric, pattern consistency, is developed to quantify the similarity of teleconnection patterns over different MJO events and forecast lead time. By analyzing the operational hindcasts from the numerical weather forecast systems, we explore the connection between this diagnostic metric and the prediction skills of extratropical geopotential height. We further demonstrate that MJO teleconnection pattern consistency is characterized by a phase-dependent feature, which is also reflected in the model prediction skills of extratropical geopotential height. The work in this chapter is published in *Geophysical Research Letter* as

- Tseng, K. -C., E. A. Barnes and E. D. Maloney, 2018: Prediction of the midlatitude response to strong Madden-Julian oscillation events on S2S timescales. *Geophys. Res. Lett.*, **45**, 463–470.

Chapter 3 examines the physical mechanisms that lead some MJO phases to have more robust teleconnection signals using a linear baroclinic model (LBM). By employing ensemble simulations in the LBM, we demonstrate the phase-dependent feature of MJO teleconnection pattern consistency observed in reanalysis data can be reproduced, which implies the essential role of linear Rossby wave dynamics in responsible for this phase-dependent pattern consistency. A Rossby source analysis is conducted and shows that a constructive (destructive) interference by the teleconnection signals emanating from each side of the subtropical jet is responsible for a more (less) robust MJO teleconnection patterns in specific phases. The work in this chapter is published in *Journal of Climate* as:

- Tseng, K., E. Maloney, and E. Barnes, 2019: The consistency of MJO teleconnection Patterns: an explanation using linear Rossby wave theory. *J. Climate*, **32**, 531–548

Chapter 4 examines the interannual variability of MJO teleconnection pattern consistency. Specifically, we try to answer the question: how does ENSO modulate the pattern consistency of MJO teleconnections through changing the basic state patterns (e.g. the subtropical jet) and the MJO forcing? Employing the numerical experiments in a LBM and applying a Rossby wave ray tracing algorithm, we demonstrate two competing factors (1) the meridional shift of the ray path and (2) the interannual variability of Rossby wave source pattern largely determine the changes in MJO teleconnection pattern consistency on interannual timescales. This work will be submitted to *Journal of Climate* as :

- Tseng, K-C., E. Maloney, and E. Barnes, 2019: The consistency of MJO teleconnection patterns on interannual timescales. *J. Climate*, to be submitted

The dynamics in responsible for the phase-dependent pattern consistency of MJO teleconnections are examined in chapter 3 and 4. What is unclear, however, is the accumulated influence of past MJO on the future evolution and the predictability of extratropical circulations. Chapter 5 explores this question by using a LBM and one of the simplest machine learning algorithm: logistic regression. We show that 15 days before lag 0 (e.g. initial day for forecast) plays a dominant in determining the future state of MJO teleconnections. However, this 15-day timescale strongly depends on the past MJO phases. A physical explanation is also provided in this chapter. The work in this chapter will be submitted to *Journal of Climate* as:

- Tseng, K-C., E. A. Barnes, and E. D. Maloney, 2019: The importance of past MJO activity in determining the future state of the midlatitude circulation. *J. Climate*, to be submitted

In chapter 6, we return to a basic but unanswered question: How important the MJO is compared to other drivers of extratropical variability ? By analyzing the observational reanalysis and 22 climate models from Coupled Model Intercomparison Project Phase 5 (CMIP5), we demonstrate MJO is the dominant driver for daily extratropical geopotential height variability around North Pacific in both observational data and climate model output. Due to MJO's strong modulation in the extratropical circulations, the result further shows that the model biases in MJO convection is reflected in the winter climatology of extratropical geopotential height variance. The work in this chapter will be submitted to *Journal of Geophysical Research- Atmospheres* as:

- Tseng, K-C., E. A. Barnes, and E. D. Maloney, 2019: The dominant role of the MJO for extratropical variability in observations and the CMIP5 climate models. *JGR-Atmospheres*, to be submitted

Ultimately, chapter 7 summarizes the result and shortcoming of this dissertation. Chapter 7 also provides the discussions for future work.

CHAPTER 2

Prediction of the midlatitude response to strong Madden-Julian oscillation events on S2S timescales [1]

The Madden Julian Oscillation (MJO) forces strong variations in extratropical atmospheric circulations that have important implications for subseasonal-to-seasonal prediction. In particular, certain MJO phases are characterized by a consistent modulation of geopotential height in the North Pacific and adjacent regions across different MJO events. Until recently, only limited research has examined the relationship between these robust MJO tropical-extratropical teleconnections and model prediction skill. In this study, reanalysis data and numerical forecast model ensemble hindcasts are used to demonstrate that robust teleconnections in specific MJO phases and time lags are also characterized by excellent agreement in the prediction of geopotential height anomalies across model ensemble members at forecast leads of up to 3 weeks. These periods of enhanced prediction capabilities extend the possibility for skillful extratropical weather prediction beyond traditional 10-13 day limits.

2.1 INTRODUCTION TO THE PREDICTION OF MJO TELECONNECTIONS

The traditional view of midlatitude numerical weather prediction maintains that the nonlinear growth of errors from uncertainty in initial conditions, or deficiency of physical processes in numerical models, makes weather unpredictable beyond a 10-13 day lead time (e.g. *Hamill and Kiladis* (2014)). Nevertheless, an increasing number of studies have demonstrated that information from lower-frequency variability (lower frequency refering to a period longer than about 7 days), such as the seasonal cycle, land processes, or air-sea interactions can extend model prediction skill beyond this traditional predictability limit (*Chen and Dudhia* 2001; *Infanti and Kirtman* 2016; *Jin et al.* 2014). Among these low-frequency time scales, subseasonal-to-seasonal (S2S hereafter) timescales are of particular interest not only because we have less confidence in prediction at these time scales (*Vitart* 2014), but also because they serve as a bridge between weather and climate.

The Madden Julian oscillation (MJO) is an equatorial propagating convective envelope characterized by periods of 30-90 days (*Adames and Kim* 2016; *Hendon and Salby* 1994), a band that fortuitously occurs in

[1] This chapter contains material that has been published in the *Geophysical Research Letter* as: Tseng, K. -C., E. A. Barnes and E. D. Maloney, 2018: Prediction of the midlatitude response to strong Madden-Julian oscillation events on S2S timescales. *Geophys. Res. Lett.*, **45**, 463–470.

the S2S window with lower traditional prediction skill. A particular motivation for improving S2S prediction is that some of the most persistent and impactful weather phenomena in mid-latitudes (e.g. blocking anticyclones (*Berggren et al.* 1949; *Masato et al.* 2012) or extratropical storms) are associated with low-frequency variations of geopotential height, which can be driven by tropical-extratropical teleconnections. MJO-related teleconnections have significant impacts on S2S-timescale geopotential height anomalies in the mid-latitude Pacific and North America, which consequently modulate the weather patterns of those regions (*Henderson et al.* 2017; *Seo and Lee* 2017). For example, previous research has shown that when the MJO exhibits enhanced convection in the western Pacific and suppressed convection in the eastern Indian Ocean, positive geopotential height anomalies generated by stationary Rossby waves occur in the Gulf of Alaska, which can dramatically increase the occurrence of blocking (*Henderson et al.* 2016). Further, some studies have shown that improved MJO forecasts have positive impacts on midlatitude weather forecasts (*Hendon et al.* 2000; *Vitart and Molteni* 2010).

Understanding the teleconnected response of the MJO does present challenges, however. The MJO is a circumnavigating system and the teleconnection signal takes time to propagate to the mid-latitudes. Hence, a location in the midlatitudes may exhibit a teleconnected response that was initiated by tropical convective heating in an earlier phase of the MJO. The highly varied features of the MJO combined with its teleconnections make it difficult to quantify the MJO's influence over different phases and lead times, an issue especially important for midlatitude prediction. Thus, although there have been a numerous studies showing how MJO-related teleconnections modulate mid-latitude regions (*Henderson et al.* 2017; *Kim et al.* 2006; *Seo and Lee* 2017), studies illustrating the MJO teleconnection influence on the forecast skill of numerical weather prediction models in the North Pacific and adjacent regions are still limited.

Here, we demonstrate that while some MJO phases produce robust teleconnections in the midlatitudes, others do not. By robust, we mean generating consistent patterns over different events. This result is shown in reanalysis data and its implications for S2S forecasting are demonstrated using a hindcast ensemble from the European Centre for Medium-Range Weather Forecasts (ECMWF) forecast model. Specifically, MJO phases in which tropical-extratropical teleconnections are more robust at lead times of 2-3 weeks in the reanalysis are also the phases that offer improved prediction of the North Pacific midlatitude circulations in the ECMWF ensemble forecast system.

2.2 DATA AND METHODS

2.2.1 Data

This study uses daily 500 hPa geopotential height (Z500) from Modern-Era Retrospective Analysis for Research and Applications (MERRA hereafter) (*Rienecker et al.* 2011) and ECMWF ensemble hindcasts (*Vitart et al.* 2017). The ensemble hindcasts were acquired from ECMWF's S2S data library established by the World Weather Research Program/World Climate Research Program (WWRP/WCRP), which includes 11 different hindcast models. The ECMWF ensemble hindcast system is the most ideal model for our research because it has the second most ensemble members and reforecasts frequently enough for MJO events sampling (4 times/week). All of the datasets mentioned above were interpolated to daily time scales and 2.5^o by 2.5^o horizontal resolution.

Since the MJO teleconnection signals are stronger in boreal winter over the North Pacific, we only use the data in the extended boreal winter (November-March) from 1979-2015 for MERRA. To remove the influence of the annual cycle, we first calculate the daily climatology of Z500 and define the annual cycle as the first three harmonics of this time series. Anomalies are computed by subtracting the annual cycles from the raw Z500. For the ECMWF ensemble hindcast (10 perturbed ensemble members), the Z500 is pre-processed in the same way as reanalysis data where the daily climatology is derived from the ensemble mean as a function of lag. The hindcast data covers the period from 1999 to 2015. In this study, the MJO phase is defined by the OLR MJO index (OMI) (*Kiladis et al.* 2014) and only days with an amplitude of OMI greater than one standard deviation are included in the composites.

2.2.2 Methods

The composited anomalous Z500 is derived by averaging anomalies for days with OMI amplitude greater than one standard deviation at lag zero over different MJO phases and time lags. In the reanalysis, the sample sizes for the eight MJO phases (in order from 1 to 8) are 388, 415, 426, 435, 352, 430, 441 and 429 (and 2265 days for non-MJO events). If the amplitudes of the OMI are consecutively greater than one standard deviation, they are considered as one event (each phase is accounted for separately). The total number of event for each MJO phase (in order from 1 to 8) are 100, 107, 103, 102, 106, 108, 103 and 106, respectively. To assess statistical significance, a bootstrapping analysis is employed. We randomly choose days in the extended boreal winter (November-March) from 1979-2015 based on the number of MJO events in each of the eight phases. By averaging the Z500 for randomly selected days based on these numbers, and

repeating this process 500 times, we can approximate the distribution of the sample mean. Then, the 95% confidence bounds on the geopotential height anomalies are determined from this distribution (*Wilks* 2011).

We quantify the pattern robustness over different events by calculating the area-weighted anomaly correlations between two maps. The pattern robustness is then defined as the fraction of pairs with correlation greater than 0.5, although conclusions are not sensitive to this threshold. For the pattern correlations, a similar significance test is employed to approximate the distribution of the percentage of pairs with high correlation coefficients. Details of the preprocessing of the data for Figure 2.3 is given in the main text.

2.3 RESULTS

2.3.1 Pattern consistency of the teleconnected Z500 in MERRA reanalysis

Figure 2.1 shows a composite map of Z500 for the extended boreal winter. Each panel denotes a different MJO phase and/or time lag where an n-day lag represents n days after the given MJO phase. Dotted regions indicate anomalies that are significantly different from zero at the 95% level based on a bootstrapping analysis (see section 2.2). In Figure 2.1, the spatial pattern of Z500 with significant tropical-extratropical teleconnection signals (dotted regions), such as phase 2, lag 10-14 or phase 3, lag 5-9, shows a wave-train structure with three centers located in the North Pacific, the Gulf of Alaska and the eastern U.S., which have been documented in many previous numerical and observational studies (e.g. *Hoskins and Karoly* (1981); *Wallace and Gutzler* (1981); *Kim et al.* (2006); *Henderson et al.* (2016)). These signals initiate from the mid-latitude Pacific in a region of high pressure anomalies (e.g. phase 2, lag 5-9) and then low pressure anomalies in the the Gulf of Alaska and the U.S. west coast subsequently strengthen (e.g. phase 2, lag 10-14), which highlights the vital role of MJO anomalous heating in connecting low- and mid-latitude regions. Since the MJO is a circumnavigating system on the equator, where one phase is often followed by the next phase and each phase typically lasts for 3-5 days, some similarity of composite patterns occurs along diagonals in Figure 2.1 from the upper right to the lower left (e.g. phase 2, lag 10-14 is similar to phase 3, lag 5-9). A nearly identical, but opposite, teleconnection pattern can be observed in phase 7 and phase 8 compared with phase 2 and phase 3, caused by opposite-signed MJO anomalous heating in the tropics.

Figure 2.1 shows that the composited amplitude of Z500 exhibits larger areas of significance over specific MJO phases and lags. There are a couple reasons why this could be the case: (1) the strong Z500 variations are dominated by only a few MJO events, or (2) certain phases of the MJO produce more consistent Z500 patterns compared to other MJO phases. The latter is more beneficial than the former for weather

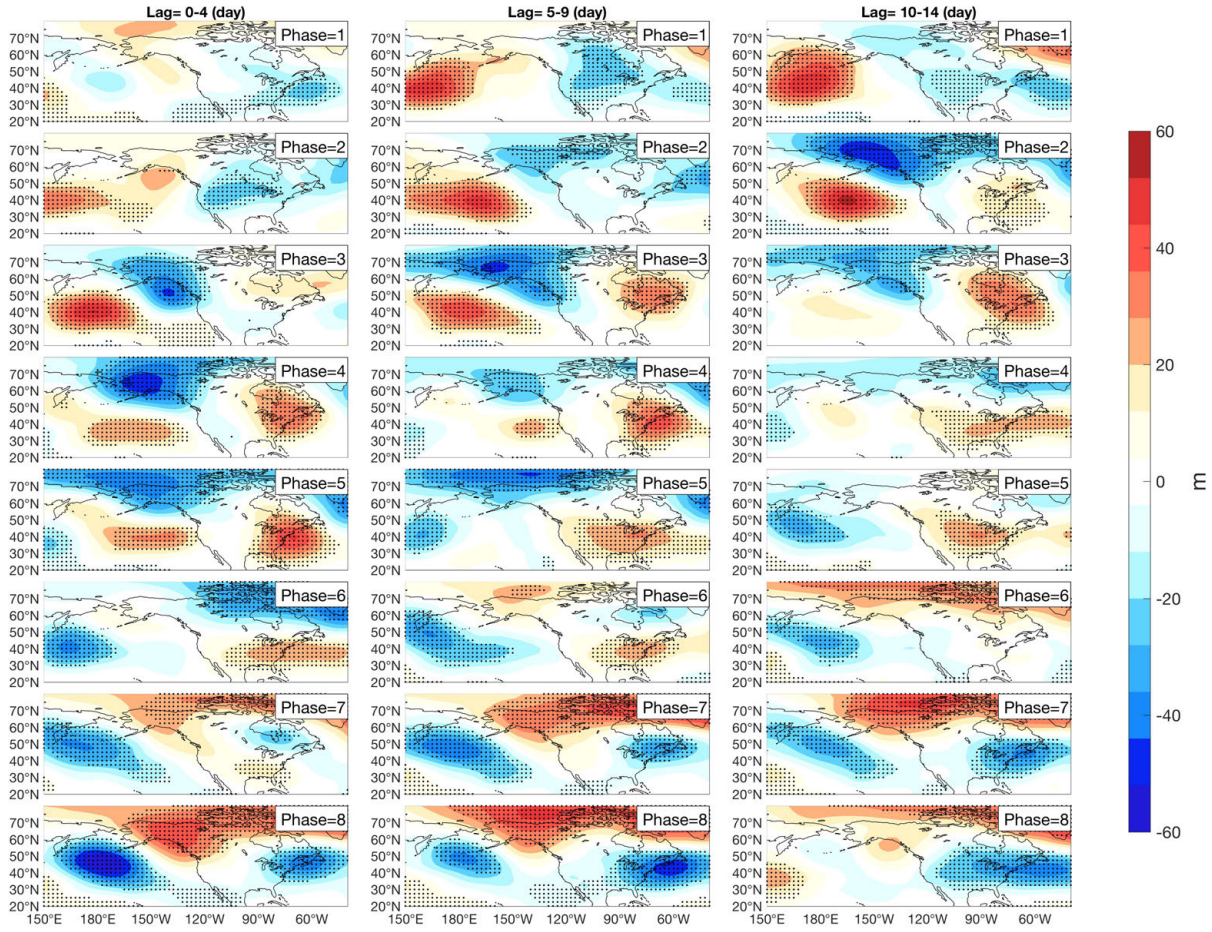

Fig. 2.1. MJO phase composite of anomalous 500-hPa geopotential height for lag 0-4 days after an MJO event, lag 5-9 days and lag 10-14 days. The dotted regions denote the anomalies that are significantly different from zero at 95% confidence based on bootstrapping analysis.

prediction, because it implies that particular MJO phases may be more robust, and thus, support extended range predictability. To test whether the occurrence frequency of positive and negative geopotential height anomalies in the North Pacific change with MJO phase, we estimate the corresponding frequencies at each grid point over different phases and lags using daily data. Figure 2.2 shows gridpoints where positive or negative anomalies occur over at least 65 % of all events. In Figure 2.2, the dotted regions present a wave-train pattern extending from the North Pacific to the Gulf of Alaska which is consistent with Figure 2.1 (e.g. phase 2, lag 10-14 and phase 3, lag 5-9). Some regions in the wave-train pattern exceed 75% frequency (hollow dots) such as the centers of high pressure anomaly in the North Pacific and low pressure anomaly in the Gulf of Alaska at phase 2, lag 10-14. On the other hand, the regions with low occurrence frequency (without dots) are also the regions with insignificant composited anomalies in Figure 2.1. In addition, at

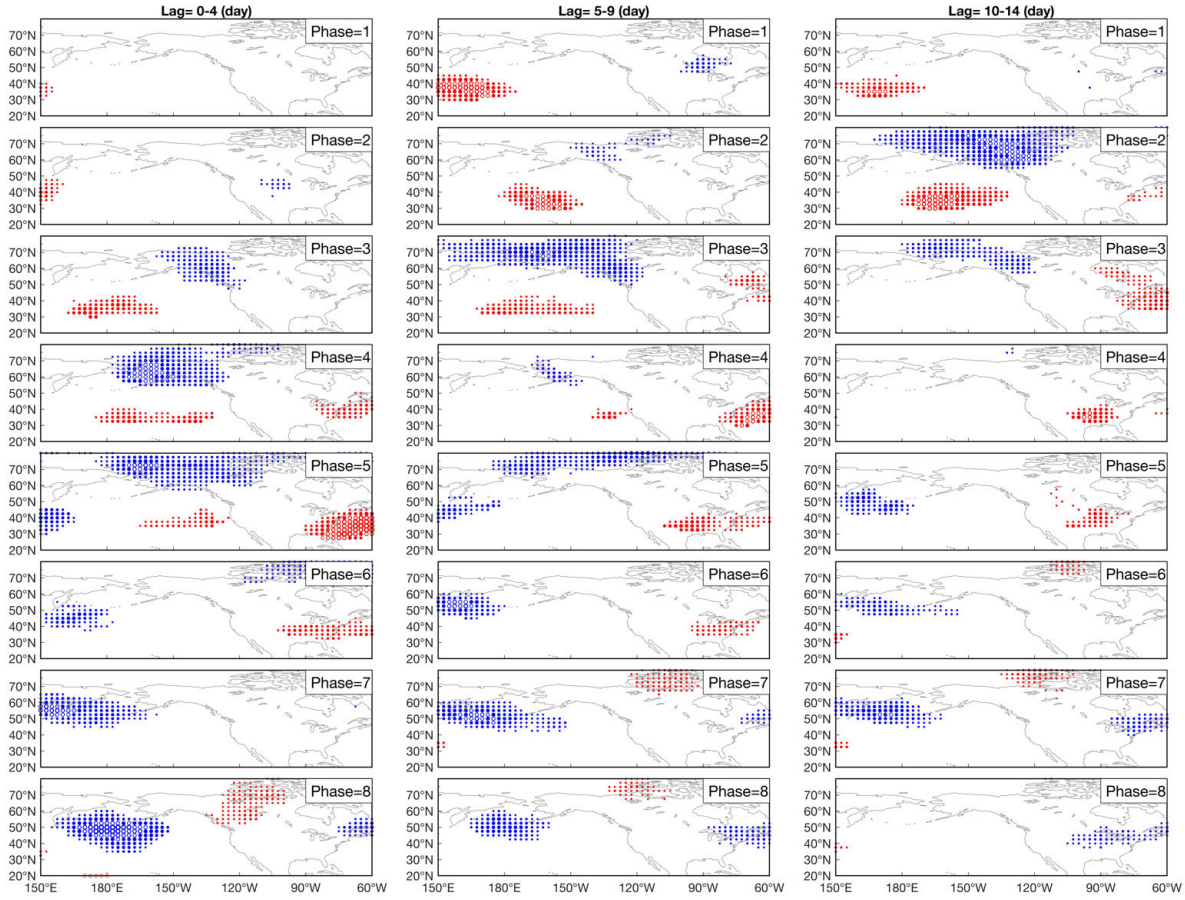

Fig. 2.2. The sign agreement of anomalous Z500 over different MJO events and lags. Red (blue) dots indicate positive (negative) geopotential height anomalies with occurance frequency > 65%. Open circles indicate an occurrence frequency > 75%

.

lag 10-14, which is the traditional limit of weather predictions, some phases (e.g. phase 2 and phase 7) demonstrate high preference of a Rossby wave train pattern while others do not (e.g. phase 4 and phase 8). These results suggest that extended predictions may be possible for certain MJO phases.

Nevertheless, the result in Figure 2.2 is not enough to show the pattern consistency over different MJO events, since the sign consistency is calculated on a local basis with no knowledge of the large-scale pattern. To quantify the robustness of the teleconnected patterns, we calculate paired pattern correlations in the North Pacific (150^oE-120^oW, 20^oN-70^oN) over different phases and time lags. For each phase and lag, one pattern correlation coefficient is derived from every two events. Thus, if there are m events, the number of combinations will be $C_2^m = \frac{m\cdot(m-1)}{2}$. By calculating the number of paired combinations that exceed a correlation of 0.5, we quantify the consistency of the Z500 patten across MJO phases. Figure 2.3 shows the

result of the paired correlation analysis. Dark (light) colors indicate more (fewer) pairs with high pattern correlations and dotted regions denote where the number of high correlations exceed the 99% confidence bounds by bootstrapping analysis. The shaded regions show stair-like patterns with a slope of 5 days per phase, which is the typical phase duration of the MJO. Using phase 2 as an example, the transition from light colors (lag 1-7) to dark colors (lag 8-15) indicates an increasing influence of robust tropical-extratropical teleconnections in modulating the midlatitude Z500 pattern as well as the increased pattern consistency 8-15 days following MJO phase 2. A remarkable fact of Figure 2.3 is that it provides more information than previous studies which showed that the Pacific North American (PNA) pattern is more likely to occur after MJO phase 2 and phase 6 by composite analysis. First, the daily Z500 is a highly varying field. Thus, even though composite maps may show a PNA-like pattern, it is unclear how much any one event will actually look like the PNA pattern. However, Figure 2.3 shows phase-dependent pattern consistency without supposing a PNA or any other pattern. Second, the phase-dependent pattern consistency gives us a new perspective on the extended range prediction since it indicates that the Z500 pattern over specific phases (e.g. phase 2 and phase 6) might be more predicable than others (e.g. phase 4 and phase 8).

2.3.2 Ensemble Agreement of Z500 in ECMWF ensemble hindcast

Our analysis of the MERRA reanalysis demonstrates that tropical-extratropical teleconnection patterns driven by the MJO are more robust for specific MJO phases and time lags compared to others. With this observational result in mind, we next address whether the prediction skill of Z500 in the North Pacific in a numerical weather prediction model is improved for MJO phases with more robust teleconnections. Therefore, we examine how the MJO's tropical-extratropical teleconnections influence Z500 prediction skill as a function of MJO phase in the ECMWF model ensemble hindcasts. We note that the prediction skill is not only a function of the teleconnection robustness, but also a function of error growth due to inaccuracies in the initial conditions, model physics and truncation errors.

In order to quantify the robustness of the model's composite MJO teleconnections, we divide the ECMWF ensemble hindcasts (1999-2015) into ten groups, arbitrarily selected on the basis of ensemble member number. Then, we compute the average composite pattern and agreement in sign across the ten groups (Figure 2.4). Here, an n-day lead represents not only n days after a given MJO phase but also n days after the simulation was initialized. Red- (blue-) dotted regions indicate where all of the ensemble members agree on the sign (i.e. positive or negative) of the composited Z500 anomalies. We note that most of the regions with high ensemble agreement also agree with the sign of anomalous Z500 in the reanalysis (not

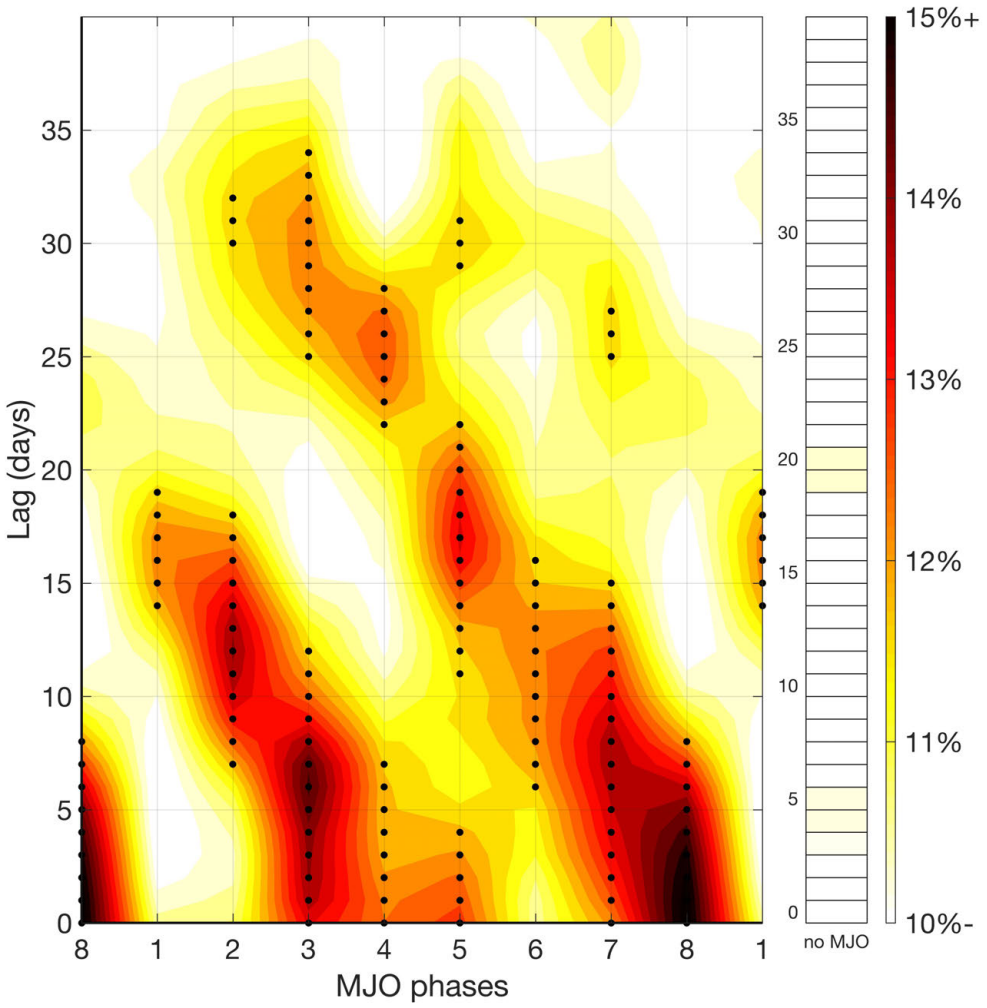

Fig. 2.3. The pattern agreement of Z500 over different MJO events quantified using pattern correlations. Shading indicates the occurance frequency of any two events exhibiting a correlation coefficient > 0.5. Dotted regions indicate an occurance frequency that is significantly higher than climatology at the 99% significance level based on a bootstrapping analysis.

shown). The dot size shows the amplitude of the ensemble-mean Z500. In Figure 2.4, the dots are generally evenly distributed in the domain immediately after the initialization time (lead 0-4) for both MJO phase 2 and phase 4, which indicates that all ten ensemble members agree on the composite pattern. As the lead time increases, Phase 2 continues to show widespread areas of high agreement including the high-pressure anomaly in the North Pacific. In particular, these regions show a wave train pattern that is very similar to the composited Z500 pattern in Figure 2.1 (phase 2 and lag 10-14). This high agreement on the wave train pattern even exists at lead times 15-19 of phase 2. In contrast to phase 2, the dots for phase 4 become more

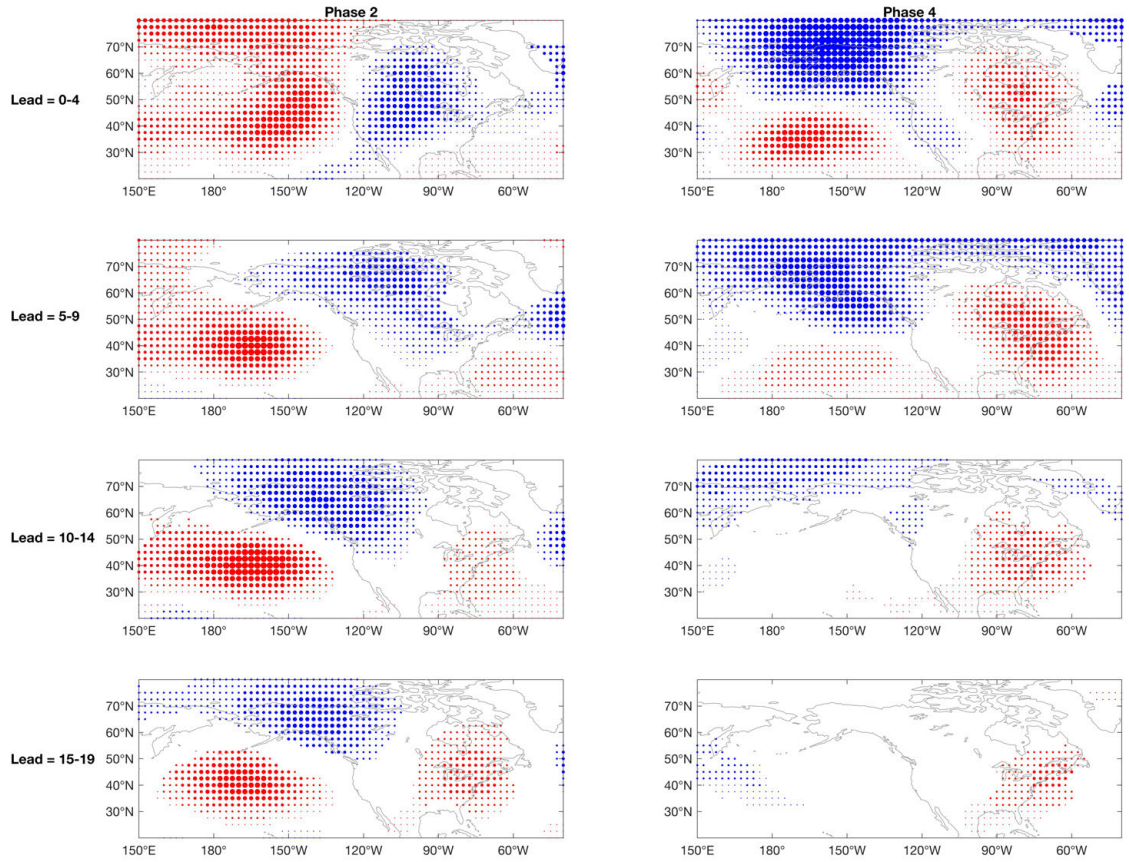

Fig. 2.4. Composites of Z500 over ECMWF's 10 ensemble members for MJO phase 2 and phase 4. Dotted regions indicate all (10) ensemble members and the MERRA reanalysis agree on the sign of the anomaly and the dot size is defined by the ensemble-averaged amplitude of composite Z500. Small: amplitude < 40m, Median: 40-70m and Large: >70m. Blue shading denotes negative anomalies while red shading denotes positive anomalies

sparse with increasing lead time and there are few grid points with large Z500 amplitude. This tendency becomes clearer for lead times 10-14 and 15-19 when little ensemble agreement exists for phase 4. Hence, Figure 2.4 provides evidence that the current ECMWF forecast system has strong ensemble member agreement for the composited teleconnected geopotential height anomalies at leads of greater than two weeks for certain phases of the MJO.

Figure 2.4 is based on the composite pattern of Z500, which only provides a general picture of how MJO-related teleconnections may influence the prediction skill of the mean pattern. However, Z500 variations on a daily basis may not necessarily be modulated as consistently as in the composite sense. Therefore, we

re-examine the concepts in Figure 2.3 and Figure 2.4 for individual MJO events instead of the composite fields. First, we calculate pattern correlation coefficients between the daily ensemble mean and the daily observed Z500 from MERRA for every event. We then calculate and plot the percent of the correlations that are greater than zero as a function of model lead time and MJO phase. The result is shown in Figure 2.5, where dark colors indicate higher frequencies of positive correlations between the model forecast and what was observed, and dots indicate regions that are 99% significantly higher than the randomly sampled data by bootstrapping. To assess significance, we apply bootstrapping analysis under the null hypothesis that the chance of predicting positive correlation coefficients is the same over different events at the same model lead time. Days including the events with and without strong MJOs are randomly sampled according to the numbers of MJO events at different phases and lead times. By resampling data 500 times, we can approximate the distribution of correlations under the null hypothesis.

Two distinct features are evident in Figure 2.5. First, the color of shading goes from dark red to light yellow, which is associated with the decrease of prediction skill with time. This is also seen in Figure 2.4, which shows fewer dots with increasing model lead time. In addition to the decrease of prediction skill, the second prominent feature is that extended skill is found in selected MJO phases, e.g., phase 1 and 2 show longer lead time with higher prediction skill than phase 4 and phase 8. Several possible explanations exist for this phase-dependent prediction skill. One explanation is associated with model error growth. Robust teleconnections might not only modulate the Z500 patterns over different events but also reduce the ensemble spread. With such robust teleconnections, the ratio of the teleconnection signal to the noise introduced by the initial perturbations stays large enough to produce skillful forecasts up to 3 weeks later. This point is also supported by Figure 2.4: all ensemble members hindcast a robust wave train pattern at phase 2 and lead times 15-19. For phases without robust teleconnections, such as phase 4 (Figure 2.3), the ensemble spread grows much faster than the phases with robust teleconnections. However, one might wonder why phase 4 has high pattern consistency at lead times 22-30 (Figure 2.3) but relatively low prediction skill (Figure 2.5). One possible reason for this behavior is that the phase 4 teleconnection only becomes robust at 22-30 days after an event (Figure 2.3). Thus, the model error might be too large at 22-30 days after the initialization to take advantage of the information from a robust teleconnection. The second explanation is related to the traditional "Maritime Continent prediction barrier". Previous studies have shown that most numerical models have difficulty in simulating MJO propagation across the Maritime Continent due to coarse model resolution and poorly-simulated scale interactions (*Peatman et al.* 2015; *Kim et al.* 2016), which might cause unrealistic large-scale circulation anomalies in the upper troposphere and negatively impact the Rossby wave

source that produces tropical-extratropical teleconnections. A third possible explanation is associated with the sensitivity of the teleconnection produced by anomalous tropical heating to the mean state. Research has shown that the relative position of anomalous heating and the subtropical jet is a key factor in determining the nature of tropical- extratropical teleconnections (*Henderson et al.* 2017). In general, all of these factors can limit the prediction skill of numerical models: the former implies that a large signal (teleconnection) to noise (error growth) ratio is required to have skillful extended predictions; the latter two factors imply that if the model cannot simulate the MJO or mean state with fidelity, it will not produce reasonable teleconnection signals that provide skillful extended predictions.

2.4 DISCUSSION AND CONCLUSIONS FOR CHAPTER 1

The results shown here indicate that MJO convection can produce a robust modulation of Z500 in the North Pacific for certain phases and time lags. This phase-dependent modulation of Z500 by the MJO is also reflected in an MJO phase and forecast lead dependence in ECMWF forecast model's ensemble agreement and prediction skill. A robust tropical-extratropical teleconnection at MJO phase 1, 2, 5 and 6 provides more confidence in the prediction of Z500 at 2 to 3 week leads, which is longer than that associated with the traditional 10-13 day midlatitude "predictability barrier". However, the prediction skill is not increased at all phases and lead times at which reanalysis fields indicated high pattern consistency (e.g. phases 4). The factors responsible for diminished prediction skill at MJO phase 4 relative to that suggested by reanalysis fields remain to be determined. Nevertheless, our results show that MJO-related tropical-extratropical teleconnections clearly have profound implications for understanding and predicting S2S time scale variability over the North Pacific and North America.

The insight we have gained about the phase-dependent MJO modulation of Z500 has important implications, and also suggests some interesting questions for future work. For the high frequency weather phenomena influenced by the midlatitude geopotential height variations, such as atmospheric rivers (*Mundhenk et al.* 2016) and blocking anticyclones (*Henderson et al.* 2016), we may expect some similarities between their prediction skill and that of Z500. This is an area of ongoing research. Low-frequency variability (longer than intraseasonal time scales) associated with phenomena such as the quasi-biennial oscillation (QBO) or El Niño and Southern Oscillation (ENSO) are also likely to modulate the nature of MJO teleconnections (*Baggett et al.* 2017; *Moon et al.* 2011; *Son et al.* 2017). Furthermore, the interaction between MJO heating and the position of east Asia jet presents a challenge for midlatitude teleconnection predictions, given changes in jet position and strength from year to year. Although subject to the uncertainties of scale

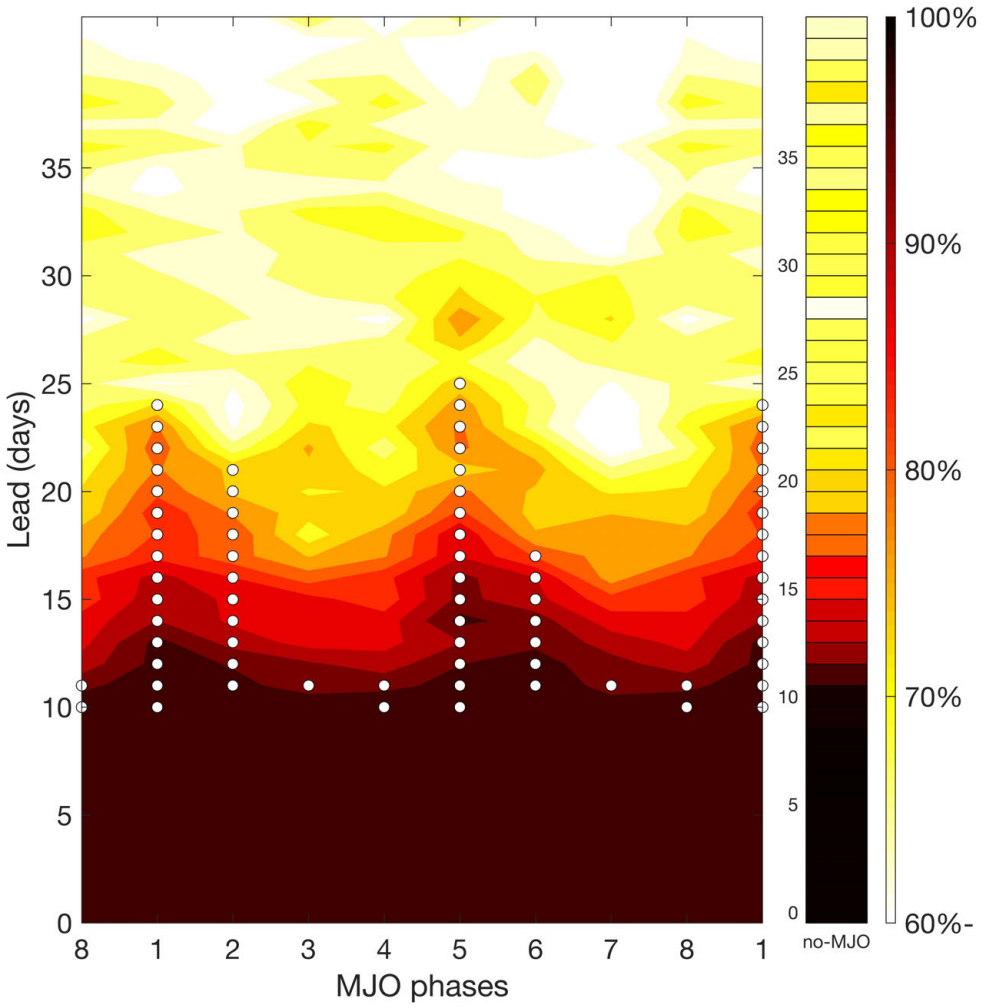

Fig. 2.5. The frequency (as a percentage) with which the Z500 pattern predicted by the ECMWF ensemble mean is positively correlated with the observed Z500 anomalies from MERRA reanalysis. The dotted regions indicates the value is significantly higher at 99% confidence than the randomly sampled data at the same lead time by bootstrapping analysis. The sample sizes for each MJO phase are (in order from 1 to 8) 89, 110, 112, 115, 86, 98, 108 and 110.

interactions and nonlinear error growth in numerical models, the robust impacts of the MJO on midlatitude geopotential height, and thus the midlatitude circulation and steering flow, provides the scientific community useful tools for subseasonal-to-seasonal prediction.

CHAPTER 3

The consistency of MJO teleconnection patterns: an explanation using linear Rossby wave theory [2]

In this chapter, we examine the physical mechanisms that lead some MJO phases to have more consistent teleconnections than others using a Linear Baroclinic Model. The results show that MJO phases 2, 3, 6 and 7 consistently generate Pacific/North American-like patterns on S2S timescales while other phases do not. A Rossby wave source analysis is applied and shows that a dipole-like pattern of Rossby wave source on each side of the subtropical jet can increase the pattern consistency of teleconnections due to the constructive interference of similar teleconnection signals. On the other hand, symmetric patterns of Rossby wave source can dramatically reduce the pattern consistency due to destructive interference. A dipole-like Rossby wave source pattern is present most frequently when tropical heating is found in the Indian Ocean or the Pacific warm pool, and a symmetric Rossby wave source is present most frequently when tropical heating is located over the Maritime Continent. Thus, the MJO phase-dependent pattern consistency of teleconnections is a special case of this mechanism.

3.1 INTRODUCTION

Since the 1980s, the mechanisms of tropical heating-induced extratropical responses have been extensively studied based on the knowledge of barotropic and baroclinic vorticity equations in spherical coordinates (*Hoskins and Karoly* 1981). Observational and numerical studies have also shown coherent variations between extratropical geopotential height anomalies and tropical heating (e.g. El Nino and Southern Oscillations, *Bjerknes* 1969; *Simmons et al.* 1983). A number of studies proposed mechanisms to explain the growth of the teleconnected signals such as the barotropic conversion by the heating-induced divergent wind in the upper troposphere (*Simmons et al.* 1983) or dynamical feedbacks between synoptic eddies and low frequency modes of variability (*Held et al.* 1988; *Jin et al.* 2006). While most of the research mentioned above focused on stationary forcings (e.g. ENSO or topography) and the steady state response, since the 1990s, scientists have been also investigating coherent variations between MJO convection and extratropical

[2] This chapter contains material that has been published in the *Journal of Climate* as: Tseng, K., E. Maloney, and E. Barnes, 2019: The Consistency of MJO Teleconnection Patterns: An Explanation Using Linear Rossby Wave Theory. *J. Climate*, **32**, 531–548

responses. By using objective analysis (e.g. lag regression between an MJO index and time-filtered extratropical stream function anomalies; *Black* 1997; *Matthews et al.* 2004) and idealized simulations based on the linearized barotropic vorticity equation forced by a propagating heating source (*Ferranti et al.* 1989), the most unstable modes (e.g. Pacific/North American pattern [PNA] and North Atlantic Oscillation [NAO]) excited by the MJO in the extratropical regions were discovered. *Mori and Watanabe* (2008) conducted a detailed vorticity budget analysis showing that linear dynamics governed by the interaction between the mean state and intraseasonal variability dominates the growth and triggering mechanisms of the PNA. This process was further verified in an idealized simulation with linearized primitive equations (*Seo and Lee* 2017).

Recently, by using reanalysis data and ECMWF ensemble hindcasts, *Tseng et al.* (2018) (chapter 2) found that MJO heating in specific phases (e.g. phase 2, phase 3, phase 6 and phase 7) generate consistent teleconnection patterns in the extratropical Pacific and North America from one event to the next. The pattern consistency was defined by examining the fraction of events with high pattern correlations of the 500 hPa geopotential height anomaly field. Their study further showed that the phases with consistent teleconnection patterns have improved numerical weather forecasts at 2-4 week lead times while the other phases are constrained by the traditional limit of midlatitude prediction skill (about 10 days, *Hamill and Kiladis* 2014). This result from chapter 2 implies that if one can reveal the fundamental mechanisms that cause the phase-dependent pattern consistency of tropical-extratropical teleconnections, one might be able to determine why prediction skill improves in specific MJO phases.

Here, the mechanism responsible for the MJO phase-dependent pattern consistency of tropical-extratropical teleconnections is investigated by using a linear baroclinic model (LBM) and reanalysis data. This paper is organized as follows. In section 3.2, detailed descriptions of the LBM, data and methods are provided. In section 3.3, the phase-dependent pattern consistency documented in chapter 2 is interpreted through the LBM. It will be shown that the teleconnections during some MJO phases are less sensitive to variations in the basic state and variations in the MJO's heating pattern from event to event than others. In section 3.4, a mechanism is proposed to explain why the pattern consistency of MJO-induced teleconnections is a phase-dependent phenomenon. In section 3.5, the concept of teleconnection pattern consistency in response to tropical heating is generalized beyond the MJO using reanalysis data. Section 3.6 holds the conclusion and remarks.

3.2 DATA, MODEL AND METHOD

3.2.1 Linear Baroclinic Model

3.2.1.1 Model description

In this study, a linear-baroclinic model (LBM, *Watanabe and Kimoto* 2000) is used to examine the mechanisms of tropical-extratropical teleconnections. There are two main reasons for using a LBM. First, in a linearized model, it is easier to separate the anomalous response from basic state, which cannot be done in the real world or a model with feedback processes. Second, previous studies have shown that the MJO-induced teleconnection is dominated by linear dynamics (*Mori and Watanabe* 2008). In this study, we go one step further to see whether the phase-dependent teleconnection pattern consistency documented in chapter 2 also exists in a linear model. If the phase-dependent pattern consistency can be simulated by the LBM, we can narrow down the possible mechanisms using dry and linear dynamical considerations.

In the LBM, the primitive equations are linearized about prescribed basic states. The vertical and horizontal resolutions of the model are 20 sigma levels and T42, respectively. For the numerical damping, we employed 4^{th} order biharmonic damping (∇^4) with an e-folding time of 2 hours for the shortest wavenumber. We also employed Rayleigh friction and Newtonian cooling in the model with an e-folding time of 20 days in most model layers while the top 2 layers and the bottom 3 layers have an e-folding times of 0.5 days. All of these settings are fixed over the different simulations to ensure that differences in the model output result from only the different forcing and basic states.

3.2.1.2 Model Basic state and MJO Forcing

When we use the LBM as the platform for mechanism testing, two inputs are required: a basic state and anomalous heating. In the LBM, the linear operator is associated with the given basic state pattern and the anomalous heating is used to drive the anomalous circulation in the model. For the model basic states, the European Centre for Medium-Range Weather Forecasts (ECMWF) third-generation reanalysis product (ERA-Interim hereafter, *Dee at al.* 2011) from 1979 to 2015 is used. ERA-Interim is provided on 20 vertical pressure levels from 1000 hPa to 100 hPa and the horizontal resolution is interpolated to T42 resolution (approximately 2.8 degree grid spacing). Since the extratropical teleconnections are stronger in boreal winter than in boreal summer, the necessary variables for the basic states are derived from extended boreal winter averages (November to March) during 1979 to 2015.

The daily mean apparent heat source (Q_1) is computed following *Yanai et al.* (1973) for use in representing intraseasonal forcing (equation 3.1). In equation 3.1, v is the horizontal wind, ω is the pressure velocity

and s is the dry static energy defined as $s = c_p T + gz$, where c_p is the specific heat, T is the temperature, g is the gravitational acceleration, and z is the height.

$$Q_1 \equiv \frac{\partial s}{\partial t} + v \cdot \nabla s + \omega \frac{\partial s}{\partial p} \tag{3.1}$$

Following *Yanai et al.* (1973), the heat budget residual, Q_1, represents sub-grid scale physical processes including radiative cooling, condensation heating, evaporation, and eddy heat flux convergence. In particular, in regions with active deep convection, Q_1 is dominated by deep convective heating. In this study, the anomalous Q_1 is derived by removing the linear trend and the first three harmonics of the seasonal cycle. Further, a Lanczos band-pass filter (20-100 days) with 9 weights is applied to obtain the intraseasonal time scale diabatic heating anomaly (Q_1'). In addition, to ensure that all signals originate from the tropics rather than being excited by local heating anomalies in extratropical regions, we only specify model forcing between 30^oS and 30^oN.

3.2.1.3 Experimental Design

To test the teleconnected response to the variations of basic states and MJO forcing, we conduct two sets of experiments in this study: (1) Fixed MJO heating (FixQ1 hereafter) and (2) Fixed basic state (FixBS hereafter). The main philosophy of these two experiments is to perform ensembles of simulations with small perturbations added either to the basic state or MJO heating to test the phase-dependent consistency of tropical-extratropical teleconnections when given these modest perturbations. In the FixQ1 experiment, we use the MJO-phase composited Q_1' as the forcing. For the MJO event selection in this study, unless specified otherwise, an MJO event is retained if the OLR-based MJO index (OMI hereafter, see the subsection of observational reference for detailed descriptions; *Kiladis et al.* 2014) indicates the same phase for at least 5 consecutive days and the amplitude of the index meets or exceeds 1 standard deviation for all 5 days. FixQ1 gets its name because the MJO Q_1' is fixed for each of the eight MJO phases while the basic state of the circulation and the static stability are varied. Specifically, we replace the model basic states with 36 different realizations. Each realization is derived from a different years' boreal winter averaged including three dimensional winds, temperature, specific humidity and surface pressure (from 1979 to 2015). Thus, for each MJO phase, we have 36 different simulations resulting in a total of $8 \times 36 = 288$ simulations. While it might not be obvious that basic state variations from one winter to the next are small in the context of interannual variability such as El Nino-Southern Oscillation, our results below will demonstrate that this assumption is indeed valid and that certain MJO phases demonstrate teleconnection pattern consistency even in the presence of interannual basic state variability. Further, to ensure that the extratropical response

is generated by the forcing within the typical duration of an MJO phase of 5 days (*Henderson et al.* 2017, lag 0-4), we gradually turn off the Q_1' forcing by applying an e-folding factor of 5 days to the given forcing . It is worth mentioning that MJO heating is given to the LBM for each phase separately, which indicates that no MJO phase precedes the next MJO phase, although the MJO forcing for the particular phase still evolves throughout that phase. This may result in some differences between the LBM simulations and reanalysis data, and these differences will be discussed in the next section. However, this is not believed to be a bad assumption since MJO events across all phases on average maintain amplitude greater than 1 sigma for less than 10 days (*Henderson et al.* 2017).

For the FixBS experiment, we fix the basic state to the 1979-2015 boreal winter average and give the model MJO forcing from first 24 MJO events for each phase, which satisfies the criteria given above, resulting in a total of $8 \times 24 = 196$ simulations. An MJO event is defined based on the amplitude and duration criteria given above. We also apply the same e-folding factor to the heating in FixedBS experiment to make the experiment setup consistent.

3.2.2 Observational Reference

3.2.2.1 500hPa geopotential height anomalies

Typically, tropical-extratropical teleconnections have a barotropic structure away from the tropics; thus, we use the 500 hPa geopotential height as the major diagnostic variable noting that other tropospheric layers give us similar results. In this study, to enable a comparison with chapter 2, which used Modern-Era Retrospective Analysis for Research and Applications (MERRA) for analysis, we employ ERA-Interim from 1979 to 2015 as the observational reference. The data is interpolated to a horizontal resolution of $2.5^o \times 2.5^o$. To remove the annual cycle, the 500hPa geopotential height data is pre-processed with a similar approach to that applied to $Q1$. The only pre-processing difference between Z500 and $Q1$ is that we do not apply the intraseasonal band-passed filter to Z500, which enables a direct comparison with chapter 2.

3.2.2.2 MJO indices

To create a proxy for MJO convection evolution, the OLR-based MJO index is used (OMI hereafter, *Kiladis et al.* 2014), which was acquired from `https://www.esrl.noaa.gov/psd/mjo/mjoindex/`. One advantage of using the OMI to define intraseasonal convective heating is that the OMI is purely based

on outgoing longwave radiation, which is a good proxy for tropical deep convection. Planetary-scale convection (zonal wave numbers 1-3) in the tropics has been proven to play a vital role in generating tropical-extratropical teleconnections in previous studies (*Hoskins and Karoly* 1981; *Hsu* 1996). Thus, OMI is a more ideal MJO index for the purposes of this study than other indices defined by multiple variables.

3.2.3 Method

3.2.3.1 Quantifying the pattern consistency

The approach of paired pattern correlations is used to quantify the pattern consistency of the teleconnections over different MJO events, a method which was documented in chapter 2. For each phase and lag, one area-weighted anomalous pattern correlation coefficient of Z500 is derived from every two MJO events in the North Pacific (150^oE-120^oW,20^oN-70^oN). By calculating the fraction of pairs that meet or exceed a correlation coefficient of 0.5, we can estimate the pattern consistency for specific MJO phases and lags. The pattern correlation of anomalous fields has been widely used in operational centers as a metric to quantify prediction skill and chapter 2 demonstrated that the MJO phases with consistent patterns of geopotential height anomalies are also characterized by improved model prediction skill. The mechanism that causes this MJO-phase dependent pattern consistency is a major focus of this study.

In chapter 2, the pattern consistency was assessed in MERRA (their Figure 3). To examine whether this analysis approach also works in ERA-Interim, we applied it to Z500 of ERA-Interim from the same 1979 to 2015 period (Figure 3.1). The dark colors indicate higher pattern consistency of tropical-extratropical teleconnections over different MJO events while the bright colors represent lower pattern consistency. The dotted regions denote that the pattern consistency exceeds the 99% confidence bounds by a bootstrapping analysis. (For the bootstrapping analysis, we randomly resampled the data 500 times based on the sample size of each MJO phase and time lag to approximate the distribution of the fraction of pairs with high pattern correlations due to chance alone.) Looking at Figure 3.1, we see two stair-like patterns of high pattern consistency that are nearly quantitatively identical to the result of chapter 2 where the MERRA reanalysis was used. This indicates that the approach used in chapter 2 is also reproducible using other reanalysis data. In the following section, we apply the same analysis approach to the LBM simulations and test whether the LBM can reproduce these results.

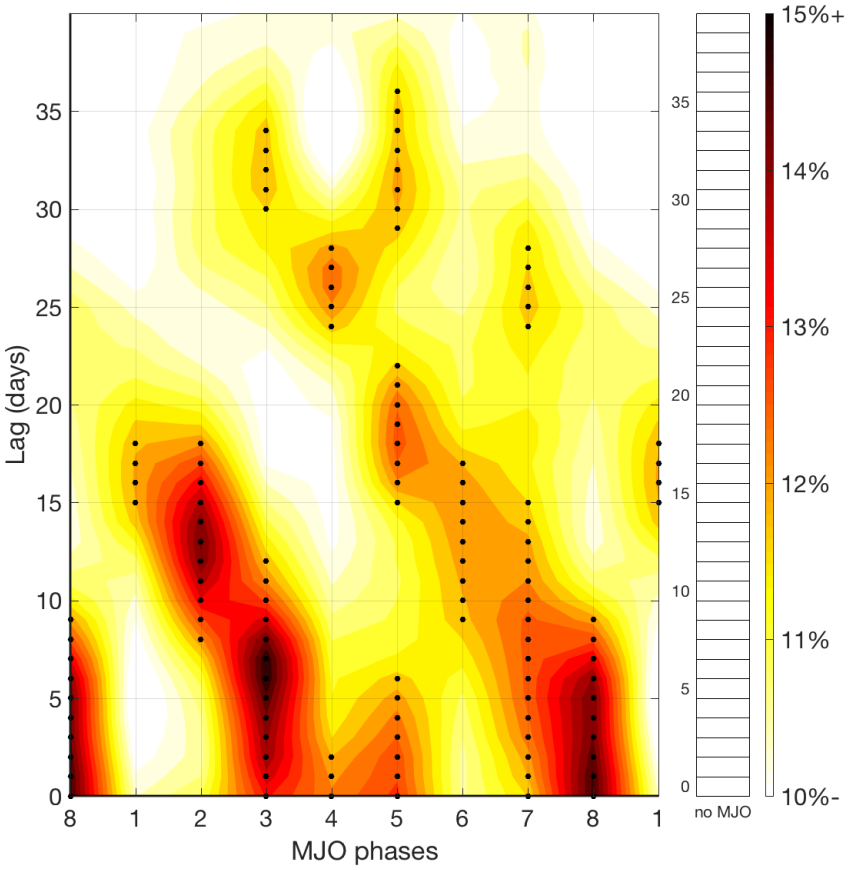

Fig. 3.1. The pattern agreement of Z500 (150^{o}E-120^{o}W,20^{o}N-70^{o}N) over different MJO events as quantified by pattern correlations. Shading indicates the occurrence frequency of any two events with correlation coefficient > 0.5. Dotted regions indicate the value is greater than the 99% confidence bounds based on a bootstrapping analysis. Recreation of Figure 3 in chapter 2 but now using ERA-Interim.

3.2.3.2 Linearized Rossby Wave Source

To investigate the Rossby wave source that triggers teleconnected patterns in the extratropical regions, we use the linearized barotropic vorticity equation (*Sardeshmukh and Hoskins* 1988; *Seo and Lee* 2017), applied to both the LBM simulations and ERA-Interim:

$$\frac{\partial \zeta'}{\partial t} = S' - \bar{V}_\psi \cdot \nabla \zeta' - V'_\psi \cdot \nabla \bar{\zeta} + F' \tag{3.2}$$

In equation 3.2, the terms with primes indicate intraseasonal time scale anomalies and overbars denote the basic state. ζ is the absolute vorticity, V_ψ is the rotational wind, S is the Rossby wave source and F is the frictional term. The linearized Rossby wave source is contributed by four different terms:

$$S' = -\bar{\zeta}\nabla \cdot V'_\chi - V'_\chi \cdot \nabla\bar{\zeta} - \zeta'\nabla \cdot \bar{V}_\chi - \bar{V}_\chi \cdot \nabla\zeta' \tag{3.3}$$

In general, the vorticity tendency in equation 3.2 is dominated by the rotational flow induced advection (the second and third terms on the right side). However, in regions of active deep convection, the Rossby wave source term can be large and influence wave generation. In equation 3.3, the first two terms on the right side indicate the stretching of climatological absolute vorticity by the divergence of the anomalous flow ($-\bar{\zeta}\nabla\cdot V'_\chi$) and the advection of climatological absolute vorticity by the anomalous divergent flow ($-V'_\chi\cdot\nabla\bar{\zeta}$). The last two terms are the stretching of anomalous vorticity by the climatological divergence ($-\zeta'\nabla\cdot\bar{V}_\chi$) and the advection of anomalous vorticity by the climatological divergent flow ($-\bar{V}_\chi\cdot\nabla\zeta'$). In *Mori and Watanabe* (2008) and *Seo and Lee* (2017), the authors noted that the first two terms on the right side of equation 3.3 are the dominant terms on intraseasonal timescales. By calculating the Rossby wave source (S' in equation 3.3), we can relate the Rossby wave source pattern in the subtropical and extratropical regions to the teleconnection pattern consistency that varies as a function of MJO phase and lag.

3.3 TELECONNECTIONS IN LBM

In this section, we address the following questions. (1) Can the LBM simulate the phase-dependent pattern consistency that is found in reanalysis data ? (2) How does the pattern consistency of MJO-induced teleconnections respond to modest variations in the basic state and MJO heating?

3.3.1 Model Forcing and Basic States

Figure 3.2 shows the MJO phase composite of column-integrated Q'_1 (shading) used in the FixQ1 experiment. The composited patterns show that MJO-related convection initiates in the central Indian Ocean in Phases 1 and 2, strengthens in the eastern Indian Ocean, and the dissipates around the date line in Phases 7 and 8. The average duration of each phase is $\simeq 5$ days, which is consistent with previous studies (*Henderson et al.* 2017) and provides motivation for our experimental design. For the FixQ1 experiment, we use the composite Q'_1 indicated by the shading in Figure 3.2. The contours in Figure 3.2 show the standard deviation of the column-integrated Q'_1 over different MJO events used in the FixBS experiment. In general,

the contours are collocated with regions of maximum Q_1', although some regions and phases exhibit less good agreement. For example, the further eastward extent of contours compared to the shading in the central Pacific likely results from interannual variability of MJO heating associated with ENSO (*Hendon et al.* 1999).

Basic state winds and their variability are shown in Figure 3.3. The shading represents the boreal winter zonal wind at 200 hPa averaged from 1979-2015, and the contours are the standard deviation of the zonal wind over the 36 boreal winter means for different years used in the FixQ1 experiment. Generally, two dominant features are apparent: the North Pacific jet stream and the North Atlantic jet stream, which are found to the east of Asia and North America, respectively, between 30^oN and 40^oN. The contours in Figure 3.3 show the interannual variability of the jet streams, including the eastward extension and northward or southward shift of the jets. The jet shifts likely result from interannual variability associated with ENSO. Typically, the subtropical jet extends eastward and equatorward during El Nino years, while westward and poleward in La Nina years. The combination of information from the shading in Figure 3.2 and the contours in Figure 3.3 can be used to test how MJO-induced teleconnections evolve with modest variations of the jet stream and other aspects of the basic state, i.e. our FixQ1 experiment. Similarly, if we exploit information from the contours in Figure 3.2 (i.e. the MJO heating variability over different events) and the shading in Figure 3.3 (i.e. the climatological basic state), we can test the sensitivity of the teleconnected responses to modest variations of tropical heating, which comprises the FixBS experiment. In reality, both the basic state and MJO heating change together (e.g. during ENSO warm events), however, this kind of linearized experimental design can help us simplify the questions and access the key mechanisms in a more tractable manner.

3.3.2 Z500 Composites

The shading in Figure 3.4 and Figure 3.5 represents the MJO phase- and lag- composited Z500 in FixQ1 and FixBS, respectively. The contours in Figure 3.4 and Figure 3.5 show the same field from ERA-Interim. In Figure 3.4, both observations and the LBM simulations indicate positive Z500 in the North Pacific during MJO phases 2 and 3, while the opposite patterns can be found in phases 6 and 7 associated with opposite signed MJO heating in the tropics. This PNA-like pattern has been widely documented in observational studies and numerical simulations (*Mori and Watanabe* 2008; *Seo and Lee* 2017). Although the observed teleconnection pattern is generally collocated with the simulated pattern, some inconsistency still exists. For example, the amplitude of the simulated teleconnections is systematically smaller than the

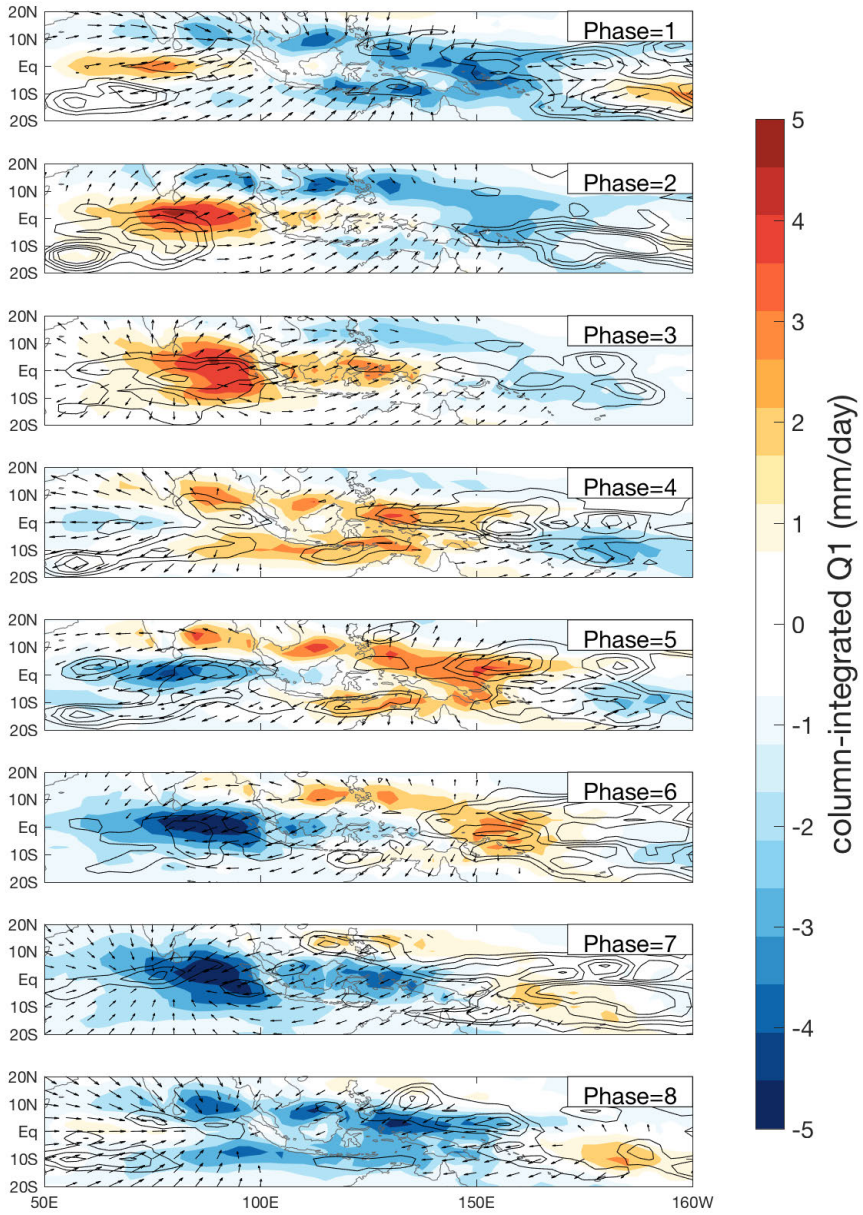

Fig. 3.2. The MJO phase composited column-integrated Q_1 used in the FixQ1 experiment (shading, $mm \cdot d^{-1}$) and the standard deviation of the intraseasonal time scale column-integrated Q_1 over the different events used in FixBS (contours, from 3 $mm \cdot d^{-1}$ to 5 $mm \cdot d^{-1}$ with interval of 0.5 $mm \cdot d^{-1}$) The vector shows the MJO-phase composited 200 hPa divergent wind; vectors with amplitude smaller than 0.8 (ms^{-1}) are omitted.

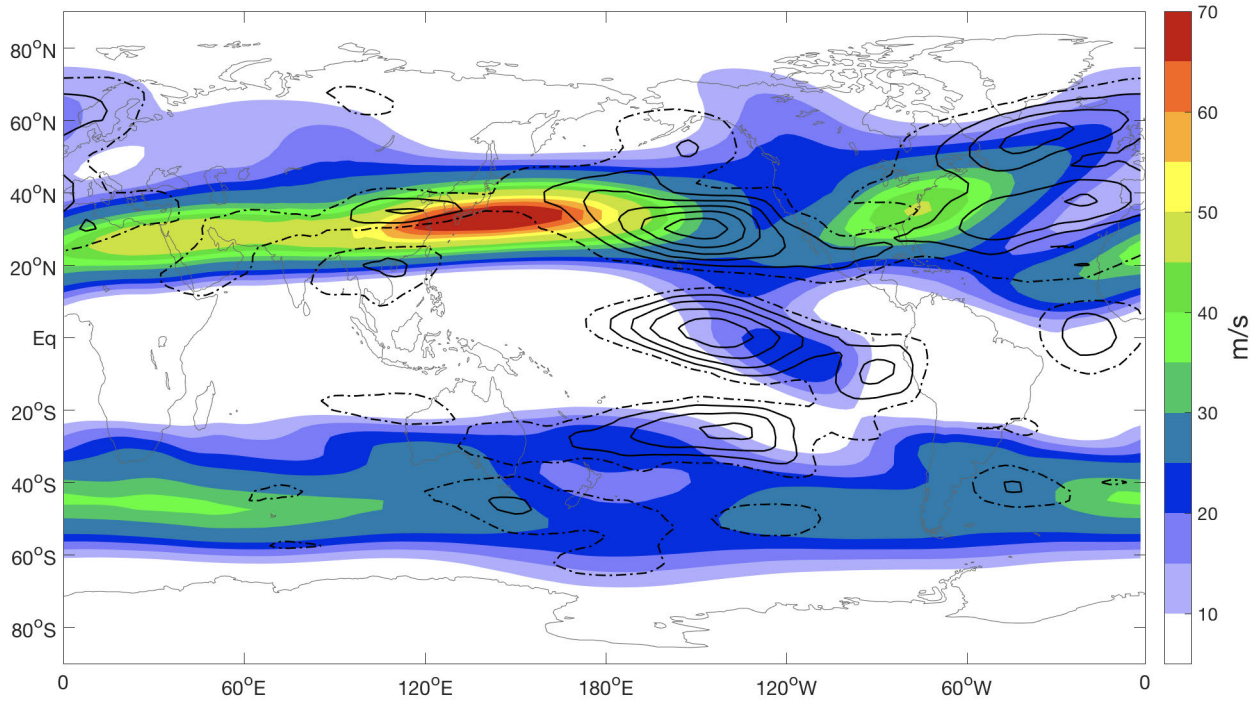

Fig. 3.3. The 200 hPa climatological zonal wind in DJF (shading, ms^{-1}) and the standard deviation of DJF-averaged zonal wind over different years from 1979-2015. Contours start at 5 ms^{-1} with an interval of 1 ms^{-1}. The dashed contour denotes the isoline of 5 ms^{-1}.

observed teleconnections in Figure 3.4. *Held et al.* (1988) noted that a linear model might underestimate the amplitude of tropical-extratropical teleconnections due to the lack of dynamical feedbacks from transient eddies. *Hirota and Takahashi* (2012) also pointed out the lack of diabatic heating feedbacks can lead to an underestimation of teleconnection amplitude. In addition, the nonlinear feedback from zonal mean-eddy interactions that might amplify the teleconnections is also absent in the model (*Kimoto et al.* 2001; *Watanabe and Jin* 2004). Looking more closely at Figure 3.4, we also see that the strongest observed teleconnections are found diagonally (see contours, e.g., similar spatial structure and strength patterns shows up in MJO phase 1, lag 15-19, MJO phase 2, lag 10-14, and MJO phase 3, lag 5-9) while the strongest simulated teleconnections are more concentrated in specific MJO phases. Since the MJO propagates in the real world, where one phase is often followed by the next phase and each phase typically lasts for 5 days, the composited signal is stronger diagonally across phase-lag space in observations than the LBM, where MJO heating is given to the model separately in different phases for both FixQ1 and FixBS. Overall, however, the LBM can

reasonably reproduce the MJO-induced teleconnections observed in the reanalysis data, although with some differences caused by the experimental design and the model dynamics.

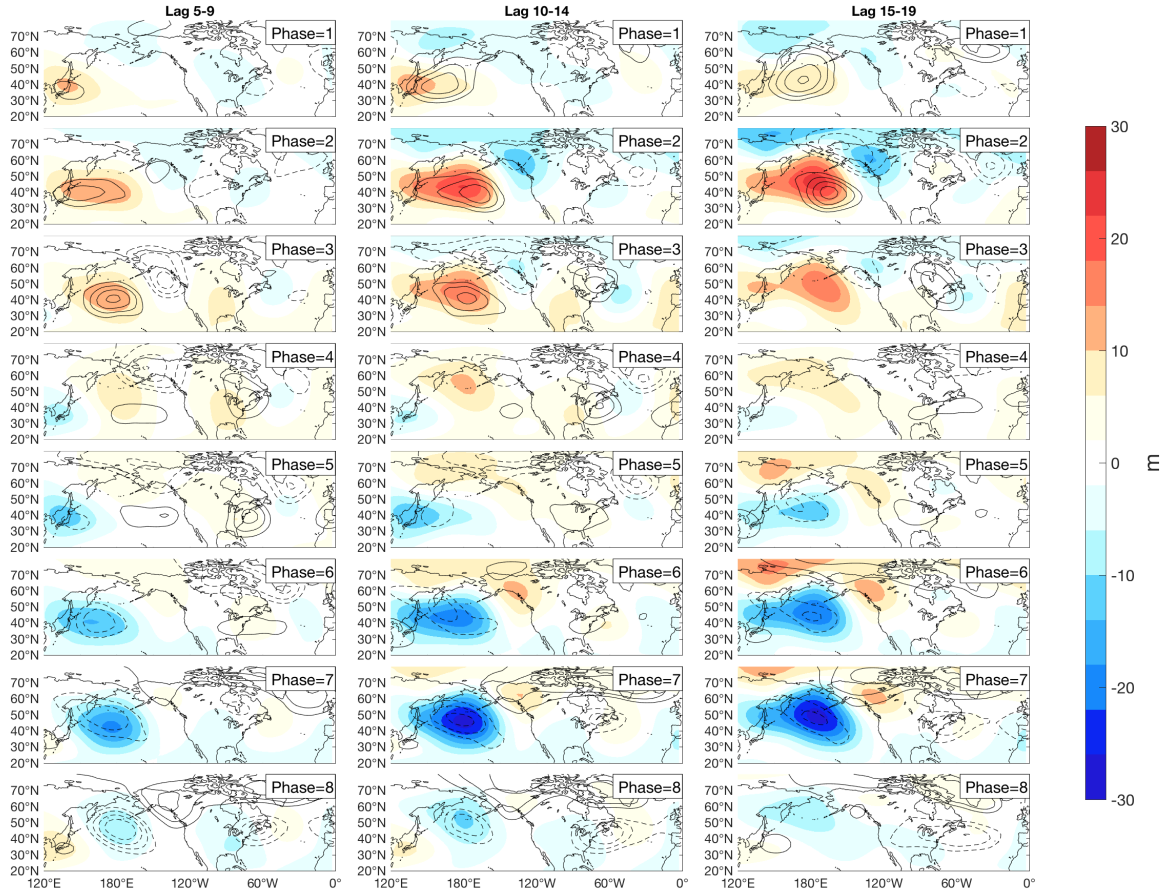

Fig. 3.4. MJO phase- and lag-composites of Z500 in the FixQ1 experiment (m, shading) and ERA-Interim (m, contour). Solid contours denote positive anomalies and dashed contours denote negative anomalies. The contour interval is 10 m starting at +/- 20m.

Comparing the teleconnected patterns between two experiments, the shading in Figure 3.4 and Figure 3.5 generally indicate similar behavior. Both experiments show stronger composited amplitudes in specific MJO phases, such as phases 2, 3, 6 and 7. This suggests two possibilities: (1) The signal is dominated by a few strong simulations in these phases or (2) a similar teleconnection pattern occurs more frequently in these phases compared to others. We provide a more detailed discussion of these possibilities in the next subsection. One notable difference between Figures 3.4 and 3.5 is that the amplitude of composited Z500 is higher in FixBS. Since we conducted these two experiments in a linearized model with identical setups except for the initial conditions, the amplitude of response is directly proportional to the amplitude

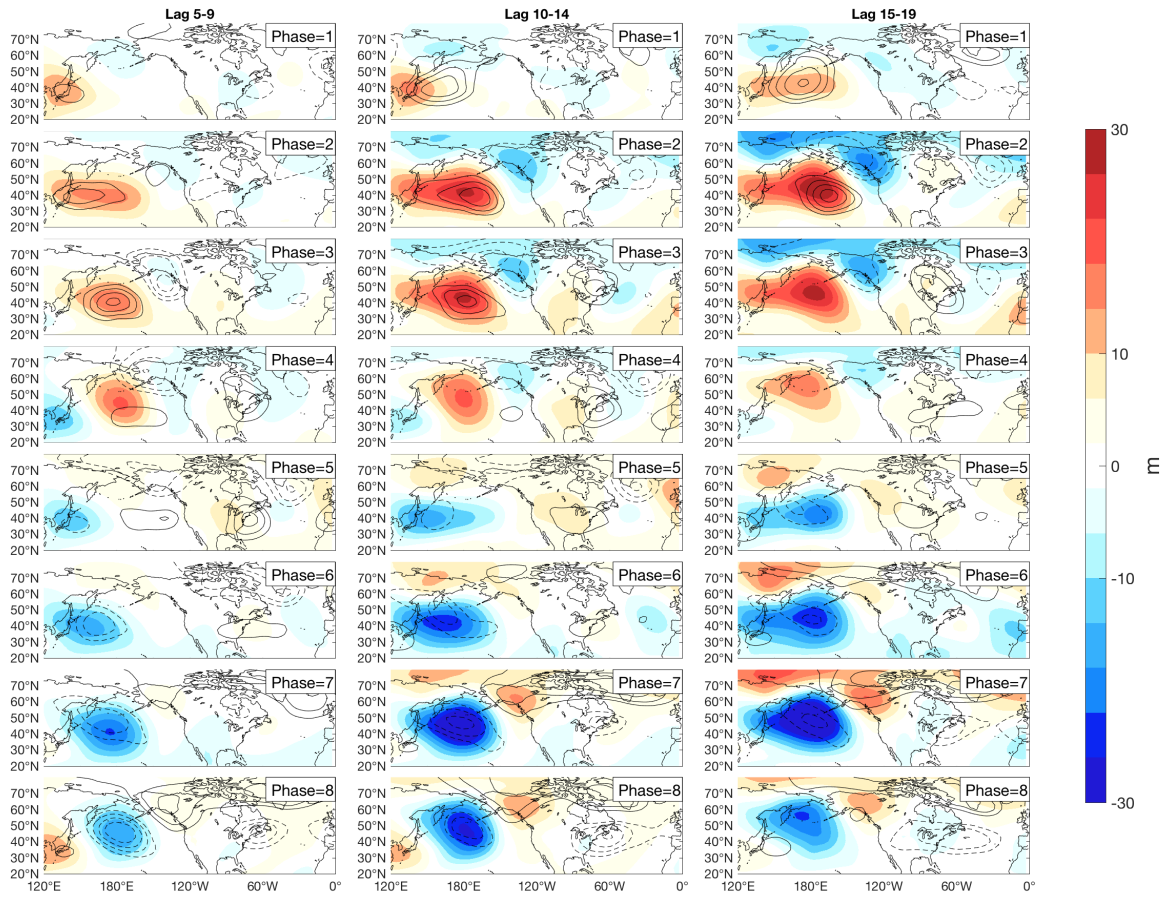

Fig. 3.5. MJO phase- and lag-composites of Z500 in the FixBS experiment (m, shading) and ERA-Interim (m, contour). Solid contours denote positive anomalies and dashed contours denote negative anomalies. The contour interval is 10 m starting at +/- 20m.

of given forcing, especially with the perturbed heating locations occurring in the same general vicinity among events. On average, the amplitude of composited Q_1' in FixQ1 is 40% smaller than the amplitude of individual events in FixBS. Thus, the teleconnected response largely reflects the amplitude difference of the given forcing. One might think that the FixBS and FixQ1 experiments should lead to the same composite amplitude of Z500 since the model used here is linear. However, this would only be true only if the the basic states were identical in FixQ1 and FixBS. Since the basic states are different between these two experiments, FixBS and FixQ1 show different composite amplitudes.

3.3.3 Pattern Consistency in LBM

Since a large composite amplitude could result from only a few dominant MJO events while most of other events are weak, Figure 3.4 and Figure 3.5 provide limited information about the occurrence frequency

of the teleconnection patterns or the pattern consistency over different events. Here, we calculate the pattern correlation of Z500 in the region of 20^oN-70^oN,150^oE-120^oW to quantify the similarity over different model realizations in FixQ1 and FixBS. Figure 3.6(a) is the equivalent plot of Figure 3.1, but for the FixQ1 experiment. The dark colors in Figure 3.6 indicate that more simulation pairs have similar teleconnection patterns and the light colors indicate that fewer simulation pairs have similar teleconnection patterns. In Figure 3.6(a) for FixQ1, high pattern consistency appears right after model initialization and decays with time. Since forcing is identical from one simulation to the next in FixQ1, the tropical response directly induced by the heating should be similar (e.g. resembling the Gill pattern, *Gill* 1980). With increased model lead time, the MJO heating starts to interact with the different basic states. Thus, the pattern consistency dramatically decreases around day 5 for most MJO phases, which is also the e-folding time used to decay the heating. However, some phases show prolonged periods of high pattern consistency (e.g. phases 2, 3, 6, and 7) and these are also the phases showing large amplitudes of composited Z500 in Figure 3.4. After day 30, all MJO phases show relatively low pattern consistency. The trend of decreased pattern consistency over all MJO phases likely results from the different basic states, which determine the ultimate patterns of Z500. One concern is whether the domain selection can influence the results in Figure 3.6(a). To test this, we conducted a series of sensitivity tests by moving the southern boundary northward every 5^o of latitude (not shown). With this shifting of the southern boundary, the high pattern consistency in the early lags decreases, verifying the hypothesis that the high pattern consistency in early lags results from the tropical response directly induced by the heating.

For the FixBS experiment (Figure 3.6b), the percentages of pairs with high pattern consistency is low in the first ten days and then increases for phases 2,3,6,7 and 8 after day 10. The timing of the high pattern consistency in Figure 3.6b corresponds well to the timing of large composite amplitude in Figure 3.5. As we mentioned previously, the Gill-like response is driven by the given heating immediately after model's initialization. The highly diverse Z500 patterns before day 10 could result from different forcings and hence different direct circulation responses at short lead times. One might argue that 500 hPa is a region of near non-divergence in the tropics and hence, subtle changes in the height of non-divergence from one MJO event to the next could produce different signed geopotential height anomalies over different events, making it unlikely to achieve high pattern consistency at small leads. Thus, we conducted another sensitivity test that examined the pattern consistency of the 200 hPa geopotential height anomalies rather than 500 hPa (figure not shown). The calculation based on 200 hPa geopotential height is nearly identical to the calculation based on 500 hPa geopotential height. Thus, the result is not sensitive to the choice of vertical layer. Regardless,

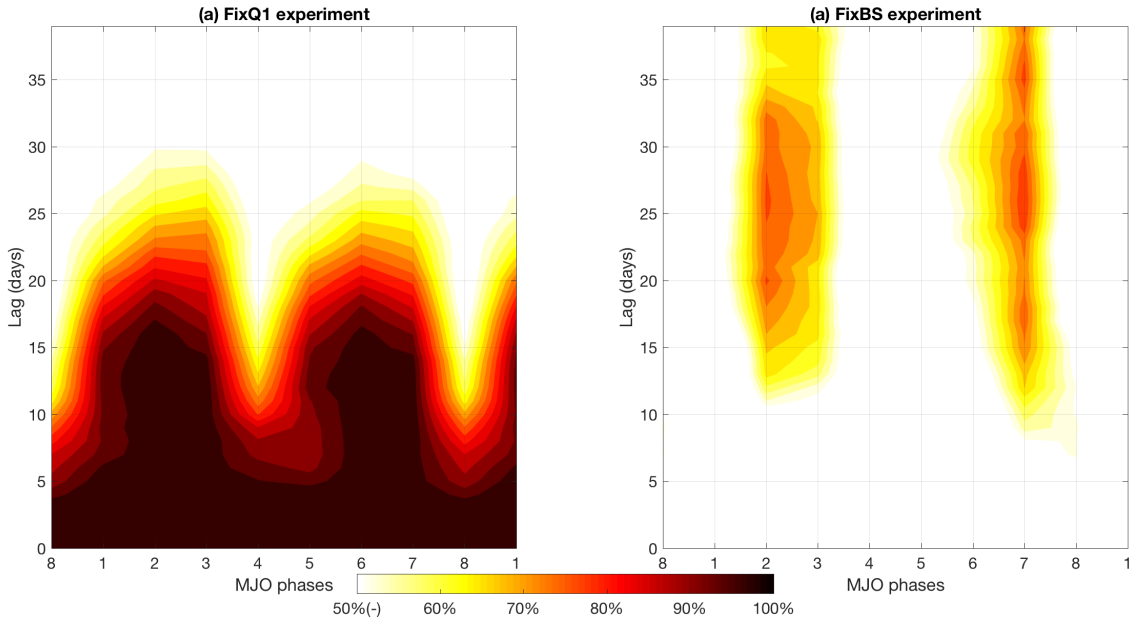

Fig. 3.6. The pattern agreement of Z500 (150^{o}E-120^{o}W,20^{o}N-70^{o}N) over different MJO simulations as quantified by pattern correlations in (a) the FixQ1 experiment and (b) the FixBS experiment. Shading indicates the occurrence frequency of any two simulations with correlation coefficient > 0.5. A value of 100% indicates that all simulation pairs have pattern correlations that exceed 0.5.

even though a variety of heating patterns are given in FixBS, high pattern consistency still appears around day 10 for specific MJO phases, and these are also the phases that show prolonged periods of high pattern consistency in FixQ1. The time lag of 10 days likely arises from the weakening influence of the direct Gill-like responses that vary from event-to-event associated with different heating anomaly structures, and the time it takes to establish the tropical-extratropical teleconnection determined by the basic state and Rossby wave propagation. Note that the phases with higher pattern consistency in FixBS show a longer period of greater consistency (up to day 35) compared to FixQ1, and this is likely caused by the identical basic states in FixBS. Generally, Figure 3.6(a) and Figure 3.6(b) indicate that regardless of modest variations in the basic states and heating patterns, the teleconnection patterns during MJO phases 2, 3, 6 and 7 are very consistent from one realization to the next, suggesting that the geographical location of the heating anomalies (i.e. MJO phase) is responsible for such consistency. This will be explored further in the next section.

3.4 ROSSBY WAVE SOURCE ANALYSIS

3.4.1 Rossby Wave Source Consistency as a Function of MJO Phase in the LBM

To assess the key mechanisms for why heating in specific MJO phases and geographical locations favors consistent teleconnection patterns while others do not, we employ the linearized Rossby wave source based on equation 3.3. The dots in Figure 3.7 show the sign agreement of the linearized Rossby wave source at 200 hPa (S' in equation 3.3) at lag 1 for different MJO phases in FixQ1. Dotted regions indicate that over 70% of the realizations (i.e. more than 25 realizations) agree on a positive sign or negative sign of the linearized Rossby wave source. (Note that since FixBS has similar patterns, we only show the results from FixQ1 here.) In general, Figure 3.7 indicates two interesting features: (1) The regions with high agreement of the Rossby wave source over all MJO phases are all concentrated near the East Asia Jet (110^oE-180^oE, 25^oN-40^oN), and (2) the sign agreement of the linearized Rossby wave source evolves with MJO phase, showing either a symmetric or an asymmetric pattern about 135^oE. The latter point can be explained by examining the terms in 3.3. Two terms in equation 3.3 are associated with energy conversions from the basic state vorticity to the anomalies. The first term, $-\bar{\zeta}\nabla \cdot V'_\chi$, is proportional to the amplitude of the climatological vorticity and the second term, $-V'_\chi \cdot \nabla\bar{\zeta}$, is proportional to the gradient of the climatological vorticity. Typically, the jet regions are characterized by the strongest zonal and meridional wind gradients, thus providing favorable conditions for producing vorticity anomalies and a strong Rossby wave source. As far as the symmetry of the Rossby wave source about 135^oE, because the direction of the anomalous upper-tropospheric divergent wind evolves with MJO phase (vectors in Figure 3.2), the sign of the linearized Rossby wave source is also affected. For example, when the convective signal is located in the eastern Indian Ocean (e.g. MJO phases 2 and 3), the intraseasonal divergent flow at 200 hPa is southwesterly in the eastern Indian Ocean and the Indochina peninsula and northwesterly in the Northwestern Pacific. This kind of divergent flow pattern can result in a negative Rossby wave source to the west of 135^oE (the dashed line in Figure 3.7) and a positive Rossby wave source to the east of 135^oE (see also *Seo and Lee* 2017). In contrast to the MJO heating in the eastern Indian Ocean, anomalous convection in the western Pacific can generate a nearly identical Rossby wave source pattern with opposite sign near the jet regions. In addition, the divergence of the intraseasonal flow (i.e. $\nabla \cdot V'_\chi$) also evolves with MJO phase. When the MJO convection is located in the eastern Indian Ocean, the jet exit region is characterized by the anomalous upper-tropospheric convergence and the jet entrance region is characterized by anomalous divergence. When MJO convection is located in the western Pacific, the jet exit region is characterized by anomalous upper-tropospheric divergence and the jet entrance

region is characterized by anomalous convergence. In general, $-\bar{\zeta}\nabla\cdot V'_\chi$ and $-V'_\chi\cdot\nabla\bar{\zeta}$ add constructively to each other over the eight MJO phases. The other terms in the Rossby wave source are small, consistent with previous studies (e.g. *Seo and Lee* 2017).

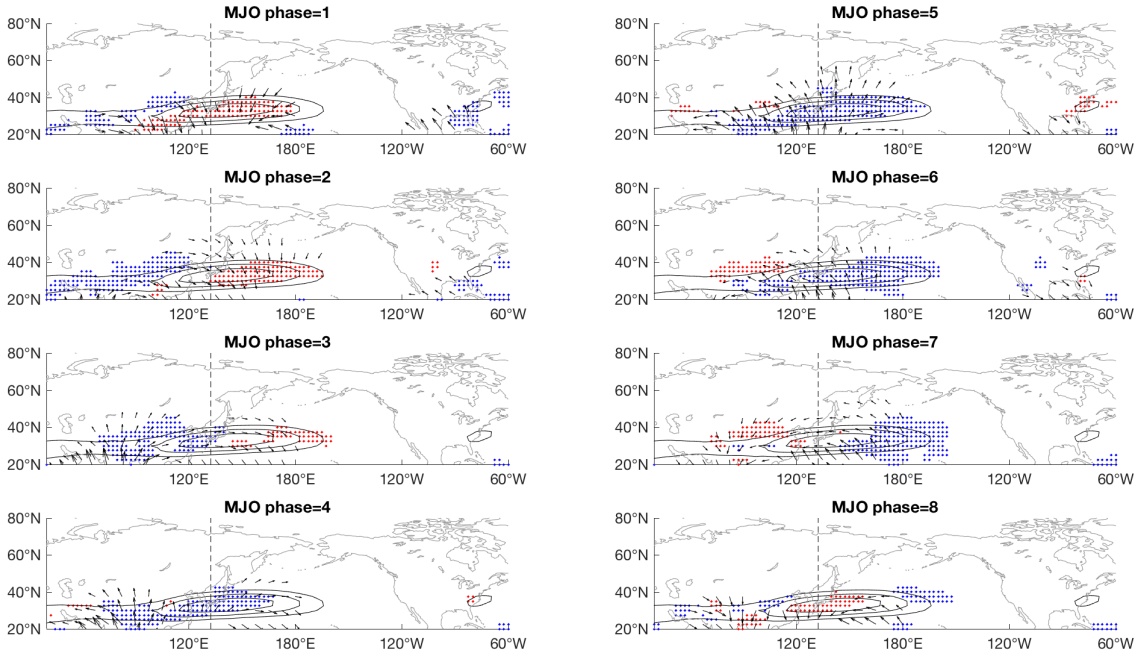

Fig. 3.7. The sign agreement of the 200 hPa anomalous Rossby wave source at a lag of 1 day over different simulations of the FixQ1 simulations. Red dots indicate positive Rossby wave source anomalies with occurrence frequency > 70% and blue dots indicate negative Rossby wave source anomalies with occurrence frequency > 70%. Dashed vertical lines demark 135^{o}E and the contours denote the 200 hPa climatological zonal wind at 45, 55 and 65 ms^{-1}. The vector shows the MJO-phase composited 200 hPa divergent wind in LBM at a lag 1 day; vectors with amplitude smaller than 0.8 (ms^{-1}) are omitted.

3.4.2 The Role of Tropical Heating

Further inspection of Figure 3.7 shows that the phases with more dipole-like patterns of sign agreement of the Rossby wave source are also the phases characterized by higher pattern consistency on S2S time scales (e.g. phases 2, 3, 6, and 7). In addition, these are also the MJO phases showing a dipole heating structure across the eastern Indian Ocean and the western Pacific (Figure 3.2). Thus, we conduct two experiments to clarify the roles of heating in the eastern Indian Ocean and the heating in the western Pacific for generating the dipole-like Rossby wave source and associated tropical-extratropical teleconnection pattern. The first simulation contains positive-only heating from the MJO phase 2 composite (Figure 3.8(a)) and a fixed

climatological basic state. The second simulation has an identical setup to the first simulation except that MJO phase 6 positive-only heating is used (Figure 3.8(b)). We examine the extratropical response 10 days after we prescribe the forcings. Results of the simulations are shown in Figure 3.8(c)-Figure 3.8(f). Figure 3.8(c) and Figure 3.8(d) are the Rossby wave source patterns generated by MJO heating in MJO phase 2 and phase 6 simulations, respectively. Figure 3.8(c) and Figure 3.8(d) indicate that heating both in the eastern Indian Ocean and the western Pacific can generate an asymmetric structure of the Rossby wave source around the jet. The slightly stronger Rossby wave source in the jet entrance region for MJO phase 2, and jet exit region for MJO phase 6, likely results from the proximity of the forcing center. The corresponding teleconnection patterns for the two simulations are shown in Figure 3.8(e) and Figure 3.8(f). Because of the opposite Rossby wave source pattern around the jet regions, Figure 3.8(e) and Figure 3.8(f) show similar PNA-like patterns, but with opposite sign. Due to the linearity of the LBM, the sign of the heating either in the eastern Indian Ocean or the western Pacific can simply be flipped to show that the MJO phases characterized by dipole heating (i.e. phases 2, 3, 6, and 7) are more likely to have strong teleconnection signals because of the constructive superimposition of similar teleconnected patterns. The enhanced signal could lead the MJO-induced teleconnections to emerge from the background variability in the observations and increase the pattern consistency. This result is consistent with *Seo and Lee* (2017) who showed that both anomalous heating in the eastern Indian Ocean and the western Pacific have comparable roles in generating PNA-like teleconnection patterns in the extratropical Pacific. With that said, the simulations above do not directly explain why the MJO phases characterized by a symmetric Rossby wave source have lower pattern consistency. This will be addressed further in the next section, especially when considering Rossby wave sources that are symmetric about $135^o E$.

3.5 DYNAMICS OF CONSISTENT TELECONNECTIONS IN THE REANALYSIS

In section 3.4, we demonstrated that the MJO phases with a more asymmetric pattern of the Rossby wave source are also the phases with more consistent teleconnection patterns in the LBM. Our subsequent heating location tests showed that MJO convection in the eastern Indian Ocean and the western Pacific can generate similar PNA-like patterns, but with opposite sign because of the opposite Rossby wave source generated about the jet. This provides some clue as to why specific MJO phases favor a more consistent tropical-extratropical teleconnection pattern. However, section 3.4 only demonstrated that a single convectively-driven forcing, either in the eastern Indian Ocean or the western Pacific, can generate a dipole structure of Rossby wave source in the LBM across the jet. This does not yet answer, however, why the MJO phases

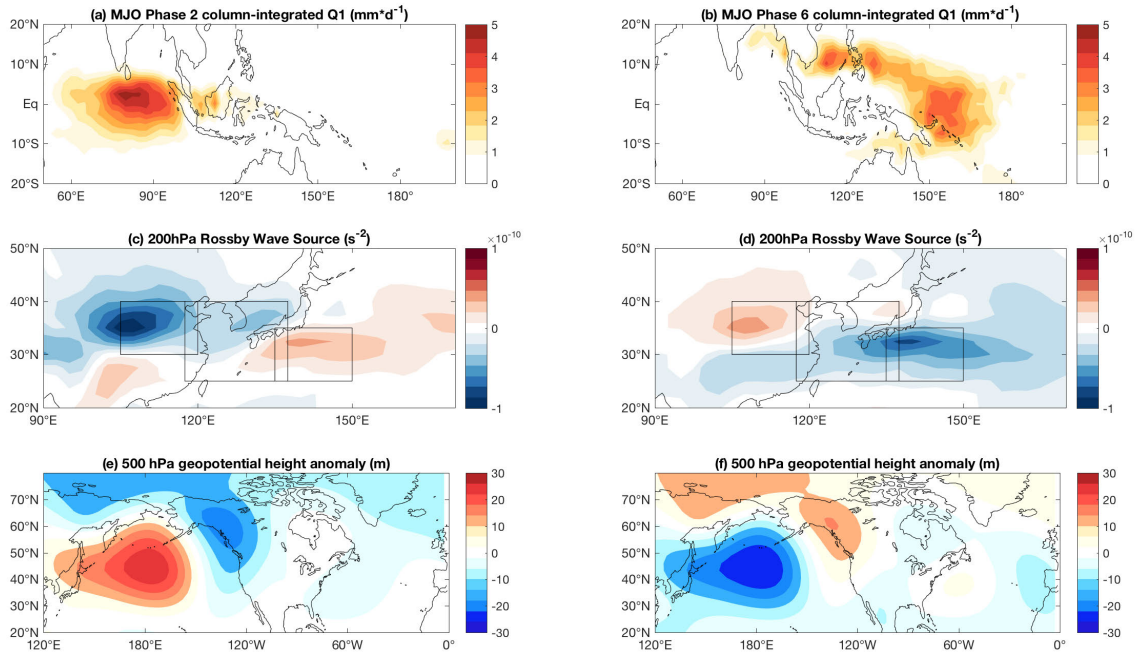

Fig. 3.8. LBM simulations with positive-only heating and the climatological basic state. (a) MJO phase 2 column-integrated Q1 ($mm \cdot d^{-1}$), (b) MJO phase 6 column-integrated Q1 ($mm \cdot d^{-1}$), (c) the 200hPa Rossby wave source generated by heating in Figure 3.8(a), (d) the 200 hPa Rossby wave source generated by heating in Figure 3.8(b), (e) the simulated 500 hPa geopotential height anomaly at lag 10 with heating in Figure 3.8(a) and (f) the simulated 500 hPa geopotential height anomaly at lag 10 with heating in Figure 3.8(b).

characterized by a symmetric Rossby wave source have less consistent teleconnections. Further, all of these tests are based on an LBM. The real world might act in a more complicated manner than a linear system. Thus, in this section, we present a statistical view to examine the relationship between the Rossby wave source around the jet and the pattern consistency of teleconnections in ERA-Interim.

3.5.1 Composite Patterns of Z500 Based on the Rossby Wave Source

To demonstrate how the Rossby wave source across the subtropical jet influences the variability of tropical-extratropical teleconnections in the reanalysis data, we use the standardized time series of the area-averaged Rossby wave source at lag 1 in two reference regions. The first region is located at 105^oE-120^oE, 30^oN-40^oN (EI_{RWS} hereafter, the left box shown in Figure 3.8(c,d)) and the other is located at 135^oE-150^oE, 25^oN-35^oN (WP_{RWS} hereafter, the right box shown in Figure 3.8(c,d)). These two regions are also the regions showing the strongest Rossby wave source signals in Figure 3.8(c) and Figure 3.8(d). The indices are named based on which heating center (eastern Indian Ocean heating or western Pacific heating)

is the more dominant contributor to the Rossby wave source. Figure 3.9 depicts the composited Z500 at lag 10 over the extratropical Pacific for different combinations of EI_{RWS} and WP_{RWS}. From Figure 3.9(c) to Figure 3.9(f), it is found that either strong EI_{RWS} or strong WP_{RWS} can generate PNA-like composite patterns in the extratropical Pacific. For example, when EI_{RWS} is greater than one standard deviation and the amplitude of WP_{RWS} is less than one standard deviation (Figure 3.9(d)), the composited Z500 shows a positive PNA-like pattern with a low pressure anomaly in the North Pacific and high pressure anomaly in Alaska. A nearly opposite pattern of composited Z500 can be found when EI_{RWS} is smaller than minus one standard deviation and the amplitude of WP_{RWS} is smaller than one standard deviation (Figure 3.9(c)). Figure 3.9(e) and Figure 3.9(f) show that WP_{RWS} generates similar teleconnection patterns to EI_{RWS}, except with an opposite sign. In general, the information from Figure 3.9(c) to Figure 3.9(f) suggests that a dipole structure of the Rossby wave source around the jet regions is likely to give rise to an enhanced teleconnection signal while a symmetric Rossby wave source can reduce the teleconnection signal. To verify this point, Figures 3.9(a), 3.9(b), 3.9(g) and 3.9(h) show four scenarios, including the dipole structure of the Rossby wave source and the symmetric structure of the Rossby wave source across the subtropical jet. In Figure 3.9(a) and (b), the composited Z500 shows a similar PNA-like pattern to the composited pattern in panels (e)-(f) but the composited amplitudes are stronger for a dipole structure of the Rossby wave source. In Figures 3.9(g) and (h) for a symmetric Rossby wave source with same sign to either side of 135^oE, the teleconnection pattern is qualitatively different and weaker. These results verify the importance of a dipole Rossby wave structure for producing a robust teleconnection.

Although Figure 3.9 shows that a dipole Rossby wave source can favor a strong Z500 composite pattern, one might argue that the Rossby wave source index defined previously is not representative enough of all MJO phases. According to Figure 3.7, the sign agreement of the Rossby wave source shows either a monopole or a tripole structure in MJO phases 1, 4, 5 and 8. Our earlier two domains filter out the monopole cases. Thus, we revisit the Z500 composite pattern to include the domain averaged value of the Rossby wave source in the region of 117.5^oE-147.5^oE, 25^oN-40^oN (MC_{RWS} hereafter, i.e. the Maritime Continent region, the middle box shown in Figure 3.8(c,d)). Figure 3.10 depicts the Z500 composite patterns at a lag of 10 days for different combinations of MC_{RWS}, EI_{RWS} and WP_{RWS}. In Figure 3.10, we see that the average amplitude of Z500 is weak (typically smaller than 40m) compared with Figure 3.9(a)-3.9(d) when the MC_{RWS} is greater than 1σ or smaller than -1σ. Figure 3.10 implies that the extratropical response is likely to be less sensitive to variations of MC_{RWS}. However, the weak composite amplitude of Z500 can

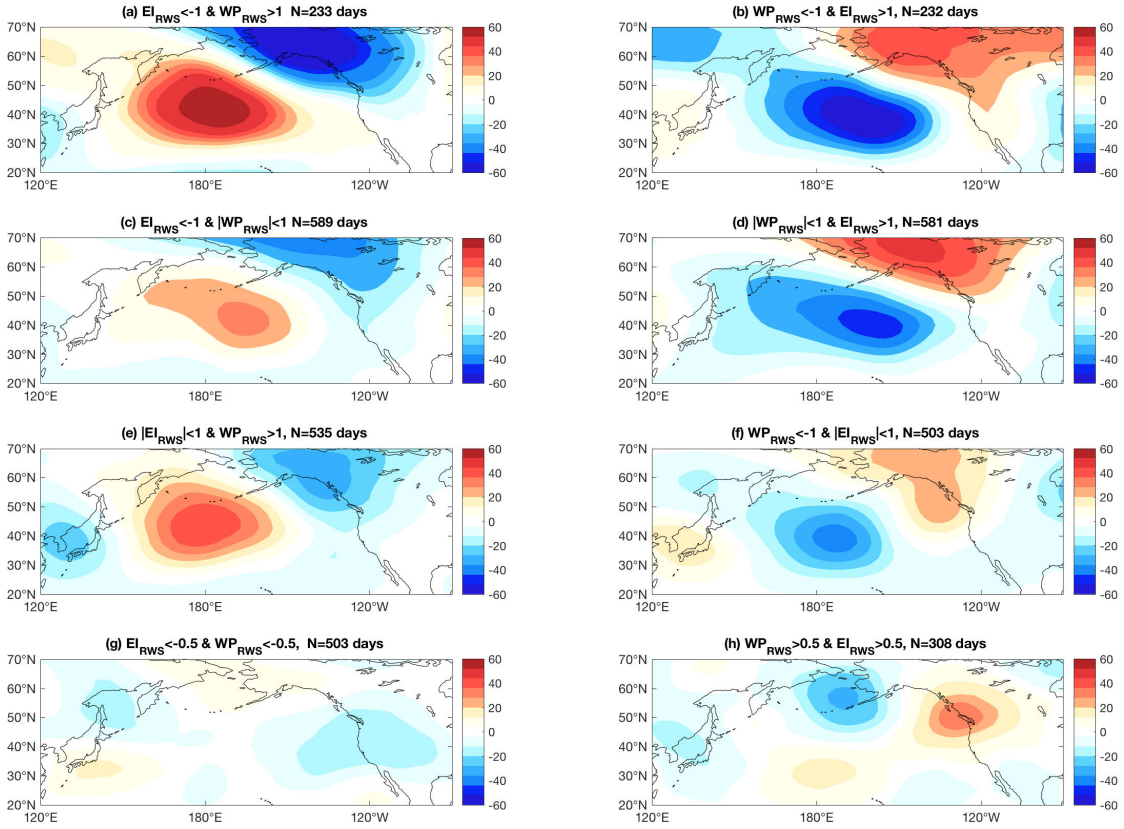

Fig. 3.9. The composited geopotential height anomaly at lag 10 from ERA-Interim for (a) $EI_{RWS} < -1\sigma$ and $WP_{RWS} > 1\sigma$ (b) $WP_{RWS} < -1\sigma$ and $EI_{RWS} > 1\sigma$ (c) $EI_{RWS} < -1\sigma$ and $|WP_{RWS}| < 1\sigma$ (d) $|WP_{RWS}| < 1\sigma$ and $EI_{RWS} > 1\sigma$ (e) $|EI_{RWS}| < 1\sigma$ and $WP_{RWS} > 1\sigma$ (f) $WP_{RWS} < -1\sigma$ and $|EI_{RWS}| < 1\sigma$ (g) $EI_{RWS} < -0.5\sigma$ and $WP_{RWS} < -0.5\sigma$ (h) $EI_{RWS} > 0.5\sigma$ and $WP_{RWS} > 0.5\sigma$. EI_{RWS} is defined as the standardized time series of the domain-averaged Rossby wave source from 105^oE-120^oE and 30^oN-40^oN. WP_{RWS} is defined as the standardized time series of the domain-averaged Rossby wave source from 135^oE-150^oE and 25^oN-35^oN.

arise from strong, but highly varied, patterns over different events or weak amplitudes in individual events. Additional discussion of these issues is presented in section 3.5b.

3.5.2 Pattern Consistency of Z500 According to a Rossby Wave Source-Based Index

In Figure 3.9, the composite analysis showed that the distribution of the Rossby wave source across the subtropical jet can have a strong influence on the composited Z500 signals. Of interest is whether a similar influence is found for the pattern consistency of Z500. To examine this, in Figure 3.11(a) we divide EI_{RWS} and WP_{RWS} into several bins of width 0.5σ. For each bin, the pattern consistency of Z500 at

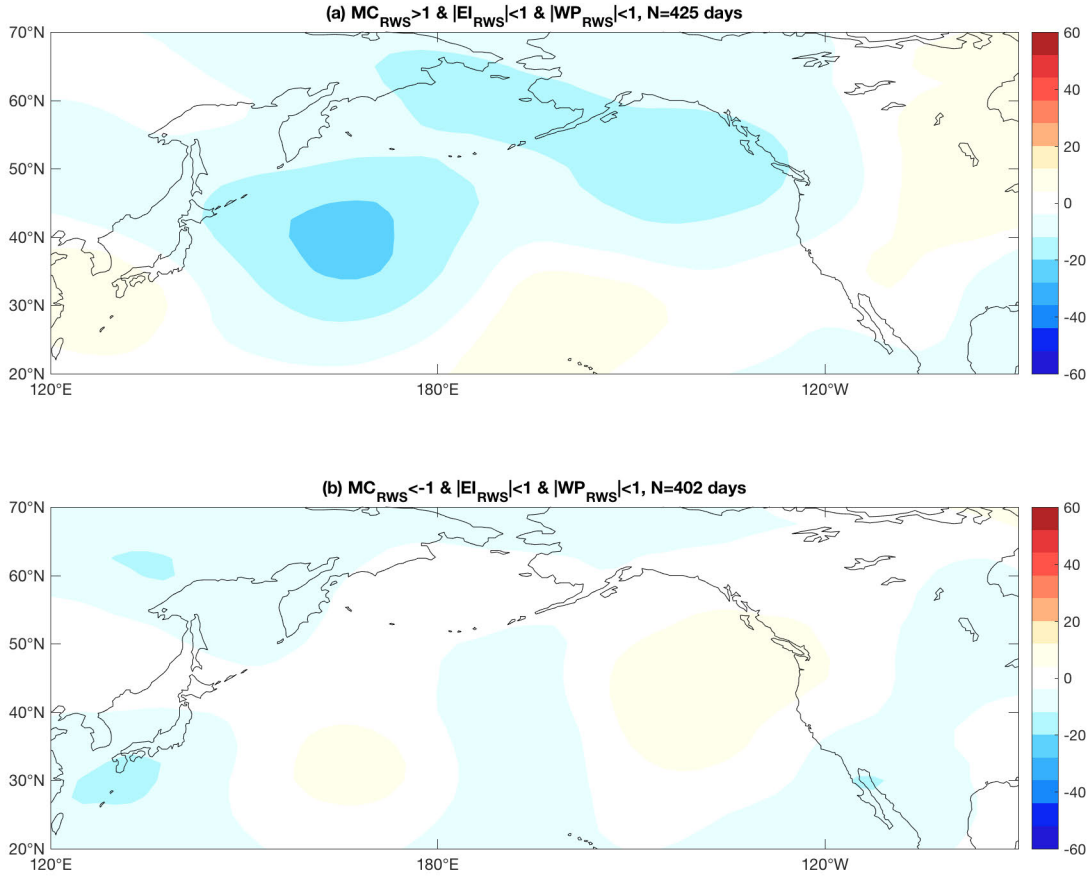

Fig. 3.10. The composited geopotential height anomaly (m) from ERA-Interim for (a) $MC_{RWS} > 1\sigma$, $|WP_{RWS}| < 1\sigma$ and $|EI_{RWS}| < 1\sigma$ (b) $MC_{RWS} < -1\sigma$, $|WP_{RWS}| < 1\sigma$ and $|EI_{RWS}| < 1\sigma$. MC_{RWS} is defined as the standardized time series of the domain-averaged Rossby wave source from 117.5^{o}E-147.5^{o}E and 25^{o}N-40^{o}N.

lag 10 is calculated based on the approach given in section 3.2. If the sample size is less than 30, the calculated value is omitted. The five different dot sizes range from small to large corresponding to different pattern consistencies ranging from 11% to 19% with an interval of 2%. Values below 11% are omitted (the climatological value of pattern consistency is around 11%). Figure 3.11(a) shows that the regions with high pattern consistency are mostly concentrated in the second and the fourth quadrants. These are the quadrants that produce a dipole structure of the Rossby wave source. In addition, the small dots are mostly located in the first and the third quadrants which are the quadrants having a symmetric structure of Rossby wave source. This result verifies the hypothesis in section 3.5a that the constructive superposition of the teleconnections produced by opposite signed Indian Ocean and west Pacific heating not only enhances

the composite amplitude but also increases the pattern consistency of Z500. It further suggests that the destructive interference of teleconnections by the Rossby wave source on each side of the jet can diminish the amplitude of composited Z500 and decrease the pattern consistency in the case of a symmetric Rossby wave source pattern. The high pattern consistency only shows up for amplitudes of the Rossby wave source greater than one standard deviation (dashed line in Figure 3.11(a)). Hence, it suggests that a Rossby wave source of a sufficient strength is needed to produce consistent teleconnection patterns. We also performed additional analysis by replacing the two reference time series of the Rossby wave source with those of Indian Ocean and west Pacific tropical OLR (75^oE-100^oE, $5^oS-7.5^oN$ and 145^oE-170^oE, $5^oS-7.5^oN$) to test more directly how tropical convection influences the pattern consistency in the extratropical regions. The results with the OLR-based time series are qualitatively similar to the Rossby wave source-based time series (results not shown). We additionally examined the Z500 pattern consistency based on MC_{RWS} and the result is shown in Figure 3.11(b). From Figure 3.11(b), it appears that the Z500 pattern consistency is largely independent of MC_{RWS}. The consistency values range from only $11\%-15\%$, which implies that MC_{RWS} is not a strong determinant in producing the Z500 pattern consistency in the extratropical Pacific. Overall, the result in Figure 3.11 demonstrates that dipole structures of Rossby wave source across the jet can generate consistent teleconnection patterns in the extratropical Pacific while a monopole structure does not.

The results shown in Figure 3.10 and Figure 3.11 are based on the Rossby wave source. However, we haven't explicitly looked into the specific role of the MJO in Figure 3.10 and Figure 3.11. Figure 3.12 shows the frequency with which specific MJO phases can generate a dipole structure of a Rossby wave source across the jet at a lag of 1 day (e.g. $EI_{RWS}<0$, $WP_{RWS}>0$ or $EI_{RWS}>0$, $WP_{RWS}<0$). Over 50% of MJO phase 2 and phase 3 events generate Rossby wave sources with $EI_{RWS}<0$ and $WP_{RWS}>0$, and MJO phase 6 and phase 7 have greater than 50% chance of generating a Rossby wave source with $EI_{RWS}>0$ and $WP_{RWS}<0$. Notably, these are also the phases showing consistent Z500 patterns at lag 10-15 in the extratropical Pacific (Figure 3.1). This indicates that the MJO phases that have Rossby wave sources in the second and the fourth quadrants are more likely to generate similar teleconnections pattern due to the constructive interference of PNA-like signals. By contrast, other MJO phases (i.e. phases 1, 4, 5, and 8) with Rossby wave sources evenly distributed across the four quadrants have similar probabilities of generating PNA-like patterns and non-PNA-like patterns. This probability distribution results from the location of MJO heating. Since MJO phases 1, 4, 5 and 8 have anomalous heating located in the Maritime Continent, subtle shifts of horizontal MJO heating structure determine which Rossby wave source on opposite sides of the

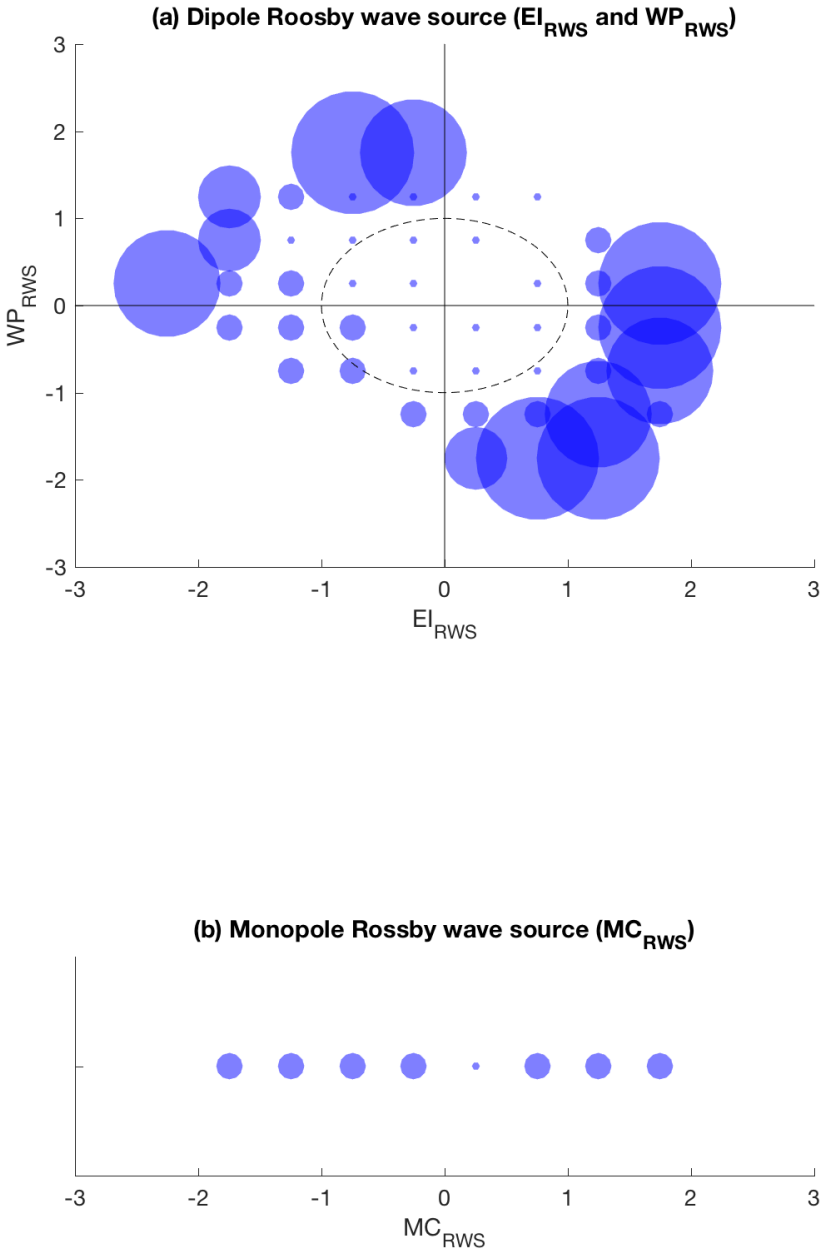

Fig. 3.11. The pattern consistency of 500 hPa geopotential height anomalies at a lag of 10 day in the domain of 150^{o}E-120^{o}W, 20^{o}N-70^{o}N as a function of (a) EI_{RWS} and WP_{RWS} and (b) MC_{RWS}. The intervals of EI_{RWS}, WP_{RWS} and MC_{RWS} are 0.5σ. Five different dot sizes from small to large correspond to the following five different pattern consistency values : 11%-13%, 13%-15%, 15%-17%, 17%-19% and >19%. If the pattern consistency is smaller than 11%, or the sample size is smaller than 30, the value is omitted.

jet dominates the teleconnection pattern. The symmetric pattern of the Rossby wave source generated by these MJO phases is similar to a seesaw with equal weight on each side. Any small perturbation can easily break the balance. Hence, for these phases the pattern consistency is greatly reduced due to event-to-event variability in the precise heating structure.

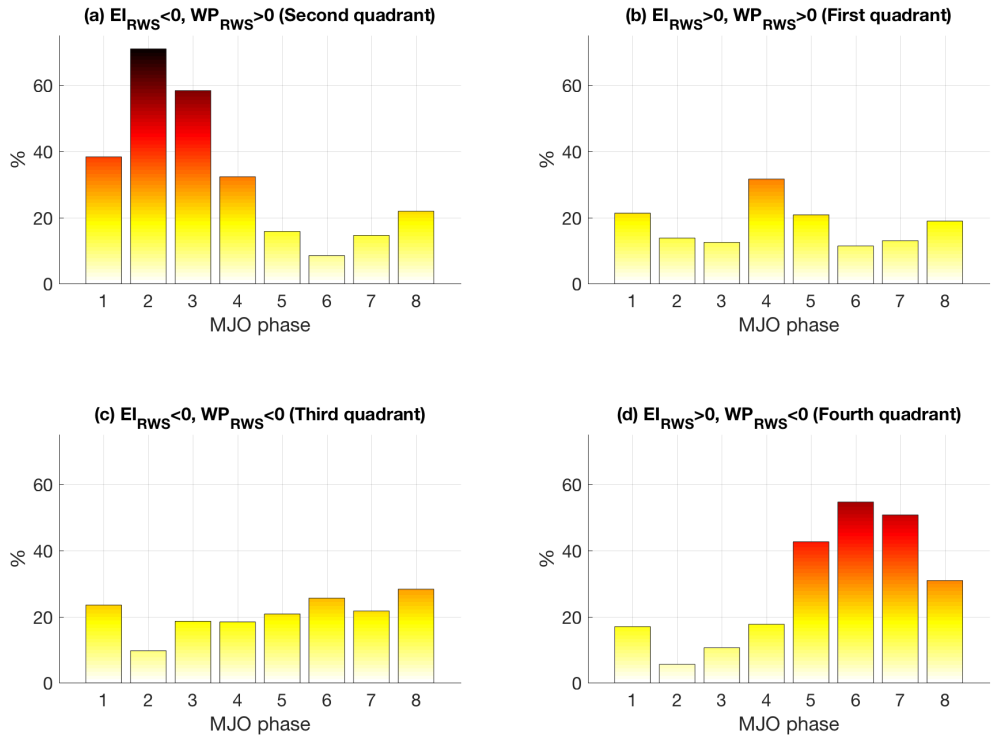

Fig. 3.12. The frequency that specific MJO phases generate a Rossby wave source with (a) $EI_{RWS} < 0$, $WP_{RWS} > 0$, (b) $EI_{RWS} > 0$, $WP_{RWS} > 0$, (c) $EI_{RWS} < 0$, $WP_{RWS} < 0$ and (d) $EI_{RWS} > 0$, $WP_{RWS} < 0$ within ERA-Interim.

3.6 CONCLUSIONS AND REMARKS

Heating induced tropical-extratropical teleconnections play an important role in modulating extratropical circulation patterns and hence weather events. Since the MJO is a dominant mode of variability on intraseasonal time scales, it is intuitive to leverage information about the MJO for S2S time scale prediction in extratropical regions given the strong teleconnections produced by MJO convective heating. The major goal of this study is to examine why specific MJO phases favor a more consistent teleconnection pattern while others do not. In this study, a set of perturbed basic states or perturbed phase-dependent MJO heating

distributions are applied in a linear baroclinic model (LBM) to create an ensemble, and the MJO phase-dependent consistency of teleconnection patterns across the ensemble of simulations is assessed, much as *Tseng et al.* (2018) assessed the pattern consistency in a hincast ensemble. The results indicate that the consistency of the teleconnection pattern is a function of MJO phase which approximately corresponds to the geographical locations of MJO heating anomalies. Teleconnection patterns during MJO phases 2, 3, 6, and 7 are less sensitive to modest variations of the basic state and anomalous heating patterns compared to other MJO phases. An explanation for this phase-dependent pattern consistency is proposed by calculating the sign agreement of linearized Rossby wave source over different model realizations. Phases with a more dipole-like pattern of anomalous Rossby wave source on the east and west side of the Pacific jet are also the phases showing higher pattern consistency of teleconnections in both model and reanalysis. Heating location tests also demonstrate that both MJO convection in the eastern Indian Ocean and the western Pacific generate similar asymmetric Rossby wave source patterns and teleconnections in the LBM, except with opposite sign. Given the linearity of the model, this result implies that an enhanced teleconnection signal may appear for the phases with a dipole-type pattern of Indo-Pacific warm pool heating and a dipole Rossby wave source along the jet because of the constructive interference of similar teleconnection patterns. However, it also implies that other phases with less significant Z500 composite patterns may be caused by the lack of a dipole structure, and thus, more variability in the teleconnection pattern from event-to-event. In the last section, the relationship between the Rossby wave source on each side of the jet and the robustness of tropical-extratropical teleconnections in reanalysis data is examined, initially without explicit consideration of the MJO. The analysis showed that an asymmetric Rossby wave source pattern zonally across the jet not only enhances the composited amplitude of Z500, but also increases the pattern consistency of Z500 over different events, as was found in the LBM. The MJO-induced teleconnection results can be regarded as a special case of this behavior.

This study gives a possible explanation for the phase-dependent pattern consistency of Z500 described in *Tseng et al.* (2018), who found that robust tropical-extratropical teleconnections for certain MJO phases can benefit S2S time scale weather prediction. However, a number of unanswered questions still exist. First, will the MJO phase-dependent pattern consistency change when other low-frequency variability is considered? Since other modes of climate variability (e.g. quasi-biennial oscillation or ENSO) modulate MJO activity including MJO propagation speed and convection intensity as well as the basic state, it would be interesting to examine how these modes of climate variability affect MJO phase-dependent pattern consistency. Second, the mechanisms discussed in this study are based on linear dynamics, but nonlinear feedbacks may also be

important. For example, *Watanabe and Jin* (2004) showed that the subtropical jet is an amplifier for tropical-extratropical teleconnections through zonal mean-eddy feedback processes. How such feedbacks influence the robustness of tropical-extratropical teleconnections is still an ongoing area of research.

The results of this study provide a compelling explanation for the MJO phase-dependent consistency of teleconnection patterns first described in *Tseng et al.* (2018) by invoking linear Rossby wave dynamics. This study also gives a possible explanation for why MJO phases with consistent teleconnections are also characterized by small model ensemble spreads and improved prediction skills. However, the nonlinear dynamics and interaction between physics schemes in a numerical weather forecast system are more complicated than the linearized dynamical core used in this study. Thus, relating our results to these more complex dynamical forecast systems requires additional future research.

CHAPTER 4

The consistency of MJO teleconnection patterns on interannual timescales [3]

The Madden-Julian Oscillation (MJO) excites strong variations in extratropical geopotential heights which modulate extratropical weather, making the MJO an important predictability source on subseasonal to seasonal timescales (S2S). Previous research demonstrates a strong similarity of teleconnection patterns across MJO events for certain MJO phases (i.e. pattern consistency) and increased model ensemble agreement during these phases that is beneficial for extended numerical weather forecasts. However, the MJO's ability to modulate extratropical weather varies greatly on interannual timescales, which brings extra uncertainty in leveraging the MJO for S2S prediction. Few studies have investigated the mechanisms responsible for variations in the consistency of MJO tropical-extratropical teleconnections on interannual timescales. This study uses reanalysis data, ensemble simulations of a linear baroclinic model, and a Rossby wave ray tracing algorithm to demonstrate that two competing mechanisms largely determine the interannual variability of MJO teleconnection consistency. First, the meridional shift of ray paths associated with stationary Rossby wave propagation indicate increases (decreases) in the MJO's extratropical modulation during La Niña (El Niño) years. Second, a previous study proposed that the constructive interference of Rossby wave signals caused by a dipole Rossby wave source pattern across the subtropical jet during certain MJO phases produces a consistent MJO teleconnection. However, this dipole feature is less clear in both El Niño and La Niña years due to the extension and retraction of MJO convection, which would decrease the MJO's influence in the extratropics. Hence, considering the joint influence of the basic state and MJO forcing, this study suggests a diminished potential to leverage the MJO for S2S prediction in El Niño years

4.1 INTRODUCTION

Subseasonal to seasonal (S2S) timescales (2-5 weeks) - timescales longer than medium-range weather forecasts and shorter than seasonal outlooks - have long been recognized as a prediction desert (*Hamill and Kiladis* 2014), and developing skillful predictions in this window will provide tangible benefits to human society. A growing body of research has been conducted exploring the potential to leverage low-frequency modes of variability (> 2 weeks) for S2S prediction (*Vitart et al.* 2017). Given that the Madden-Julian oscillation (MJO) is a mode of tropical convective variability characterized by planetary-scale circulations and

[3]This chapter contains material that will be submitted in the *Journal of Climate* as: Tseng, K-C., E. Maloney, and E. Barnes, 2019: The consistency of MJO teleconnection patterns on interannual timescales

intraseasonal timescales (*Madden and Julian* 1971; *Adames and Kim* 2016), it has been considered one of the most important predictability sources on S2S timescales. While the MJO produces a direct modulation of tropical weather such as the tropical cyclone genesis (*Liebmann et al.* 1994; *Maloney and Hartmann* 2000), the initiation of El Niño/Southern oscillation (ENSO) events (*Moore and Kleeman* 1999), and the diurnal cycle in the Maritime continent(*Kanamori et al.* 2013), the MJO's impacts extend well beyond the tropics. Indeed, some of the most impactful weather phenomena in the extratropics, such as atmospheric rivers (*Mundhenk et al.* 2016; *Mundhenk et al.* 2018), anticyclonic blocking (*Henderson et al.* 2016) and extreme cold air outbreaks (*Yoo et al.* 2012) are modulated by the MJO through tropical-extratropical teleconnections. By generating upper-troposphere divergent flow which interacts with the subtropical jet, the MJO excites quasi-stationary Rossby waves that propagate into the extratropics and consistently modulate extratropical weather (*Hoskins and Karoly* 1981; *Sardeshmukh and Hoskins* 1988).

A recent study showed that the landfall frequency of atmospheric rivers in coastal California can increase or decrease by 40% in specific MJO phases compared to climatology due to the low-frequency variation of geopotential height associated with MJO teleconnections. An empirical model using the MJO as a predictor provides skillful prediction of atmospheric rivers at forecast leads of 3 weeks, and an additional 2 weeks of skill are obtained when the quasi-biennial oscillation (QBO) is included as a predictor (*Mundhenk et al.* 2018). In addition to empirical prediction, MJO teleconnections also benefit the prediction skill of operational forecast systems. For example, a recent study demonstrated that a more consistent teleconnection pattern from event to event (i.e. pattern consistency) found in MJO phases 2, 3, 6 and 7 is also characterized by excellent agreement in the prediction of geopotential height anomalies across model ensemble members at forecast leads of up to 3 weeks (*Tseng et al.* 2018)(chapter 2).

The MJO's ability to modulate extratropical weather, however, may vary on interannual timescales. For example, previous studies demonstrate that the QBO can dramatically change MJO intensity and propagation speed, which can modulate the MJO's extratropical teleconnections (*Mundhenk et al.* 2018). Thus, the influence of the El Nino-Southern Oscillation (ENSO) on the consistency of MJO teleconnections necessitates investigation. ENSO represents a recharge or discharge of warm water volume in the equatorial Pacific, with a period of 2-7 years (*Jin* 1997). ENSO has been documented to influence convective activity of the MJO, including its intensity and the propagation speed (*Pohl and Matthew* 2007). In El Niño years, MJO convection tends to be stronger over the western and central Pacific and is characterized by a faster propagation speed, while La Niña years indicate the opposite behavior (*Pohl and Matthew* 2007; *Henderson and Maloney* 2018). ENSO also modulates the strength and position of the subtropical jet and extratropical

geopotential heights and through its impact on tropical-extratropical teleconnections (*Bjerknes* 1969). Due to ENSO's widespread influence on both basic states and MJO forcing, the consistency of MJO teleconnections and the predictability of the associated extreme weather are expected to be modulated by ENSO in potentially complex ways.

This work uses reanalysis data, ensemble simulations of a linear baroclinic model, and a Rossby wave ray tracing algorithm to investigate the mechanisms underlying ENSO-induced interannual variability of MJO teleconnections and their consistency. The results are interpreted through the theoretical lens of linear Rossby wave theory, where the wave growth and propagation are assumed to follow the first-order approximation of the linearized barotropic vorticity equation. In particular, a meridional shift of the Rossby wave ray paths modulated by ENSO that lead to changes in the consistency of the MJO teleconnection will be highlighted in this research. In addition, the role of intraseasonal Rossby wave source modulated by ENSO in influencing the consistency of the MJO teleconnection will also be elucidated. This manuscript is organized as follows. In section 4.2, a description of data, the linear baroclinic model (LBM), and methods are provided. In section 4.3, the pattern consistency of MJO teleconnections in different ENSO states in reanalysis fields is discussed. In section 4.4, the mechanisms that determines variations in the pattern consistency of MJO teleconnections with ENSO are investigated through ensemble simulations of the LBM and use of a Rossby wave tracing algorithm. Section 4.5 presents conclusions and discussion.

4.2 DATA, MODEL AND METHOD

4.2.1 Linear Baroclinic Model

4.2.1.1 Model description

The linear baroclinic model (i.e. LBM) developed by *Watanabe and Kimoto* (2000) is used in this study. In the LBM, the hydrostatic primitive equations are linearized about a basic state and the anomalous response for a given forcing is calculated, allowing the influence of basic state variability and MJO forcing to be separated. Following the LBM setup of *Tseng et al.* (2019) (chapter 3), T42 horizontal resolution ($\sim 2.8^o$) and 20 sigma levels are used. Numerical damping, including Rayleigh friction and Newtonian cooling, is employed in the LBM with an e-folding timescale of 20 days in most vertical layers, while the top and the bottom layer have a damping timescale of 0.5 day. These parameters were employed previous studies demonstrating reasonable simulation of MJO teleconnection patterns (*Tseng et al.* 2019) (chapter 3).

4.2.1.2 Model Basic state and MJO Forcing

To generate model basic states, the European Centre for Medium-Range Weather Forecasts (ECMWF) third generation reanalysis product (ERA-Interim, *Dee at al.* (2011)) from 1979 to 2015 is used. Five variables including surface pressure, specific humidity, horizontal momentum, and temperature are used to define the basic state in the LBM. The basic states are associated with the linear operator of the LBM, which remains unchanged during the period of the integration. To examine how different climate states influence the pattern consistency of the MJO teleconnections, we further define the ENSO phase based on the monthly NINO3.4 index, which was acquired from https://www.esrl.noaa.gov/psd/gcos_wgsp/Timeseries/Nino34/. A warm ENSO phase (i.e. El Niño) is defined as when the NINO3.4 index is greater than 1^oC, and a cold ENSO phase (i.e. La Niña) occurs when the NINO3.4 index is colder than -1^oC, and neutral conditions are identified as when the index doesn't meet either criterion. Since MJO teleconnections are stronger during boreal winter than other seasons, we only use data during November to March (referred to as extended boreal winter hereafter). Basic states are then defined by the boreal winter average values.

For the model forcing, the daily apparent heat source (i.e. Q_1, equation 4.1) is derived from the budget residual of the thermodynamic energy equation (*Yanai et al.* 1973).

$$Q_1 \equiv \frac{Ds}{Dt} \cong Q_R + Q_c - \frac{\partial \overline{s'w'}}{\partial p} \tag{4.1}$$

In equation 4.1, $\frac{Ds}{Dt}$ is the material derivative of the dry static energy (i.e. s, which is defined as $c_p T + gz$. c_p is the specific heat and g is the gravitational acceleration), Q_R is the radiative heating or cooling, Q_c is the latent heat release, $-\frac{\partial \overline{s'w'}}{\partial p}$ is the convergence of the eddy heat flux by convection or boundary layer turbulence and w is the pressure velocity. In general, the apparent heat source is positive when convective heating is dominant. An intraseasonal band-passed filter (20-100 days) is applied to the obtain the MJO heating anomaly. In addition, a Gaussian mask with maximum on the equator and e-folding scale of 15^o in the meridional direction (e.g. $e^{\frac{-\phi}{15^2}}$) is applied to the heating to ensure extratropical signals are excited only by remote forcing in the tropics.

4.2.1.3 Experimental Design

ENSO can modulate MJO teleconnections through two distinct pathways: (1) by modulating the basic state and (2) by modulating the MJO forcing (see discussion in section 4.3). Therefore, we can examine the influence from each component by either fixing or changing the basic states or the MJO forcing in the LBM. Overall, seven different ensemble simulations are conducted named: (1) bs.neutral.frc.neutral, (2) bs.El

Niño.frc.neutral, (3) bs.La Niña.frc.neutral, (4) bs.neutral.frc.El Niño, (5) bs.neutral.frc.La Niña, (6) bs.El Niño.frc.El Niño and (7) bs.La Niña.frc.La Niña. The simulations are named after the nature of the basic states and MJO forcing used in the particular simulation. For example, the simulation "bs.neutral.frc.neutral" indicates both the basic states ('bs') and the MJO forcing ('frc') are acquired from ENSO neutral years. For an individual simulation within an ensemble, the MJO forcing is generated by compositing 200 randomly sampled MJO days for a given MJO phase when the OLR MJO index (see next section for definition) reaches or exceeds 1σ at lag 0. The resampling process is repeated 30 times to acquire 30 ensemble members. According to the central limit theorem, when the independent random variables are added, their normalized sum tends toward a normal distribution even if the original structure is not normal. The preprocessing used ensures that the perturbations to the MJO forcing form a normal distribution for each MJO phase, which is consistent with the preprocessing used to generate ensemble simulations for numerical weather forecasts in operational centers (*Christiansen* 2019).

Previous studies have shown that the teleconnections generated by earlier MJO phases can interfere with teleconnections generated by subsequent MJO phases due to the circumnavigating nature of MJO convection (ref). Also, heating-induced teleconnections take 10 days to develop. Therefore, an additional 10 days of MJO forcing prior to lag 0 are given to the LBM to mimic real world conditions. Figure 4.1 demonstrates one of the MJO phase 6 forcing evolutions given to the LBM acquired from neutral years (shading). In Figure 4.1, the MJO forcing is characterized by a phase 6 lag 0 heating structure with a negative heating in the Eastern Indian ocean and a positive heating in the Western Pacific. With increasing lag, the MJO forcing propagates eastward and decays around the date line, which is consistent with observed features in previous studies (*Hendon and Zhang* 2007). The contours represent the standard deviation of the MJO forcing over different ensemble members, which demonstrates the longitudes where the MJO forcing is most strongly perturbed. The above forcing preprocessing enables examination of the effects of interannual variability of MJO forcing, including the change in intensity over different ocean basins and the eastward extension or the westward retraction of MJO convection in the Western Pacific.

4.2.2 Observational Reference

4.2.2.1 500hPa geopotential height anomalies

Thirty-seven years (1979-2015) of daily 500hPa geopotential height (Z500 hereafter) data from ERA-Interim is used to represent MJO teleconnections. Since the tropical-extratropical teleconnections are characterized by a barotropic structure, the precise selection of vertical pressure level does not qualitatively affect

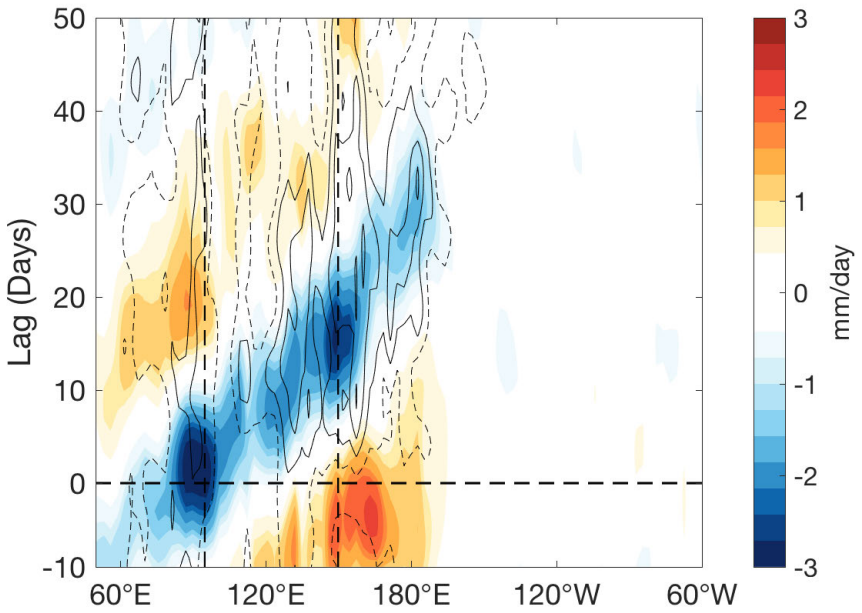

Fig. 4.1. The column-integrated apparent heat source relative to MJO events defined at MJO phase 6, lag 0. The contour represents the standard deviation over different ensemble members, which begins at 0.7 mmd^{-1} with an interval of 0.1 mmd^{-1}.

the conclusions of this study. The daily anomalous Z500 is acquired by removing the first three harmonics of the seasonal cycle. In this study, we are also interested in ENSO's indirect effect on tropical-extratropical teleconnections through modifying the MJO forcing and the basic state upon which MJO teleconnections propagate. Thus, we also apply an intraseasonal band-pass filter to the total z500 anomaly field to remove extratopical anomaly signals directly generated by ENSO. In this study, both total and intraseasonal Z500 anomaly data are interpolated to a horizontal resolution of 2.5^o by 2.5^o.

4.2.2.2 MJO phases

The evolution of MJO convection is defined by the OLR-based MJO index (OMI), which can be acquired from https://www.esrl.noaa.gov/psd/mjo/mjoindex/. One advantage of using OMI rather than other MJO indices is that tropical convection plays a major role in perturbing the upper-troposphere vorticity field and generating tropical-extratropical teleconnections. Other MJO indices defined by several fields, such as real time monitoring MJO index (RMM), are typically dominated by the wind field while convective variability explains little variance of the index. MJO phase is then defined by $tan^{-1}(OMI2/OMI1)$, where OMI1 and OMI2 are the principal components of the first two empirical orthogonal functions of the equatorially averaged (15^oN-15^oS) OLR fields. Only days with $\sqrt{OMI1^2 + OMI2^2}$ greater than 1σ are used in our analysis.

4.2.3 Method

4.2.3.1 Quantifying pattern consistency

Following the method of *Tseng et al.* (2019) (chapter 3), the pattern consistency of MJO teleconnections is calculated to quantify the robustness of the teleconnection signals. An area-weighted pattern correlation coefficient is determined for every pair of MJO events (or ensemble members) in a domain over the North Pacific and North America (20^o-70^oN, 150^oE-120^oW). For an ensemble with 30 members, there are 435 correlation coefficients. By estimating the fraction of pairs with a correlation coefficient that meet or exceed a certain criteria (0.5 in this study), the pattern consistency of the MJO teleconnection over different phases and time lags can be quantified. *Tseng et al.* (2018) (chapter 2), in which ENSO state was not considered, showed that the MJO phases with higher pattern consistency from event to event in observations are also characterized by better agreement across numerical weather prediction model ensemble members in predicted extratropical geopotential height anomalies.

4.2.3.2 Linearized Rossby wave source

To better understand the dynamics of the circulation response to MJO forcing, we use the linearized barotropic vorticity equation (*Sardeshmukh and Hoskins* 1988):

$$\frac{\partial \zeta'}{\partial t} = S' - \bar{\mathbf{v}}_\psi \cdot \nabla \zeta' - \mathbf{v}_\psi' \cdot \nabla \bar{\zeta} + F' \tag{4.2}$$

where the prime indicates perturbations (intraseasonal timescales) and the overbar is the climatology; ζ is the absolute vorticity, $\mathbf{v}_\psi$ is the rotational wind including zonal (u_ψ) and meridional components (v_ψ), F' is frictional and S' is the Rossby wave source. In equation 4.2, the rotational wind redistributes the vorticity field, associated with Rossby wave propagation and S' is related to Rossby wave production. S' can be expanded in the following form:

$$S' = -\nabla \cdot (\bar{\zeta} \mathbf{v}_\chi' + \bar{\mathbf{v}}_\chi \zeta') = -\bar{\zeta} \nabla \cdot \mathbf{v}_\chi' - \mathbf{v}_\chi' \cdot \nabla \bar{\zeta} - \zeta' \nabla \cdot \bar{\mathbf{v}}_\chi - \bar{\mathbf{v}}_\chi \cdot \nabla \zeta' \tag{4.3}$$

In equation 4.3, $\mathbf{v}_\chi$ is the non-rotational component of the horizontal wind. The physical meaning of equation 4.2 and 4.3 is that generation of the anomalous Rossby wave ($\frac{\partial \zeta'}{\partial t}$) is associated with the stretching and advection of the climatological absolute vorticity by the anomalous divergent flow (i.e. $-\nabla \cdot (\bar{\zeta} \mathbf{v}_\chi')$) and the stretching and advection of the anomalous absolute vorticity by the climatology divergent flow (i.e. $-\nabla \cdot (\bar{\mathbf{v}}_\chi \zeta')$). The Rossby wave source term (S') is especially notable in regions of convective activity where there is strong divergent outflow that impinges upon a strong background vorticity gradient (e.g. the subtropical jet).

4.2.3.3 Rossby wave ray tracing algorithm

We use a Rossby wave ray tracing algorithm (*Karoly* 1983) to investigate how interannual variability of wave propagation influences the pattern consistency of MJO teleconnections. As noted previously, wave propagation is largely regulated by the rotational flow. Thus, to understand Rossby wave propagation in a nearly barotropic flow, which is a good assumption in the mid-latitude upper troposphere, the rotational component of equation 4.2 can be isolated. Further, by replacing the vorticity (ζ') with stream function ($\nabla^2\psi'$), equation 4.2 can be rewritten in the following form:

$$\frac{\partial \nabla^2\psi'}{\partial t} + (\bar{\mathbf{v}}_\psi \cdot \nabla)\nabla^2\psi' - \psi'_x\bar{\zeta}_y + \psi'_y\bar{\zeta}_x = 0 \tag{4.4}$$

In equation 4.4, ∇^2 is the horizontal Laplace operator, $-\psi'_x$ indicates the rotational component of the anomalous meridional wind (v'_ψ), ψ'_y represents the rotational component of the anomalous zonal wind (u'_ψ), $\bar{\zeta}_y$ is the meridional gradient of the absolute vorticity and $\bar{\zeta}_x$ is the zonal gradient of the absolute vorticity. Since $\psi'_y\bar{\zeta}_x$ and $\bar{v}_\psi\frac{\partial}{\partial y}\nabla^2\psi'$ in $(\bar{\mathbf{v}}_\psi \cdot \nabla)\nabla^2\psi'$ are negligible compared to the other terms, equation 4.4 can be simplified as:

$$\frac{\partial \nabla^2\psi'}{\partial t} + \bar{u}_\psi\frac{\partial}{\partial x}\nabla^2\psi' - \psi'_x\bar{\zeta}_y \approx 0 \tag{4.5}$$

Using so-called Wentzel-Kramers-Brillouin (WKB) theory for approximating solutions to (5), the following dispersion relationship can be generated:

$$\omega = \bar{u}_\psi k - \frac{\bar{\zeta}_y k}{k^2 + l^2} \tag{4.6}$$

where ω is the frequency, k is the zonal wave number, l is the meridional wave number, and the total wave number K is defined by $\sqrt{k^2+l^2}$. The components of group velocity for a stationary Rossby wave ($\omega = 0$) may then be represented as $c_{gx} = \frac{dx}{dt} = \bar{u}_\psi + \frac{(k^2-l^2)\bar{\zeta}_y}{K^4}$ and $c_{gy} = \frac{dy}{dt} = \frac{(2kl)\bar{\zeta}_y}{K^4}$. In this study, these group velocities are used to determine Rossby wave paths, as in *Karoly* (1983). By using analogies to optical physics, *Hoskins and Ambrizzi* (1993) demonstrated that the subtropical jet characterized by high stationary wavenumber acts as a waveguide, which can trap Rossby waves and affect their propagation direction. We will demonstrate below that the interannual variability of the subtropical jet plays a vital role in determining the pattern consistency of MJO teleconnections from event to event.

4.3 THE CONSISTENCY OF TELECONNECTIONS IN REANALYSIS

Figure 4.2 demonstrates the pattern consistency of the daily and intraseasonal Z500 anomalies over different ENSO states as a function of MJO phases and time lag. Darker colors indicate that more paired events have similar teleconnection patterns, while lighter colors indicate fewer paired events have similar teleconnection patterns. An n-day lag indicates n days after the given MJO phase. Figure 4.2(a)-4.2(d) show the unfiltered anomalous Z500 and 4.2(e)-4.2(h) display the intraseasonal Z500 anomalies. In Figure 4.2(a) during ENSO neutral conditions, two striped patterns extend from lag 0, MJO phase 3 and phase 8 to lag 20, MJO phase 1 and phase 5, respectively. This feature is consistent with *Tseng et al.* (2019) (chapter 3), who demonstrated that the two stripes of high pattern consistency are generated when MJO heating exhibits a dipole pattern with opposite heating centers on either side of the Maritime continent (e.g. MJO phase 2, 3, 6 and 7). The tilting structure of the stripes is due to the progression of MJO phases and associated eastward propagation of convection. However, with variations in ENSO state (Figure 4.2b and 4.2c), for unfiltered Z500 anomalies only one of the two stripes indicating high pattern consistency still exist in both cold and warm ENSO periods. In El Niño years, only the stripe initiated in Phase 8 exists, while the stripe initiated in Phases 3 and 4 only shows up in La Niña years.

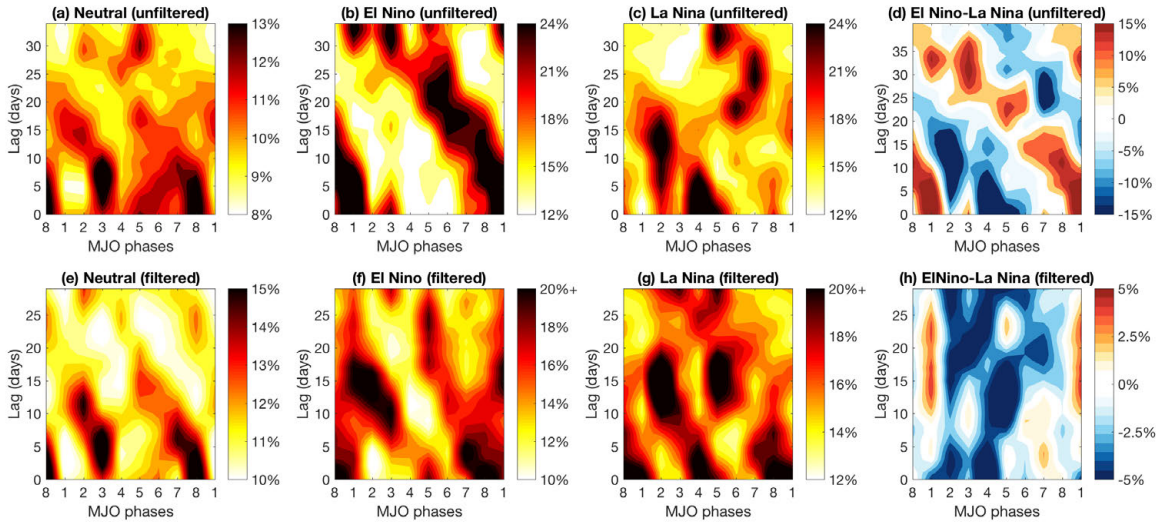

Fig. 4.2. The pattern consistency of the unfiltered (a)-(c) and intraseasonal (e)-(g) Z500 anomalies over the domain of the North Pacific and the North America (20^o-70^oN, 150^oE-120^oW) in neutral, El Niño and La Niña years, respectively. (d) is the difference between (b) and (c). (h) is the difference between (f) and (g).

It is hypothesized that constructive or destructive interference of MJO and ENSO teleconnection patterns are responsible for some of the behavior shown in the top row of Figure 4.2. The role of tropical heating in generating tropical-extratropical teleconnections has been extensively investigated since the 1980s, including that associated with both intraseasonal and interannual time scale heating. The El Niño SST warming pattern and associated active convection in the eastern and central Pacific are known to induce a positive Pacific-North America pattern (PNA pattern), which is characterized by a low-pressure anomaly in the North Pacific, high pressure anomaly near the west coast of North America, and a low-pressure anomaly in the east United States. La Niña years are associated with a negative PNA pattern. *Henderson and Maloney* (2018) demonstrated the MJO convection in phases 2 and 3 favors a negative PNA pattern while the convection in phases 6 and 7 leads to a positive PNA pattern. Since both the interannual and intraseasonal timescales Z500 anomalies are included in the unfiltered Z500 anomalies, the constructive (destructive) interference between the teleconnection patterns generated on these two timescales likely lead to enhanced (diminished) pattern consistency during certain periods in Figure 4.2(b) and 4.2(c) relative to Figure 4.2(a), consistent with the superposition of ENSO and MJO teleconnections shown by Henderson et al. (2018) (referred to their Figure 12). Figure 4.2(d) depicts the difference of the unfiltered Z500 anomaly pattern consistency between El Niño and La Niña years and a shift of the high pattern consistency from El Niño years to La Niña years is observed, which can be explained by the tropical-extratropical teleconnections directly generated by interannual convection variability. In El Niño years, the constructive interference between MJO and ENSO teleconnections happens around MJO phase 6 and 7, however, this feature shows up in MJO phase 2 and 3 during La Niña years. Thus, 4.2(d) shows the shift of regions characterized by high pattern consistency due to the change in ENSO state. The amplitude change in the pattern consistency of daily Z500 on interannual timescales can reach 15%, which is about the same order of magnitude with the pattern consistency shown in Figure 4.2(a)-4.2(c). Therefore, Figure 4.2(d) highlights the importance of the ENSO on modulating the daily Z500.

In addition to ENSO's ability to interfere with the MJO teleconnection through superposition, it can indirectly influence MJO teleconnections by modulating the basic state upon which MJO teleconnections propagate and develop, as well as the strength and propagation characteristics of MJO convection. To remove the direct influence of ENSO on the extratropical geopotential height, an intraseasonal band-pass filter (20-100 days) is applied. The resulting patterns consistencies are shown in Figure 4.2(e)-4.2(g). Both Figures 4.2(a) and 4.2(e) show similar stripe features, except that the stripes are more distinct in Figure 4.2(e). Since Figure 4.2(a) contains Z500 variability on timescales shorter than subseasonal, it logical that

the stripes of pattern consistency will be more clear in Figure 4.2(e) than 4.2(a). The other apparent difference is that two stripes show up in both Figure 4.2(f) and 4.2(g) during both warm and cold ENSO states compared to a single stripe in 4.2(c) and 4.2(d). This change supports the previous hypothesis that the diminished pattern consistency in regions of phase space in Figure 4.2(b) and 4.2(c) is caused by the destructive interference between interannual and intraseasonal teleconnections. Lastly, we compare the difference in MJO teleconnection pattern consistency between El Niño years and La Niña years (Figure 4.2h). Figure 4.2(h) suggests a systematic increase of pattern consistency from El Niño years to La Niña. A number of factors may explain this increased pattern consistency including changes in MJO intensity, propagation speed of MJO convection, the eastward longitudes to which MJO convection penetrates (eastward extension or westward retraction), and the strength and location of the subtropical jet. The coexistence of different factors makes the key mechanisms difficult to assess in reanalysis fields. The difference in sample sizes over different climate states, such as neutral years having twice the sample size of the other two ENSO states, also increases the difficulty of interpreting the robustness of the results. Therefore, we use an LBM in the next section to help address these challenges.

4.4 THE CONSISTENCY OF SIMULATED TELECONNECTIONS

In this section, we address the following two questions (1) Can an LBM simulate the interannual variability of MJO teleconnection pattern consistency found in the reanalysis data? and (2) What is the key mechanism that determinines the interannual variability of the teleconnection pattern consistency?

4.4.1 An overview of the simulated MJO teleconnection pattern consistency

Seven ensemble simulations are generated by varying the basic states and/or the MJO forcing to assess the two questions posed above. As described in section 4.2, each ensemble simulation generates 30 ensemble members by perturbing the MJO forcing in each MJO phase. Figure 4.3 demonstrates the pattern consistency of the simulated MJO teleconnections in the LBM as a function of MJO phase and time lag. Figure 4.3(a) shows the pattern consistency of the MJO teleconnections when both the basic states and the MJO forcing are acquired from ENSO neutral years. The second row shows the pattern consistency of the MJO teleconnections when the basic states and/or the MJO forcing are replaced by El Niño year conditions. The third row is the pattern consistency of the MJO teleconnection when the basic states and/or the MJO forcing are replaced by La Niña year conditions. As discussed in Tseng et al. (2019) (chapter 3), the simulated pattern consistency is on average higher than the reanalysis pattern consistency, which, in-part, reflects

the absence of noise by the synoptic eddies in the idealized linear model compared to the real world. Regardless of the systematic bias in amplitude, the LBM can qualitatively simulate the interannual variability of MJO teleconnection pattern consistency in reanalysis, especially the decreased consistency of the MJO teleconnection pattern in El Niño years compared to La Niña years (compare Figure 4.3d and 4.3g to Figure 4.2h). Both the El Niño basic states (Figure 4.3b) and the El Niño MJO forcing (Figure 4.3c) dramatically decrease the pattern consistency of the MJO teleconnections. When both are taken into account, the pattern consistency decrease can exceed 50% (Figure 4.3d). For the La Niña years (the third row of Figure 4.3), the effects from basic states and the MJO forcing compete. The La Niña year basic states increase the pattern consistency while the La Niña MJO forcing decreases the pattern consistency of MJO teleconnections compared to the neutral state. Therefore, the net influence from La Niña in the consistency of MJO teleconnections is modest (i.e. difference between Figure 4.3a and 4.3g). In the next two subsections, the role of variation in basic states and the MJO forcing over different ENSO climate states in affecting the MJO teleconnection will be examined in more detail.

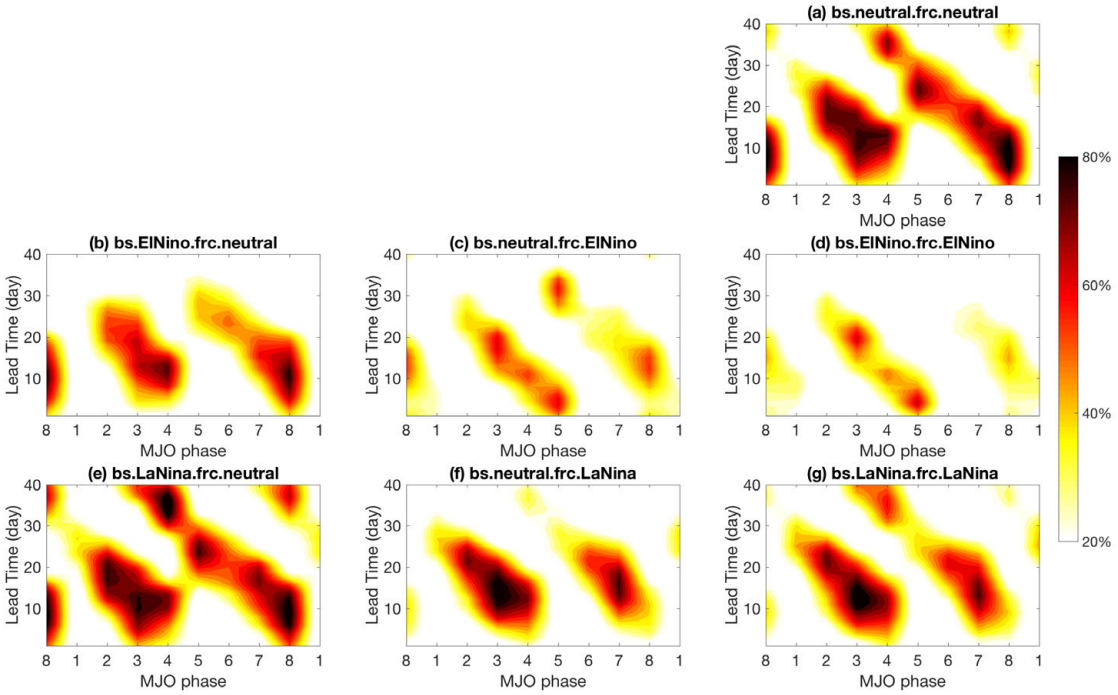

Fig. 4.3. The pattern consistency of Z500 anomalies over the 30 ensemble members in the simulations of (a)bs.neutral.frc.neutral (b)bs.El Niño.frc.neutral (c)bs.neutral.El Niño (d)bs.El Niño.frc.El Niño (e)bs.La Niña.frc.neutral (f) bs.neutral.frc.La Niña (g)bs.La Niña.frc.La Niña

4.4.2 The role of basic states

Figures 4.3(b) and 4.3(e) indicate that La Niña basic states favor a higher pattern consistency for MJO teleconnections relative to El Niño years. As a first step to address the dynamics responsible for this interannual variability of MJO pattern consistency, the linearized Rossby wave source based on equation 4.3 is examined for the three ensemble simulations: bs.neutral.frc.neutral, bs.El Niño.frc.neutral, and bs.La Niña.frc.neutral. The results are shown in Figures 4.4(a)-4.4(d). The shading in 4.4(a) is the composite MJO phase 6 Rossby wave source averaged over the 30 ensemble members from the simulation of bs.neutral.frc.neutral (lag 0-5). Phase 6 is one of the MJO phases characterized by the high pattern consistency at lag 10, although other phases with high pattern consistency give similar results. The dipole Rossby source pattern across the subtropical jet (to the east and west of the jet entrance regions) has been documented in previous studies to lead to a more consistent MJO teleconnection pattern due to the constructive interference of Rossby waves emanating from the positive and negative source regions (*Seo and Lee* (2017); *Tseng et al.* (2019)). In general, a more defined dipole structure of the Rossby wave source leads to a higher MJO teleconnection pattern consistency (Figure 2.11 in chapter 2).

The shading in Figures 4.4(b) and 4.4(c) shows the difference between the composited Rossby wave source between the simulations of bs.El Niño.frc.neutral and bs.La Niña.frc.neutral, respectively, and bs.neutral.frc.neutral. The solid contours are the boreal winter mean zonal wind at 200 hPa over different climate states, and the dashed contours represent the change in mean zonal wind during the ENSO periods relative to neutral conditions (i.e. El Niño − neutral or La Niña − neutral). The most notable variations on interannual timescales show up in the western center of the Rossby wave source dipole. Previous studies have demonstrated that the western center of Rossby wave source is mostly determined by the anomalous divergence in a region of climatological positive vorticity (i.e. $-\bar{\zeta}\nabla\cdot\mathbf{v}_{\chi}^{'}$ in equation 4.3, *Sardeshmukh and Hoskins* (1988)). During El Niño years, the western Rossby wave source center is enhanced due to increased cyclonic vorticity in the subtropical jet, with opposite behavior during La Nina years. The result of this Rossby wave source analysis contradicts what is shown in Figure 4.3 since a enhanced dipole-like Rossby wave source pattern can favor a more robust teleconnection signals rather than decreasing the pattern consistency. This implies that the concept of Rossby wave source interference cannot be used to explain the interannual variability of the MJO teleconnection pattern consistency shown in Figure 4.3(b) and Figure 4.3(f). Another possible factor for difference between Figure 4.3(b) and Figure 4.3(f) is the interannual variability of the subtropical jet in the northeast Pacific (around $180^{o}E$-$120^{o}W$) and its effect on Rossby wave propagation. During the El Niño years, the subtropical jet expands eastward and equatorward (the

red dashed contour in Figure 4.4e), while the subtropical jet in La Niña years is characterized by westward retraction and poleward shift (the red and blue dashed contours in Figure 4.4f).

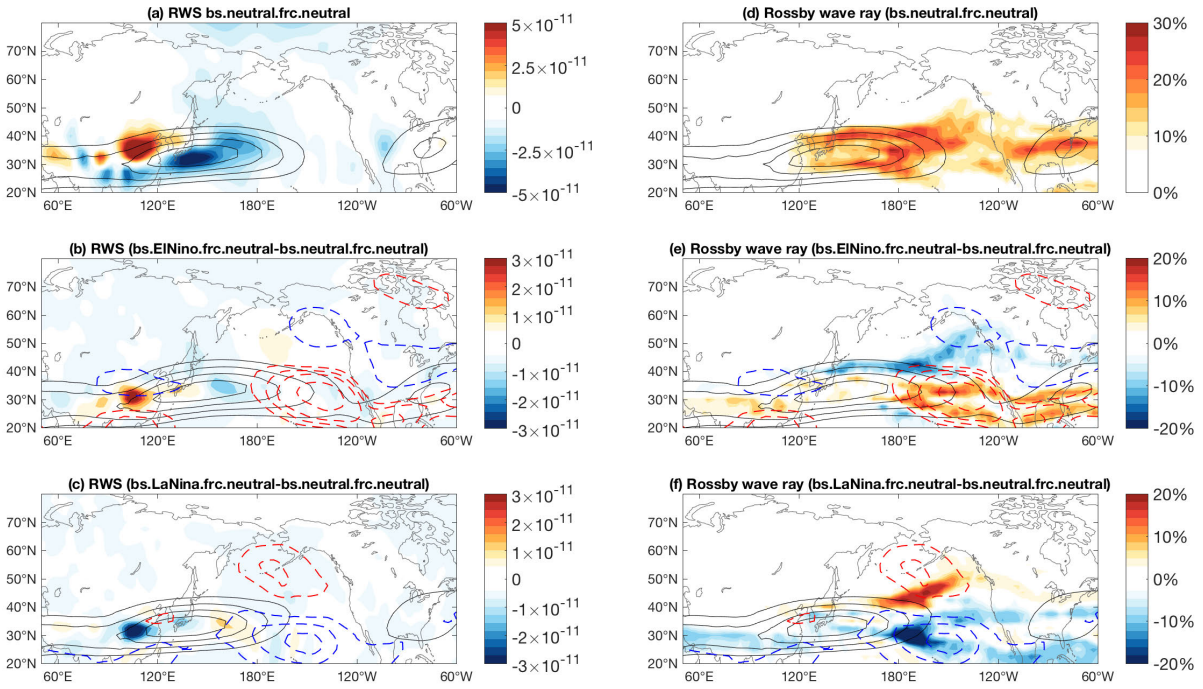

Fig. 4.4. Shading: (a) Ensemble mean MJO phase 6 Rossby wave source in the simulation of bs.neutral.frc.neutral. The difference of the ensemble mean Rossby wave source between simulations of (b) bs.El Niño.frc.neutral and bs.neutral.frc.neutral and (c) bs.La Niña.frc.neutral and bs.neutral.frc.neutral. (d) The Rossby wave ray density based on the neutral year basic states. (e) The difference of the ray density between (e) El Niño year basic states and neutral basic states and (f) La Niña year basic states and neutral basic states. The solid contours are the 200hPa zonal wind at 35, 45, 55 and 65 ms^{-1}. The dashed contours are the difference of 200hPa zonal wind between El Niño or La Nina and neutral year basic states. Red colors are positive values, starts at $4ms^{-1}$ with an interval of $4ms^{-1}$. Blue colors are negative values, starting at -$4ms^{-1}$ with an interval of $4ms^{-1}$.

To explore how the jet variations on interannual timescales influence the pattern consistency of MJO teleconnections, a wave seeding and Rossby wave tracing algorithm is applied over different climate states as described in section 4.2. Since the MJO teleconnection is quasi-stationary, we only consider $\omega = 0$ in this study, which further constrains total stationary wave number $K_s = \sqrt{\frac{\bar{\zeta}_y}{\bar{u}_\psi}}$ (equation 4.6). Rossby waves with initial zonal wave number $k = 1, 2, 3, 4$ are used, consistent with the scale of the Rossby wave source and convective scales of the MJO. Rossby waves with initial zonal wave number higher than 4 can lead to exponential growth or decay of wave amplitude because it will lead to a imaginary meridional wave number, l, due to the constrain of K_s. For each grid point with an amplitude of Rossby wave source greater than

$2 \times 10^{-11}(s^{-2})$, a Rossby wave ray is initiated and tracked for 15 days. Figure 4.4(d) shows the density of the ray paths in the simulation of bs.neutral.frc.neutral. The density indicates the number of ray paths on a grid spacing of $2.5^o \times 2.5^o$ degrees divided by the total number of ray paths. The regions with the highest ray path density are spatially collocated with the subtropical jet, consistent with a the trapping of the waves by the jet. A notable northward extension of ray paths is found at the jet exit. Figure 4.4(e) and 4(f) depict the density change in the ray paths over different ENSO states. In El Niño years, the eastward extension of the subtropical jet leads to an eastward shift of the ray paths and decreased ray density in the Gulf of Alaska. In contrast, the northward shift and contraction of the subtropical jet and ray paths in La Niña years increases the ray density in the Gulf of Alaska.

To support the results in Figure 4.4, Figure 4.5 illustrates the boreal winter averaged effective beta (i.e. β^* or $\bar{\zeta}_y$ in equation 4.5) and the total stationary wave number in the two ENSO states. Effective beta is defined as $\bar{\zeta}_y = \beta - \frac{\partial^2 \bar{U}}{\partial y^2}$, where β is the meridional gradient of the planetary vorticity and $\frac{\partial^2 \bar{U}}{\partial y^2}$ is constructed from the basic state zonal wind. β^* represents the restoring force of Rossby waves, and wave propagation is only possible in regions with positive β^*. Figure 4.5(a) and 4.5(b) show that regions with positive and large β^* are spatially collocated with the jet. Regions of high maximum β^* are more continuous across the Pacific and North America during El Niño years than La Niña years. The basic state zonal wind and β^* can be used to defined a total stationary wavenumber ($K_s = \sqrt{\frac{\bar{\zeta}_y}{\bar{u}_\psi}}$), which is shown in 4.5(c) and 4.5(d). Based on Snell's law in optics, *Hoskins and Ambrizzi* (1993) demonstrated that stationary Rossby waves are refracted toward regions with large stationary wave number, consistent with the wave guide effect described above. In El Niño years, the wave guide (e.g. regions with high K_s) spans from the Pacific to Atlantic (i.e. $K_s = 4$ contours), which makes Rossby waves less likely to propagate northward, especially for high zonal wave numbers. Thus, the ray density in the Gulf of Alaska is decreased in El Niño years (Figure 4.4e). However, the northward shift of the wave guide in La Niña years indicates that shorter waves (i.e. k=3,4) have expanded influence in extratropical regions, consistent with increases in ray density around British Columbia and the Gulf of Alaska (Figure 4.4f).

Northward propagating Rossby waves near the exit regions of the subtropical jet plays an important role in generating the PNA pattern. Decreased production of northward propagating waves in El Niño years implies a decreased modulation of extratropical geopotential height by MJO teleconnections. In contrast, an increased density of northward propagating waves in La Niña years enhances the MJO's modulation of extratropical Z500. These shifts in ray paths over different ENSO states agrees with the results on MJO teleconnection pattern consistency shown in Figures 4.3(b) and 4.3(e).

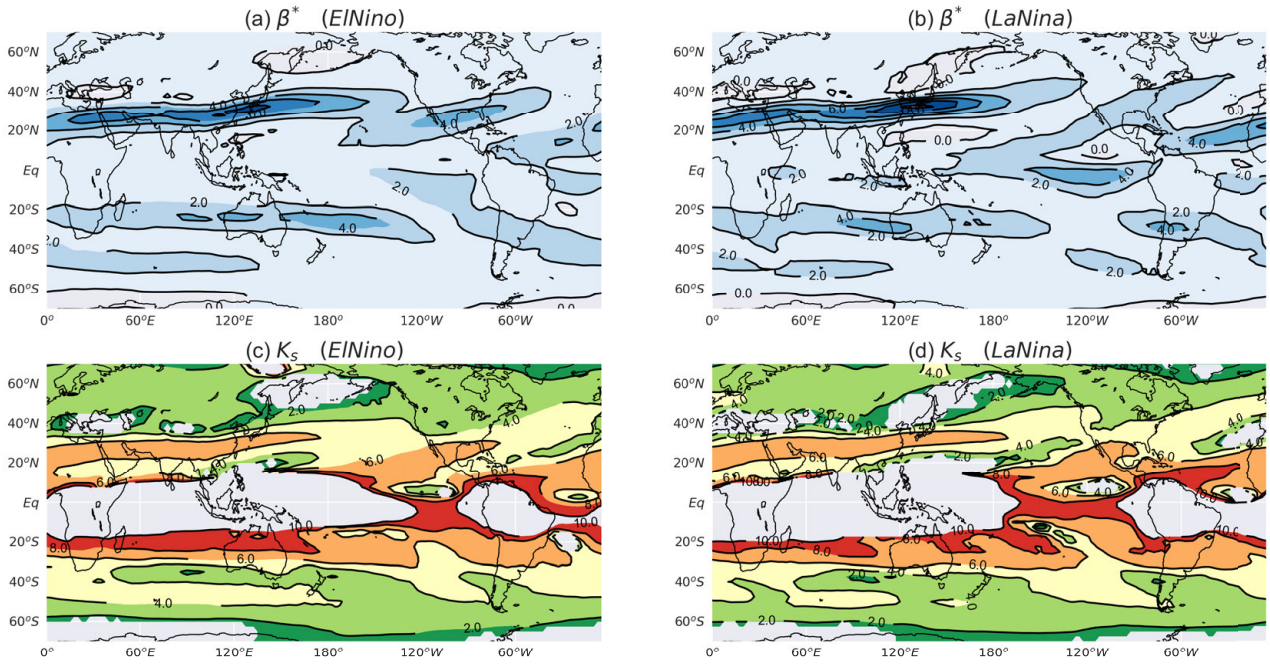

Fig. 4.5. The boreal winter averaged effective β in (a) El Niño years ($(ms)^{-1}$) and (b) La Niña years ($(ms)^{-1}$). Stationary Rossby wave number in (c) El Niño years and (d) La Niña years

4.4.3 The role of MJO forcing

This subsection focuses on the role of MJO forcing in modulating pattern consistency by analyzing three simulations : bs.neutral.frc.neutral, bs.neutral.frc.El Niño and bs.neutral.frc.La Niña. All have identical basic states, but with the MJO forcing varied across the different ENSO states. This investigation highlights how the Rossby wave source pattern is affected by variations in MJO forcing. Figure 4.6(a) shows the MJO phase 6 Rossby wave source (shading) and the 200 hPa anomalous divergent flow (vectors) averaged from lag 0 to lag 5. While only MJO phase 6 is shown, other phases producing a robust teleconnection show similar results. As discussed above, Rossby waves forced by opposite-signed Rossby wave sources on either side of the subtropical jet (i.e. dipole structure) can constructively interfere to produce consistent midlatitude geopotential patterns. Figure 4.6(a) suggests that the western center of dipole Rossby wave source is dominated by anomalous convergence in a region of high climatological vorticity ($-\bar{\zeta}\nabla\cdot\mathbf{v}_\chi'$), while the eastern center results from the negative climatological vorticity advection by the anomalous divergent flow ($-\mathbf{v}_\chi\cdot\nabla\bar{\zeta}$).

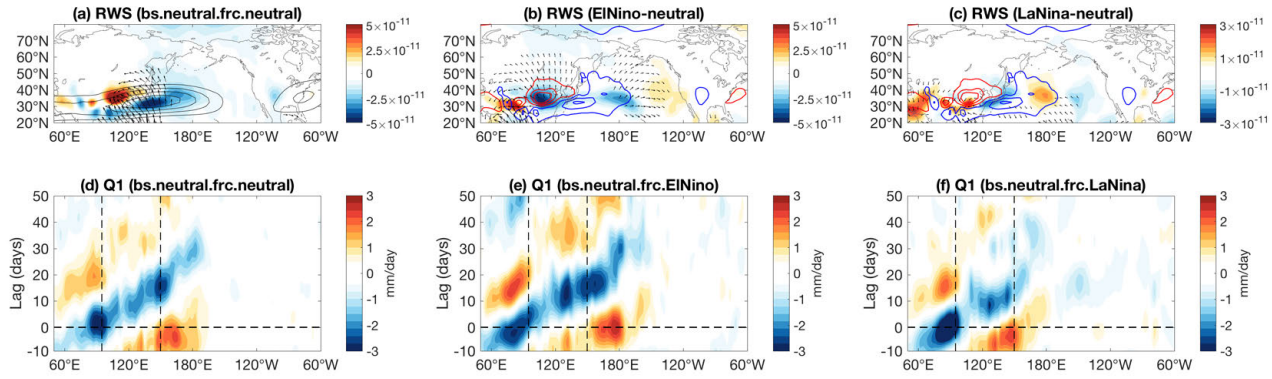

Fig. 4.6. The MJO phase 6 Rossby wave source (shading, unit=s^{-2}) and the 200hPa divergent flow (vector, unit=ms^{-1}) averaged over lag 0-lag 5 for (a) bs.neutral.frc.neutral, and the difference between (b) bs.neutral.frc.El Niño and bs.neutral.frc.neutral and (c) bs.neutral.frc.La Niño and bs.neutral.frc.neutral. The contours in (b) and (c) are identical to the shading in (a). Vector length is proportional to the real magnitude of divergent wind anomalies with magnitudes smaller than $0.2ms^{-1}$ omitted.

Figure 4.6(b) and 4.6(c) show the differences in Rossby wave source and anomalous divergent wind between the simulations of bs.neutral.frc.El Niño and bs.neutral.frc.La Niña with and bs.neutral.frc.neutral. The color contours in 4.6(b) and 4.6(c) are identical to the shading in 4.6(a) (see figure caption). Figure 4.6(d)-4.6(f) show the corresponding column-integrated Q_1 anomalies from ensemble mean provided to the three simulations. For El Niño year MJO forcing (4.6b and 4.6e), enhanced northward divergent flow occurs over the domain (i.e. vectors in 4.6b, around 30^oN-60^oN and 60^oE-150^oE), related to enhanced convection across the western and central Pacific at lag 0 (i.e. shading in 4.6e, around 180^oE). Strong northward divergent flow on the north flank of the subtropical jet leads to anomalous divergence in the western center of the dipole Rossby wave source and offsets the convergence typically there. Thus, the positive western Rossby wave source shown in 4.6(a) is greatly reduced in El Niño years. A less dipole-like Rossby wave source in El Niño years supports the less consistent MJO teleconnection in Figure 4.3(c) than 4.3(a). During La Niña, the changes in the divergent flow and the Rossby wave source relative to neutral conditions are modest (Figure 4.6c). However, enhanced southward flow is apparent in the region 60^oE-120^oE and 30^oN-40^oN, associated with stronger negative MJO heating anomalies in the eastern Indian ocean during La Nina than the neutral years. The Rossby wave source pattern in La Niña years also slightly shifts westward, which reflects the westward shift of MJO convection in La Niña years compared to neutral or El Niño years. Again, the magnitude of these changes in La Niña years is relatively small compared to that in El Niño years.

For later time lags (lag 15-20), both bs.neutral.frc.El Niño and bs.neutral.frc.La Niña show a less dipole-like Rossby wave source pattern across the subtropical jet (figure not shown). A less dipole-like pattern becomes even more apparent for bs.neutral.frc.La Niña at lags 15-20 than at earlier time lags. Figure 4.6(f) shows that eastward propagation of MJO forcing is less expansive and MJO events do not maintain strength as long in La Niña years than neutral years (lag 15-20), which may help explain why the dipole Rossby wave source becomes less clear at later lags. Thus, the pattern consistency shown at later lags (> lag 25) of Figure 4.3(f) is smaller than 4.3(a). Less continuous propagation of MJO convection can result from suppressed convective activity in the western and central Pacific caused by La Niña year SST cooling.

4.5 CONCLUSIONS AND REMARKS

The role of tropical heating in modulating the extratropical circulations has been extensively investigated since the 1980s, including on interannual and intraseasonal timescales. Since the MJO is one of the dominant modes of heating on the subseasonal timescales, it is an important source of S2S predictability. However, the MJO's ability to modulate extratropical weather varies interannually. This study explored the key mechanisms determining variability in MJO teleconnection pattern consistency over different ENSO states. By conducting ensemble simulations in a linear baroclinic model by alternately fixing or varying MJO forcing or the basic states, the impact of these factors for modulating the consistency of MJO teleconnection patterns was isolated. Results indicate that the pattern consistency of MJO teleconnections from event to event decreases dramatically in El Niño years relative to neutral conditions, while MJO teleconnections in La Niña years are characterized by only small changes. In the real world, both basic states and MJO forcing can change together and Figure 4.7 summarizes the joint influence from both factors. From the basic state perspective (contours in Figure 4.7), the southeastward extension of the subtropical jet in El Niño years decreases the likelihood of Rossby wave propagation into the Gulf of Alaska, consistent with a reduction in MJO teleconnection pattern consistency in the North Pacific and North America. By contrast, a northward shift and westward retraction of the jet in La Niña years increases the possibility of wave propagation into the extratropics, which increases the pattern consistency. From an MJO forcing perspective (shading in Figure 4.7), both El Niño year and La Niño year MJO forcing weaken the dipole Rossby wave source pattern across the subtropical jet, which reduces the constructive interference of the wave signals in midlatitudes emanating from both centers. A less dipole-like Rossby wave source pattern over both ENSO states would thus help reduce the pattern consistency of MJO teleconnections.

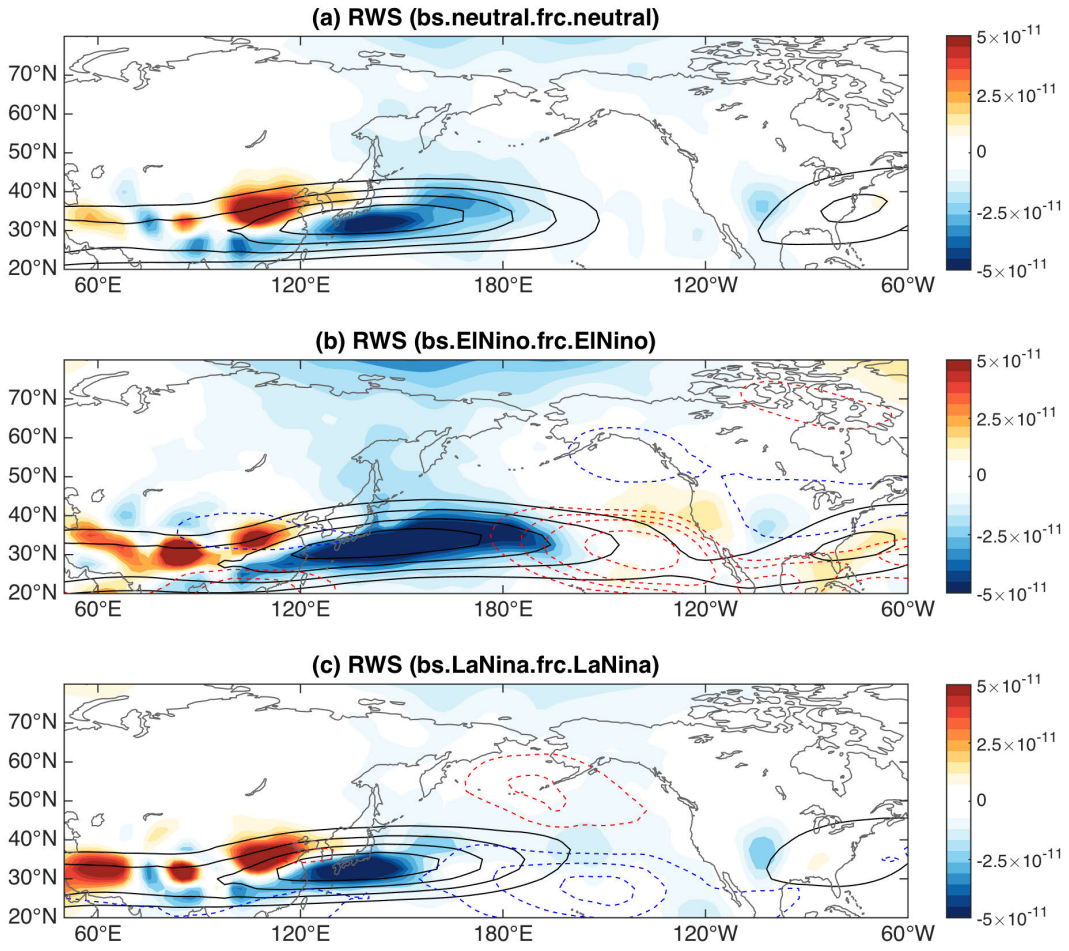

Fig. 4.7. The MJO phase 6 Rossby wave source (lag 0-5) in the simulations (a) bs.neutral.frc.neutral (b)bs.El Niño.frc.El Niño and (c)bs.La Niña.frc.La Niña. (unit=s^{-2}). Solid contours are the 200 hPa mean zonal wind at 35, 45, 55 and 65 ms^{-1} in three different climate states. The dashed contours in (b) and (c) are the difference in 200hPa mean zonal wind between the two ENSO states and the neutral years. Blue represents negative values and red positive values. The dashed contours start at 4 and -4 ms^{-1} with an interval of 4 ms^{-1}.

This study provides a compelling explanation for the interannual variability of MJO teleconnection pattern consistency. However, there are some questions remained unanswered. First, what process determines the interannual variability of MJO convective propagation? Although previous studies have showed that MJO convection propagates slower in La Niña than the El Niño years, the mechanisms responsible for a more successive MJO life cycle in El Niño years have not been examined. Second, in this study linear Rossby wave theory is used for approximating wave solutions, which assumes the basic state varies slowly

in space and time. However, wave-mean flow interactions between MJO teleconnections and the subtropical jet can alter the on daily timescales. How such feedback processes influence the robustness of MJO teleconnections is still unclear. Third, climate model projections indicate an El Niño-like warming pattern may develop in a future climate forced by increasing greenhouse gas concentrations. How the change in basic states due to the anthropogenic warming influences the predictability of the extratropical weather is an ongoing interest.

CHAPTER 5

The importance of past MJO activity in determining the future state of the midlatitude circulation

[4]

The Madden Julian oscillation (MJO) is one of the most important sources of predictability on subseasonal to seasonal (S2S) timescales. Many previous studies have explored the impact of the present state of the MJO on the future evolution and predictability of extratropical weather patterns. What is still unclear, however, is the importance of the accumulated influence of past MJO activity on these results. In this study, the importance of past MJO activity in determining the future state of extratropical circulations is examined by using a linear baroclinic model (LBM) and one of the simplest machine learning algorithms: logistic regression. By increasing the complexity of the logistic regression model with additional information about the past activity of the MJO, it is demonstrated that the past 15 days plays a dominant role in determining the state of MJO teleconnections more than 15 days into the future. This conclusion is supported by numerical LBM simulations. It is further shown that the past 15 days of additional information are only important for some MJO phases/lead times and not others, and the physical basis for this result is explored.

5.1 INTRODUCTION AND MOTIVATION

In the past decade, multiple studies have leveraged the MJO for S2S prediction by developing empirical models based on the geographical location and the amplitude of MJO forcing (i.e. MJO indices, *Cassou* (2004); *Baggett et al.* (2018); *Mundhenk et al.* (2018)). Most of these empirical models are based on the MJO information at the time of the forecast, i.e. the MJO at lag 0. However, the MJO's influence on the atmosphere takes time to develop, especially in the extratropical regions far from the heat source(*Mori and Watanabe* 2008). By analyzing observational data and employing numerical experiments, *Mori and Watanabe* (2008) and *Tseng et al.* (2019) (chapter 3) demonstrated the extratropical Pacific-North America (PNA) pattern generated by the MJO heating takes around 10-15 days to develop, indicating that prediction of the teleconnection patterns at early forecast lead times may rely on MJO information before lag 0. We define the lag (lead) as the number of days before (after) the present state, e.g. lag -1 indicates 1 day before the current state (day 0). In addition, the teleconnections generated by past MJO forcing can interfere the teleconnections generated by later MJO forcing due to the memory of atmosphere (*Tseng et al.* 2019)

[4]This chapter contains material that will be submitted in the *Journal of Climate* as: Tseng, K-C., E. Barnes, and E. Maloney, 2019: The importance of past MJO activity in determining the future state of the midlatitude circulation

(chapter 3). For example, previous studies have shown that particular MJO phases (i.e. phases 2, 3, 6 and 7) favor a more robust PNA-like pattern while the teleconnection patterns generated by the other phases are less consistent from one event to the other. Thus, the superimposition of different teleconnection signals from MJO forcing at different time lags likely jointly help determine the extratropical circulation. These two factors imply that developing empirical models based solely on the present state of the MJO (i.e. MJO at lag 0) may be improved by incorporating information about the past MJO states as well. The importance of the accumulated impacts of past MJO activity is also relevant for diagnostic studies. For example, *Cassou* (2004) demonstrated that the MJO can significantly influence the North Atlantic oscillations (NAO) with a lead time of 0-14 days. However, MJO teleconnections take time to develop over the Atlantic far from the heat source, and thus, modulation of the NAO at 0-14 days lead is likely also impacted by the past, in addition to the present, state of the MJO.

In this study, we aim to quantify the influence of past MJO activity on the future state of the extratropical circulation. To do this, we focus on three sub questions: (1) Can an empirical logistic regression model be improved by including information about the MJO before lag 0? (2) At what point in the past does the additional information about the MJO no longer benefit the empirical model? (3) What physical mechanisms determine this additional lag? By training one of the simplest machine learning algorithms, a logistic regression model, we will demonstrate that MJO activity before lag 0 plays a critical role in determining future midlatitude geopotential height anomalies. In addition, we employ numerical experiments in a linear baroclinic model (i.e. LBM) and use the dynamics of MJO teleconnection to support and interpret these results.

The manuscript is organized as follows. Section 5.2 provides detailed descriptions of the data, methods and logistic regression model. In section 5.3, the results of predicting daily geopotential height anomalies with the logistic regression models are demonstrated using an MJO index as a predictor. We also demonstrate that different phases require different amount of additional MJO information before lag 0 for improving model prediction skills. In section 5.4, results of the logistic regression model are compared to those from the LBM simulations. In section 5.5, a physical explanation for the phase dependence of results shown in the end of section 5.3 is provided. Section 5.6 is discussion and conclusions.

5.2 DATA AND METHOD

5.2.1 Data

Thirty-seven years (1979-2015) of daily 500hPa geopotential height (Z500) data are acquired from the European Centre for Medium-Range Forecast (ECMWF) third generation reanalysis product (ERA-Interim,*Dee at al.* (2011)). Since MJO teleconnections are largely characterized by a barotropic structure, the choice of 500 hPa does not qualitatively change the results shown in this study. To derive the anomalous daily Z500, the first three harmonics of the daily climatology and the linear trend are removed. Thus, except for the seasonal cycle, the Z500 anomalies contain the variability spanning daily to interannual timescales. The Z500 field is additionally interpolated onto a $2.5^o \times 2.5^o$ grid for ease of comparison with the linear baroclinic model results.

The outgoing longwave radiation (OLR) MJO index (OMI) acquired from https://www.esrl.noaa.gov/psd/mjo/mjoindex is used as a proxy for MJO convection. The OMI1 and OMI2 indices correspond to the two principal components of the first two leading modes of the equatorial-averaged OLR. To define the MJO phase, the MJO phase angle is defined as $tan^{-1}(-\frac{OMI1}{OMI2})$. This angle is then used to approximate the location of MJO convection. Detailed description of the MJO index can be found in *Kiladis et al.* (2014). Since MJO-induced midlatitude Z500 anomalies are stronger during the boreal winter than the boreal summer, we focus this study on winter days from November to March. An MJO event is defined as when the OMI amplitude is greater than 1 standard deviation (i.e. $\sqrt{OMI1^2 + OMI2^2} > \sigma$).

5.2.2 Logistic Regression Model

We aim to quantify the influence of additional lags from past MJO activity on the future state of the extratropical circulation. To do this, we begin by investigating whether an empirical logistic regression model be improved by including information about the MJO before lag 0. By adding additional prior (before lag 0) MJO information to the input variables, we can examine if the MJO teleconnection prediction skill is improved, and can quantify the time lags at which when these additional predictors no longer provide benefit. The logistic regression model - one of the most basic forms of an artificial neural networks - has been widely used for classification problems, i.e. "yes/no" predictions (*Wilks* 2011; *Slade and Maloney* 2013). The formulation is nearly identical to a linear regression model, except that a nonlinear activation function is applied to the output of the linear regression. The purpose of this activation function is to add non-linearity to the otherwise linear model.

In this study, we convert the daily Z500 anomaly into a logistic value by mapping each anomaly to its sign. That is, $sign(Z500) = 1$ when $Z500 \geq 0$ and $sign(Z500) = 0$ when $Z500 < 0$. Equations 5.1 and 5.2 define the logistic regression model which uses OMI1 and OMI2 at lag 0 as predictors to predict the $sign(Z500)$ τ days into the future.

$$h_{i,\tau} = w_{OMI1_0,\tau} \times OMI1_{i,0} + w_{OMI2_0,\tau} \times OMI2_{i,0} + b_\tau \tag{5.1}$$

$$sign(Z500)^{predict}_{i,\tau} = \frac{1}{1 + e^{-h_{i,\tau}}} \tag{5.2}$$

Equation 5.1 is the linear part of the logistic model. $OMI1_{i,0}$ and $OMI2_{i,0}$ refer to the OMI indices of the ith MJO event at lag 0, $w_{OMI1_0,\tau}$ and $w_{OMI2_0,\tau}$ are the corresponding coefficients, b_τ is the "bias unit", which is a constant and $h_{i,\tau}$ is the predictive value of the linear regression model. In this study, the forecast leadtime τ spans from 0 to 30 days. Equation 5.2 is the sigmoid activation function which converts the output of Equation 5.1 into logistic values. Thus, plugging $h_{i,\tau}$ into this activation function provides a final prediction of the sign of the Z500 anomaly $sign(Z500)^{predict}_{i,\tau}$. For each grid point and forecast lead time, we develop a unique logistic model. In this way, the models over different grid points do not rely on one another. In this study, we use gradient descent optimizer to determine the optimal values of coefficients (e.g. $w_{OMI1_0,\tau}$, $w_{OMI2_0,\tau}$ and b_τ). Detailed information is given in appendix A1.

5.2.3 Linear Baroclinic Model

To augment the results from the logistic regression model, we additionally conduct numerical experiments with a linear baroclinic model (LBM,*Watanabe and Kimoto* (2000)). Specifically, we compare five simulations, with each of the five simulations forced with the composite heating variability from the same MJO events but initialized at different time lags (i.e. $lag = 0, -5, -10, -15, -20$). This experimental setup allows us to examine how past values of MJO forcing (before lag 0) impact the generation of particular extratropical teleconnection patterns. These results are then compared to the results based on the logistic regression model. Additional details are provided in section 5.4.

5.2.3.1 Model Description

In the LBM, the primitive equations are linearized about a given basic state and the anomalous response of the circulation is calculated based on the prescribed forcing. Similar to *Tseng et al.* (2019) (chapter 3), the model is run at T42 horizontal resolution ($\sim 2.8^o \times 2.8^o$) with 20 sigma levels and utilizes fourth-order biharmonics numerical damping (including the Rayleigh friction and Newtonian damping). The e-folding

timescale for the numerical damping is 20 days for all vertical layers except the top and bottom layers which have an e-folding timescale of 0.5 days. All of these parameters are fixed throughout this study, ensuring that any differences between simulations is caused by differences in the prescribed forcing.

5.2.3.2 Model Basic States and Forcing

The LBM takes two inputs: (1) the basic state, which is associated with the linear operators in the model and (2) the anomalous forcing, which is used to drive the anomalous circulation in the model. For the basic state, five variables acquired from ERA-Interim are used: surface pressure, specific humidity, horizontal momentum (both zonal and meridional) and temperature. These variables are averaged over the boreal winter (November - March) from 1979-2015 and remained fixed throughout this study.

For the anomalous heating, the daily apparent heat source is calculated based on *Yanai et al.* (1973). The apparent heat source is defined by the budget residual of the thermodynamics equation (equation 5.3).

$$Q_1 \equiv \frac{D\,s}{D\,t} \cong Q_R + Q_c - \frac{\partial \overline{s'\omega'}}{\partial\, p} \tag{5.3}$$

In equation 5.3, s is the dry static energy, which is defined as $c_p T + g\,z$ where c_p is the specific heat, T is the temperature, g is the gravitational acceleration and z is the geopotential height. Q_R and Q_c are the energy fluxes by the radiation (both longwave and shortwave) and the latent heat. $-\frac{\partial \overline{s'\omega'}}{\partial\, p}$ is the flux convergence of dry static energy by the subgrid scale processes (e.g. cumulus convection and boundary layer turbulence). In this study, the anomalous field of Q_1 is derived by removing the linear warming trend and the daily climatology of the first three harmonics of annual cycle. A Lanczos band-pass filter (20-100 days) is then applied to the anomalous data to get the intraseasonal Q_1 anomaly.

5.3 PREDICTION OF MIDLATITUDE Z500 WITH LOGISTIC REGRESSION

In this section, we ask whether an empirical logistic regression model can be improved by including information about the MJO before lag 0. We then quantify the particular time lag in the past when additional information about the MJO no longer benefits the model. To test how the MJO teleconnection prediction skill changes with the increased information of past MJO indices in the logistic regression models, we rewrite equation 5.1 into a more general form (equation 5.4),

$$h_{i,\tau} = \sum_k [w_{OMI1_k,\tau} \times OMI1_{i,k} + w_{OMI2_k,\tau} \times OMI2_{i,k}] + b, \quad k \in \mathbb{Z}_0^- \tag{5.4}$$

where k is any time lag before lag 0 (i.e. non-positive integers) and τ is the forecast lead time spanning from 0 to 30 days. For example, $k = -10$ and $\tau = 10$ indicates that we are using MJO information from lag 0 to lag -10 to predict the teleconnection patterns 10 days after day 0.

Figure 5.1 demonstrates how often the logistic regression model with $k = 0$ (i.e. no past MJO information as a predictor) successfully predicts the sign of daily Z500 at various lead times. The events are divided into groups according to MJO phase (rows) and the forecast lead time (columns). Darker colors indicate higher success rates. The regions of high success rate (i.e. phase 2, 10-14 day lead time or phase 3, 5-9 day lead time) represent a PNA-like wave train extending from the North Pacific to the Gulf of Alaska. Following phase 3, the PNA-like signal initiates from the extratropical Pacific and then strengthens over the Gulf of Alaska, consistent with the propagation of the stationary Rossby wave generated by the MJO convection. Since the MJO is a circumnavigating system along the equator, with two adjacent phases typically separated by approximately 5 days, we might expect the predicted Z500 in phase 2 at 10-14 day lead time to be similar to the predicted Z500 in phase 3 at 5-9 day lead time. It is because of this that we observe similar patterns along the diagonal directions of Figure 5.1.

To investigate how increasing the MJO information before lag 0 influences the MJO teleconnection prediction skill, Figure 5.2 (upper panel) shows the loss from the logistic regression models over multiple values of k (i.e. $k = 0, -5, -10, -15, -20$) at one particular grid point ($150^o E$, $60^o N$; "X" in Figure 5.1). The loss function is defined in appendix A, which can be consider as an analog of root mean squared error used in a linear regression model. Blue shading indicates small loss, or better prediction skill, while red shading indicates high loss, or worse prediction skill. Phase/lead times with small loss extend along the diagonal direction of the panels in upper panel of Figure 5.2, and these regions are collocated with the lead times of high success rate in Figure 5.1. Looking closely at Figure 5.2, one finds that the blue shading darkens as more MJO information is added as a predictor. This is more easily seen in lower panel of Figure 5.2, which shows the difference in loss function between the logistic regression model with extra MJO information before lag 0 (i.e. various values of k) and the model only with MJO information from lag 0 (i.e. $k = 0$). MJO information from lags 0-5 does not benefit the model prediction skill very much, although the model loss is reduced by 10%-15% when information from lags 0-15 are used (e.g. Figure 5.2h and 5.2i).

One possible explanation for why lags 0-5 days offer little additional skill is that these days provide similar information to lag 0 since the MJO is a slow-varying system. In the cases where we provide information before lag -5 days (e.g. Figure 5.2g, 5.2h and 5.2i), the MJO activity in these time lags can differ significantly from that at lag 0. In this case, the logistic regression model has additional and non-repetitive

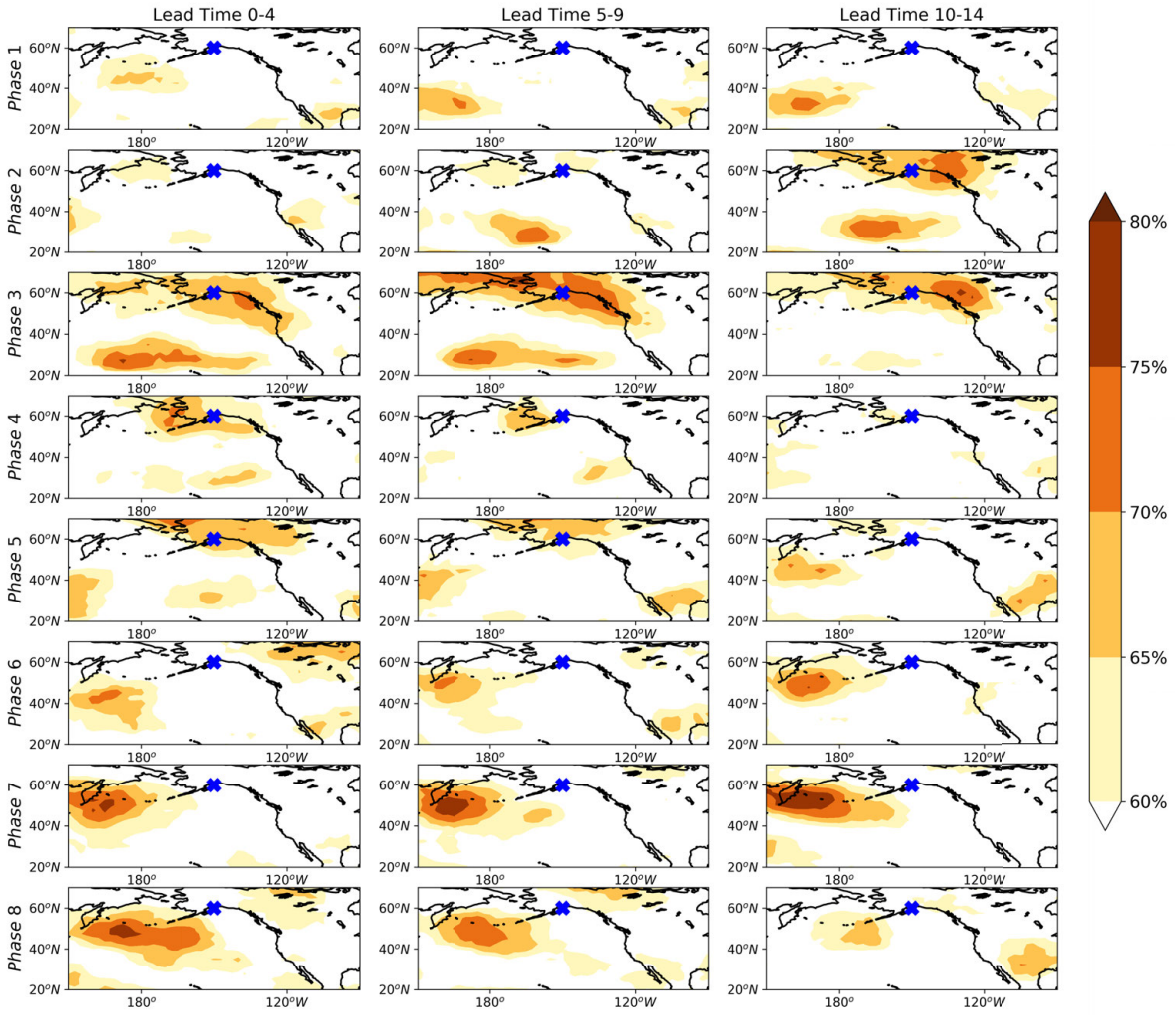

Fig. 5.1. Frequency (in percent) of correctly predicting the sign of daily Z500 anomalies by the logistic regression model for $k = 0$. Blue 'x' denotes the location shown in Fig. 5.2 and Fig. 5.3.

information that can be used for increased prediction skill. Of course, this increase in skill does not continue without limit, and comparing 5.2(h) and 5.2(i), we find that the MJO teleconnection prediction skill barely improves when extra information from lag -15 to lag -20 is included as predictors. This implies that giving the model MJO information from lag 0 to lag -15 may maximize the improvement of prediction skill, while the additional information before lag -15 has little impact on prediction. We will revisit this result with

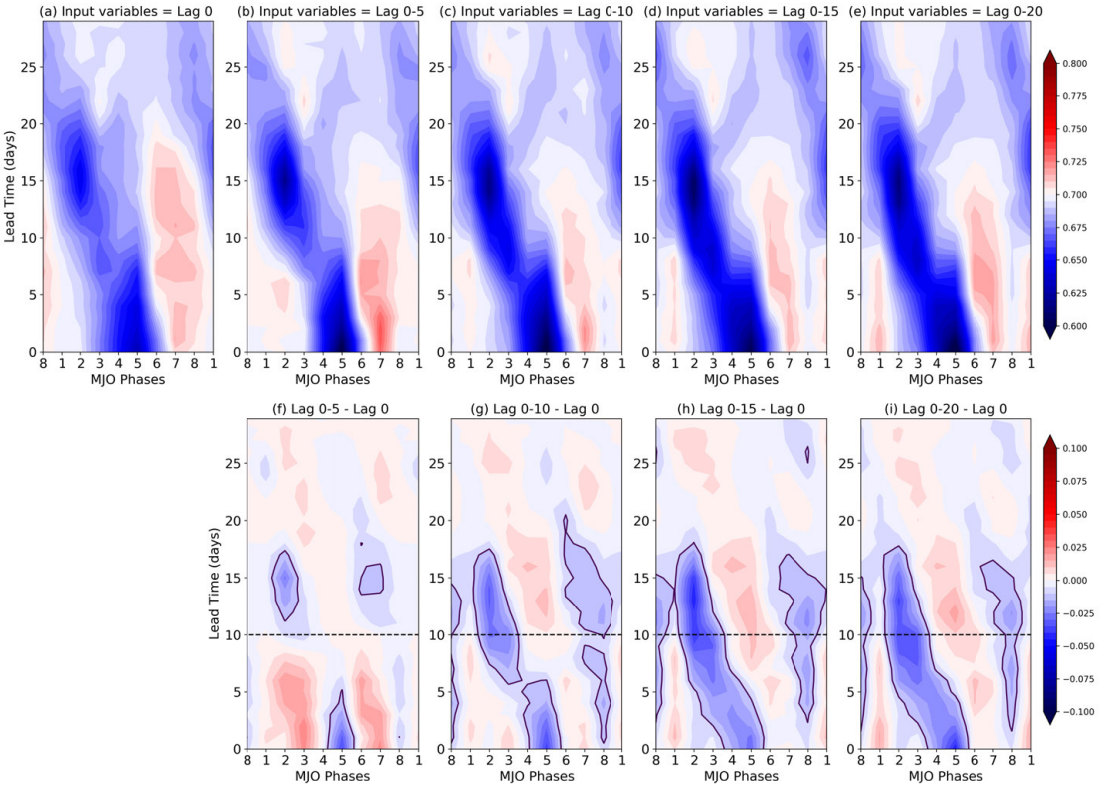

Fig. 5.2. Upper panel: The average loss (cross entropy) of the logistic regression model for (a) k=0, (b) k=−5, (c) k=−10, (d) k=−15, and (e) k=−20 as written in in equation 5.4 for the gridpoint $150^o E$ and $70^o N$ (blue 'x' in Fig. 1). Lower Panel: The difference in average loss between logistic regression models for (a) k=−5 and k=0, (b) k=−10, and k=0, (c) k=−15 and k=0, and (d) k=−20 and k=0 for the gridpoint $150^o E$ and $70^o N$ (blue 'x' in Fig. 1).

the LBM simulations in section 5.4. Finally, the lower panel of Figure 5.2 presents a perhaps surprising result that not every MJO phase/lead time is improved when additional past MJO information is added to the logistic regression model (e.g. MJO phase 5/ 10-15 forecast lead time). The mechanism responsible for this feature will be addressed in section 5.5.

To verify that the results shown in Figure 5.2 are not unique to one grid point, Figure 5.3 shows maps of the difference in loss between the model for $k = -20$ and the model for $k = 0$. Blue shading indicates that the model loss is smaller (skill is improved) when the model includes more past MJO information, while red shading indicates that the model loss is increased (skill is degraded). Comparing Figure 5.1 and Figure

5.3, regions characterized by reduced loss with additional past MJO information (blue shading in Fig 5.3) are spatially collocated with the regions that originally showed high prediction skill (shading in Figure 5.1).

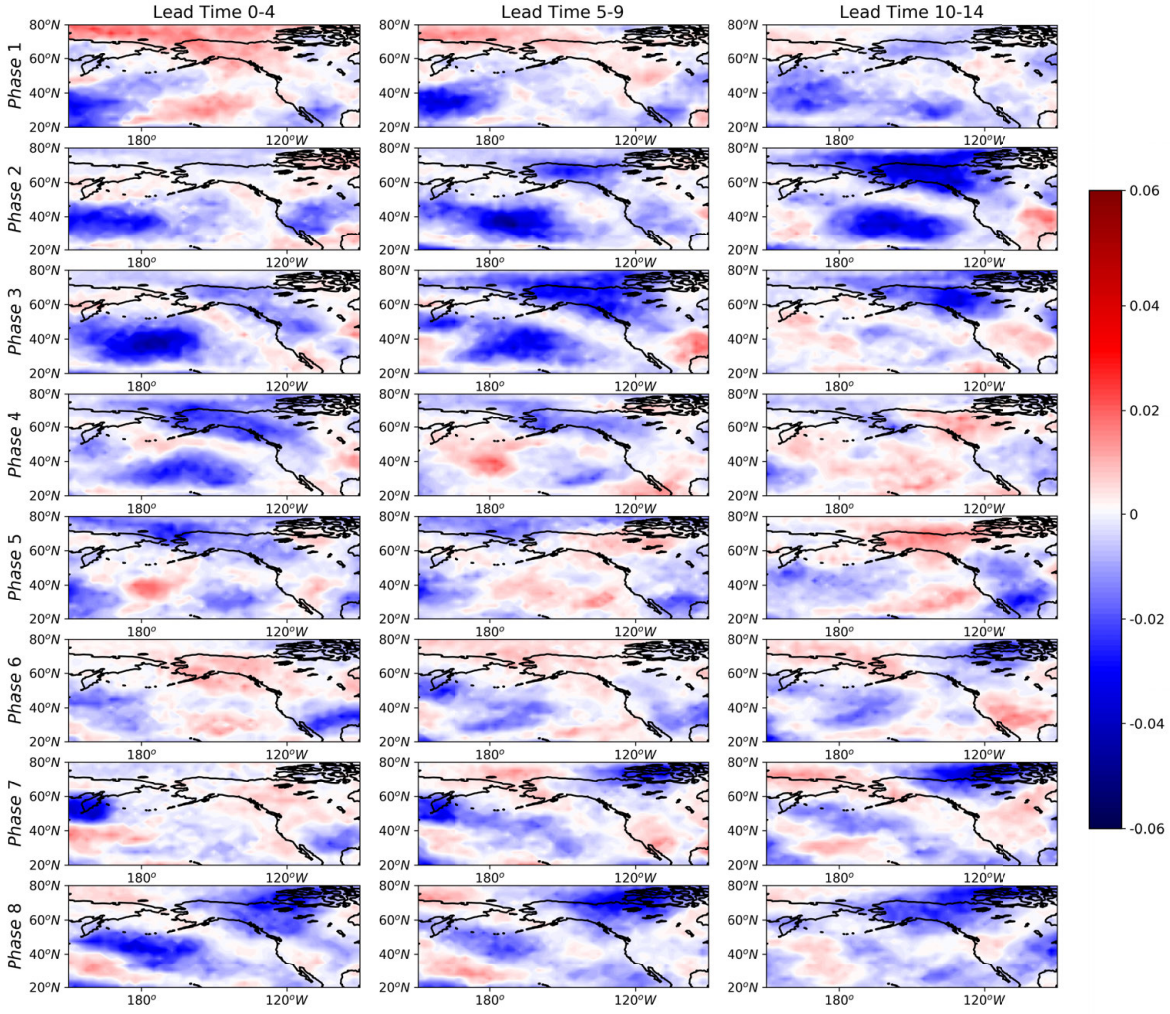

Fig. 5.3. The difference in average loss (cross entropy) between logistic regression models for k=−20 and k=0.

We also examine the difference between the logistic regression models' loss with $k = -15$ and $k = -20$ ($k = -20$-$k = -15$; shown in Figure 5.4). As previously discussed for a single grid point, MJO teleconnection prediction skill does not greatly improve with even more MJO information before lag -15 over most

of the domain. The fact that the loss slightly increases in some locations (red shading) with additional information is due to minor over-fitting of the model with additional predictors.

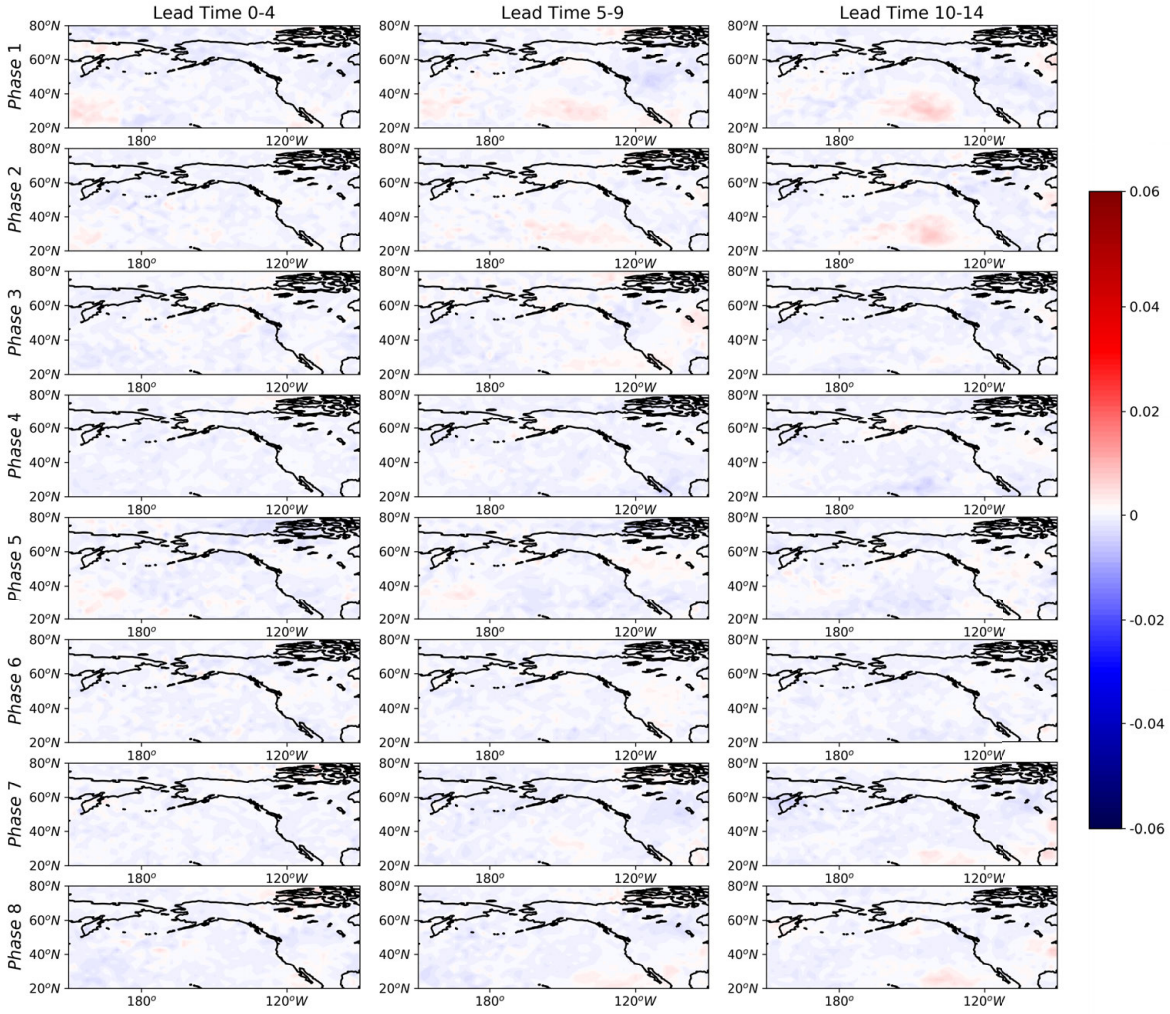

Fig. 5.4. The difference in average loss (cross entropy) between logistic regression models for k=−20 and k=−15.

5.4 MJO TELECONNECTIONS IN AN LBM

We provide additional physical inight into the results from the logistic regression model using simulations with an LBM. Specifically, we aim to quantify the importance of past MJO information in determining the evolution of the midlatitude geopotential height field.

The MJO forcing for each MJO phase is derived by randomly selecting 20 MJO events according to the criteria given in section 5.2 (i.e. the OMI amplitude at lag 0 is greater than 1σ) and calculating the phase-composited Q1 with respect to lag 0. Five simulations are run for each MJO phase, with each of the five simulations forced with the composite Q1 from the same MJO events but initialized at different time lags in the past (lag $= 0, -5, -10, -15, -20$). Figure 5.5 shows an example of this setup, where the shading represents the equatorial-average (15^oS-15^oN) MJO phase 2 forcing for the five simulations. The forcing patterns are identical from one simulation to the other after lag 0 and the forcing at lag 0 is characterized by the phase 2 heating pattern. What differs between them is the amount of MJO information before lag 0. With this simulation setup, we are able to examine the importance of past MJO activity in driving future midlatitude circulation anomalies. Finally, to increase the robustness of our results, we repeat the five simulations for each phase 24 times, giving us 24 ensemble members per simulation per phase.

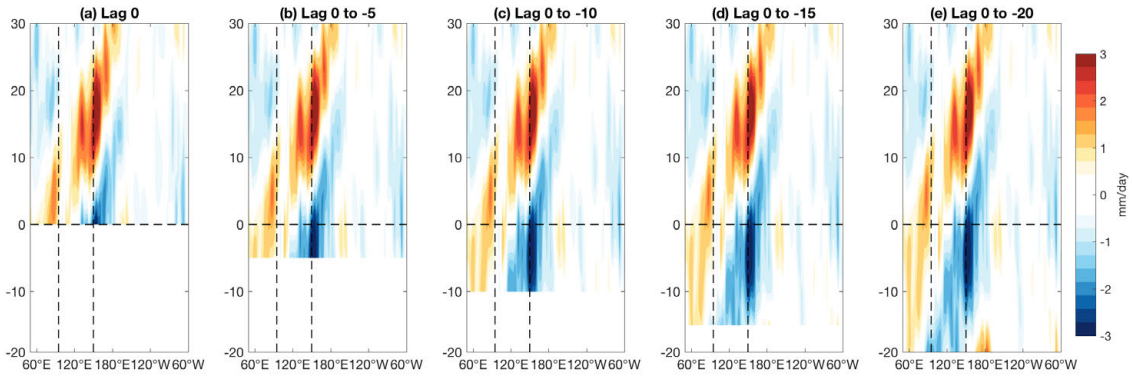

Fig. 5.5. The equatorial-average (15^oS-15^oN) MJO phase 2 column-integrated Q1 (unit=mm/day) forcing for initialization of the linear baroclinic model. Each panel denotes the forcing for each of the five different simulations. All of the simulations have identical MJO phase 2 heating at lag 0 and later lags.

The ensemble average Z500 for simulations initialized at lag 0 are shown in Figure 5.6 as a function of MJO phase and time after lag 0 (shading). We compare these anomalies with those from the simulation using information up to lag -20 days (in Figure 5.5(e); contours in Figure 5.6). Figure 5.6 shows large Z500 anomalies concentrated in specific MJO phases rather than along the diagonal directions. As noted

previously, the large signals along the diagonal of the MJO phase/lead time plots (such as Figure 5.1 and Figure 5.4) are associated with the propagation of MJO convection, where the teleconnections generated by the earlier MJO phases can interfere with the teleconnections generated by later phases. This feature is clear for the simulation which includes the MJO information from lag 0 to lag -20 (contours in Figure 5.6) but is not evident in the simulations without MJO information prior to lag 0 (shading in Figure 5.6). Further inspection of Figure 5.6 shows that differences between the shading and the contours are larger for earlier lead times (e.g. days 0-4) and smaller for later lead times (e.g. day 10-14). This can be explained by the time it takes for the MJO teleconnection to develop in the extratropical regions. That is, the MJO teleconnections in the early lead times (e.g. day 0-4) are mostly determined by the MJO forcing before lag 0 while the teleconnections in the later lead times (e.g. day 10-14) are influenced by the MJO forcing after lag 0.

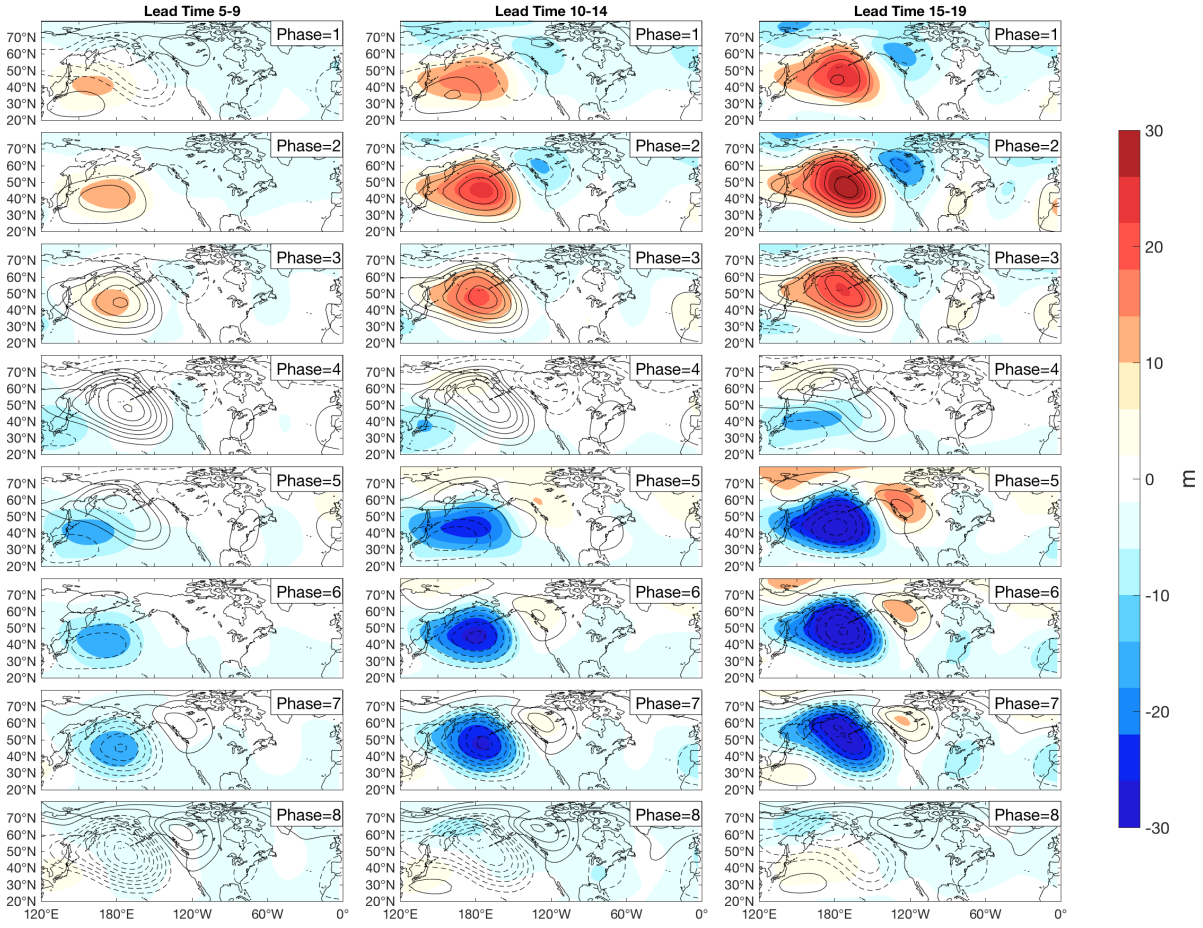

Fig. 5.6. The ensemble averaged Z500 anomalies for LBM simulations initialized at lag 0 (shading) and initialized at lag -20 (contour). Contours are drawn every 5 meters.

Figure 5.7 is identical to Figure 5.6 except the shading is the ensemble averaged Z500 anomalies from the simulation for lag 0 to -15 (Figure 5.5(d)). The similarity between the shading and contours in Figure 5.7 implies that the observed teleconnections are mostly explained by the MJO forcing from lag 0 to lag -15, while the additional information of the MJO before lag -15 has minimal impact on the simulated teleconnection patterns. This result is true whether one looks at the ensemble average, or each of the 24 ensemble members separately (not shown).

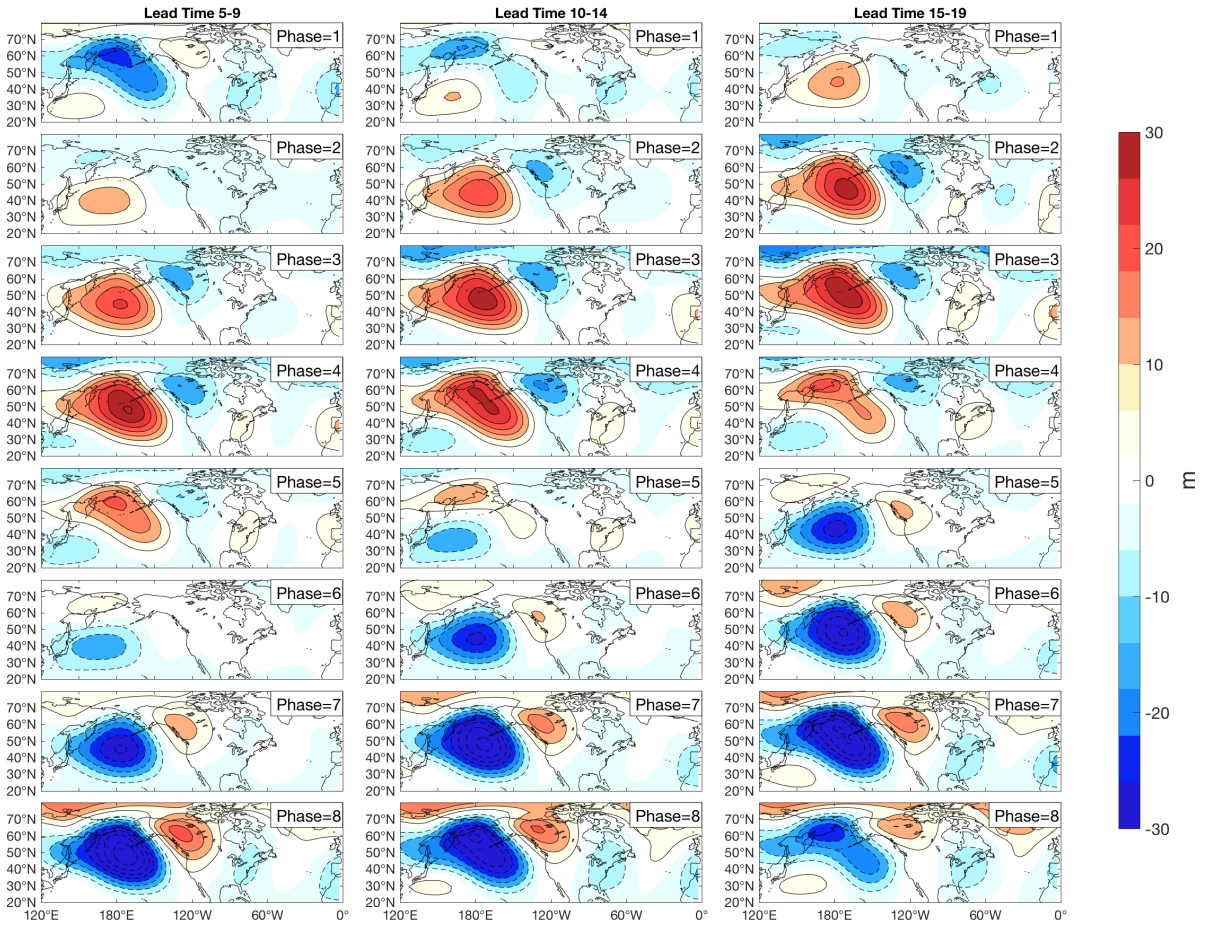

Fig. 5.7. The ensemble averaged Z500 anomalies for LBM simulations initialized at lag -15 (shading) and initialized at lag -20 (contour). Contours are drawn every 5 meters.

These results support those from the logistic regression model and indicate that 15 days is the approximate time span over which past MJO activity impacts the future evolution of the midlatitude circulation. It is worth mentioning that even though both the LBM and logistic regression models exhibit the same general

behaviour, the exact meaning of the 15 days time span is slightly different between these two models. We will expand on this point in the next section.

5.5 MECHANISTIC EXPLANATION

We now address the physical mechanisms that determine the 15 day period over which past MJO activity impacts the future evolution of the midlatitude circulation, with particular emphasis placed on why past information appears to be more important in some phases compared to others (i.e. Figure 5.3).

First, we briefly review the literature associated with the dynamics of MJO teleconnections in order to better interpret results from the logistic regression models. According to the numerical tests by *Seo and Lee* (2017) and *Tseng et al.* (2019) (chapter 3), heating in the Eastern Indian ocean and the Western Pacific can generate similar PNA-like teleconnection patterns but with opposite sign. Thus, a PNA-like pattern is more likely to be observed 10-14 days after the MJO phases characterized by dipole heating about the Maritime Continent (e.g. phases 2, 3, 6 and 7) due to constructive interference of the signals excited by the dipole heating in the two regions. On the other hand, the teleconnection patterns in other phases (e.g. phase 1, 4, 5 and 8) tend to vary more from one event to the other because of the destructive interference by the signals in these two regions. Based on these studies, one may hypothesize that a robust PNA-like signal can be found in the extratropical regions if the MJO heating persists in phases 2 and 3 (or phase 6 and 7), because of the superimposition of the same signals, while a less robust PNA-like pattern can be found if the MJO heating persists in the other phases. We will now explore how this mechanism may influence the "15 additional lags" discussed in the previous sections.

Returning to the results from the logistic regression model, we divide observed MJO events into two groups based on the change in the loss function shown in Figure 5.3(c). The first group represents the cases where the loss is greatly reduced at 10 days forecast lead time when additional MJO information (i.e. $k = -15$) is included in the model. Specifically, we choose the top one third of events most improved by the additional past MJO information. The second group represents the cases where the loss shows minimal change at 10 days lead time when the by the additional past MJO information. We choose the top one third events characterized by the least improvement in MJO teleconnection prediction skill. These two groups represent the cases where the concept of a “15 additional lags” both works (group 1) and fails (group 2).

Figure 5.8 shows the probability density function of the MJO phase over the 15 days prior to lag 0 for these two groups. The x-axis represents the MJO phase at lag 0 and the y-axis indicates the MJO phase from lag 0 to lag -15. Thus, integrating the shading along a constant x-axis results in a value of 100%. The

diagonal line represents persistent MJO forcing of the same phase over the 15 days. Shading is concentrated below this line for both groups, consistent with eastward propagation of MJO convection (where one phase is followed by the other). For example, if the MJO phase at lag 0 is phase 2, one may expect the MJO phases in the past 15 days to most likely have been phases 1, 8 or 7 rather than phases 3 or 4.

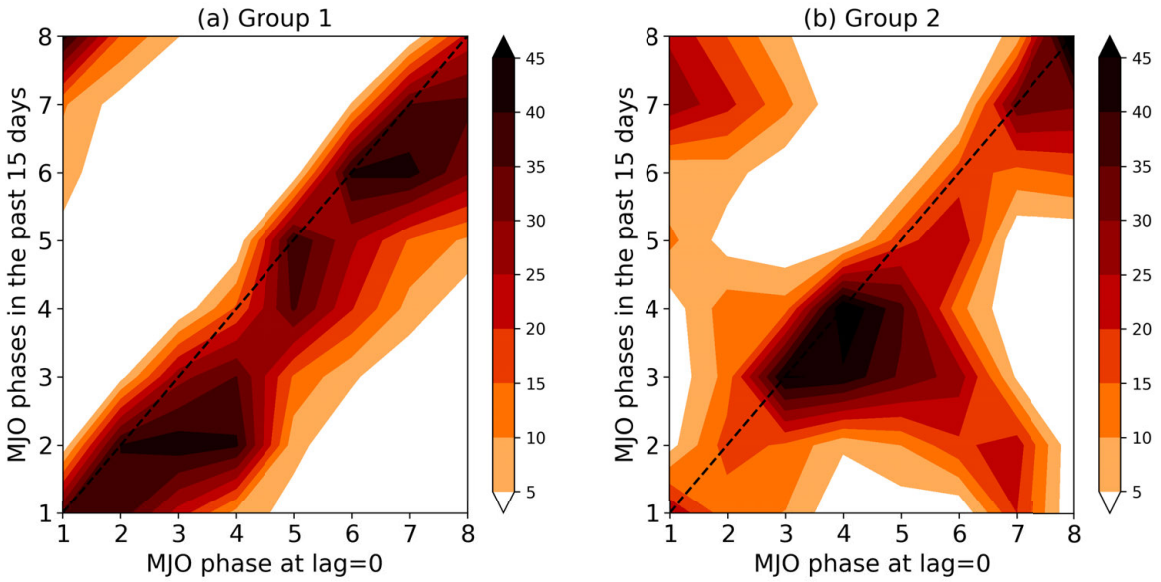

Fig. 5.8. The frequency of occurrence of the MJO phase for the 15 days before lag 0 (i.e. up to lag -15). The x-axis denotes the MJO phase at lag 0, and the y-axis denotes the MJO phase over the past 15 days. The MJO events are divided into two different groups as described in the text.

The regions of maximum frequency (shading) in Figure 5.8 imply a preference for particular past MJO phases. In group 1, the maximum frequencies appear when the MJO over the past 15 days is in phases 2, 3, 6 and 7. By contrast, the maximum frequencies for group 2 exist when the MJO over the past 15 days is in phases 4 and 8. Based on our previous discussion, phases 2, 3, 6 and 7 are characterized by more consistent teleconnection patterns, while phases 4 and 8 lack consistency. The logistic regression model is only capable of learning consistent information within the training data, and so, is only capable of using past phase information when the associated teleconnection patterns are consistent (i.e. group 1). The maximum of frequency in 5.8(a) shows the importance of past MJO phases (e.g. phase 2, 3, 6 and 7) in determining the “15 additional lags" we found for the logistic regression models. In contrast, the maximum of frequency in 5.8(b) indicates that some specific MJO phases (e.g. phase 4 and 8) don’t provide additional information for prediction.

Given this discussion, one may be confused about why the LBM does not exhibit a phase dependence in the importance of past information. That is, the LBM results suggest that the MJO activity 15 days in the past is important for the evolution of the midlatitude circulation no matter the past phase of the MJO. The reason for this is that the LBM is a deterministic model, where the future state of extratropical circulations can be considered as the linear superimposition of MJO influence over different lags. Thus, as long as the LBM is forced by Q1 from the same set of MJO events, the identical response will be simulated regardless of the current MJO phases. However, the logistic regression model based on observations is subject to the predictability of the earth system, so, only consistent relationship can be learned by the logistic regression models, such as the teleconnections generated by MJO phases 2, 3, 6 and 7. This difference explains why the phase/lead time dependence of our results only appear for the logistic regression model rather than the LBM.

5.6 CONCLUSIONS

The impacts of past MJO activity on the future state of the extratropical circulation is examined, with particular emphasis placed on quantifying how many days of past information is useful to aid prediction. Using both a logistic regression model and a linear baroclinic model to predict the evolution of midlatitude geopotential height anomalies, we demonstrate that approximately 15 days of prior MJO information importantly impacts the future evolution of the midlatitude circulation. For the logistic regression model, the prediction of MJO teleconnections is improved by including past MJO information, although this improvement is only found for specific phase/lead combinations. We find that only the MJO phases which generate consistent teleconnection patterns (i.e. phases 2,3, 6 and 7) exhibit this "15 additional lags". This is because the logistic regression model based only on two OMI indices can only learn consistent relationships in the training data.

Our results are based on results from a simple logistic regression model, and it is unclear whether the phase dependence of the results will hold for neural networks with more complex architectures. In addition, low frequency climate variability (e.g. ENSO and the quasi biennial oscillation) is known to modulate the consistency of MJO teleconnections, and thus, will likely change the specific phases/lead times for which past MJO information is useful for empirical prediction of the midlatitude circulation. How interannual variability influences how much information on past MJO activity is useful for prediction is an ongoing project. Regardless, our results suggest that midlatitude empirical prediction schemes based on the MJO may be improved by including information about the past evolution of the MJO.

CHAPTER 6

The dominant role of the MJO for extratropical variability in observations and the CMIP5 climate models [5]

It is well known that teleconnections generated by the Madden-Julian oscillation (MJO) consistently modulate weather in the extratropical Pacific and over North America, although the importance of the MJO compared to other drivers of midlatitude variability has not been thoroughly investigated. In addition, simulating the MJO continues to be a challenge for many state-of-art climate models, and it is unclear the extent to which these biases in the MJO may cause biases in midlatitude variability. In this study, we assess the impact of the MJO on extratropical variability by analyzing reanalyses and 22 climate model simulations from the Coupled Model Intercomparison Project Phase 5 (CMIP5). We find that the second leading mode of daily geopotential height in reanalysis is associated with the MJO, and can be identified without prior knowledge of the MJO, demonstrating the dominant role of the MJO in modulating extratropical circulations. This MJO-driven leading mode is also found in the CMIP5 simulations, and model biases in the wintertime extratropical geopotential height variance can be partly explained by biases in MJO simulations.

6.1 INTRODUCTION

The Madden-Julian oscillation (MJO) is a convectively coupled, planetary scale disturbance (zonal wave number 1-3) that propagates along the equator with a timescale of 20-100 days and modulates weather across the globe (*Adames and Kim* 2016; *Madden and Julian* 1971). While MJO activity impacts the tropical climate system, e.g., the initiation of the El Niño-Southern Oscillation (ENSO,*Moore and Kleeman* (1999); *Hendon and Zhang* (2007)) and tropical cyclone genesis (*Maloney and Hartmann* 2000), its influence also extends well beyond the tropics (*Hsu* 1996; *Vitart and Molteni* 2010).

Since the 1980s, the ability of large scale tropical heating, such as that associated with ENSO and the MJO, to modulate extratropical weather has been investigated through the framework of Rossby wave dynamics (*Hoskins and Karoly* 1981). The divergent flow associated with a tropical heat source can efficiently perturb the upper-troposphere vorticity field and generate a tropical-extratropical teleconnection that extends into higher latitude regions (*Sardeshmukh and Hoskins* 1988). Due to the MJO's intraseasonal timescale,

[5] This chapter contains material that will be submitted in the *Journal of Geophysical Research-Atmospheres* as: Tseng, K-C., E. Barnes, and E. Maloney, 2019: The dominant role of the MJO for extratropical variability in observations and the CMIP5 climate models

which fortuitously lands in a lead-time window with historically lower prediction skill, the MJO fills an important gap on subseasonal-to-seasonal (S2S,2-5 weeks *Vitart and Molteni* (2010); *Hamill and Kiladis* (2014)) timescales for prediction of extratropical weather and extremes (e.g. including anticyclonic blocking(*Henderson et al.* 2016), extratropical storms (*Mundhenk et al.* 2016), extreme cold air outbreaks, and heat waves (*Lin* 2018)).

Due to MJO's consistent modulation of the extratropics, the relationship between the MJO and extratropical variability has drawn a lot of attention from scientific community. For example, by comparing the Pacific-North America (PNA) pattern derived by the Empirical Orthogonal Function (EOF) and the MJO phase-composited extratropical geopotential height, *Mori and Watanabe* (2008) demonstrates that 30% of PNA amplitude variability can be explained by MJO activity. What is unclear, however, is the importance of the MJO compared to other drivers of midlatitude variability. Thus, we expand on the result of *Mori and Watanabe* (2008) in this study and examine to what extent the observed evolution of leading modes of extratropical variability (e.g. PNA) are forced by MJO heating.

Although the field has seen steady progress over the past 30 years in understanding MJO dynamics and the associated teleconnections, simulating the MJO and its teleconnections in climate models remains a challenge. A significant hurdle is properly simulating MJO convective heating, as well as the basic state upon which Rossby waves propagate. By analyzing data from Coupled Model Intercomparison Project Phase 5 (CMIP5) and the MJO task force (MJOTF)model database, both *Hung et al.* (2013) and *Jiang et al.* (2015) showed that more than half of CMIP5 and MJOTF climate models are characterized by biases in MJO heating such as insufficient propagation or too short lived convection. In addition to possible model biases in the tropics, the representation of subtropical jet has also been documented to play an important role in simulating the MJO teleconnection patterns since the subtropical jet can influence both wave propagation and generation. By analyzing 10 climate models from the CMIP5 dataset, *Henderson et al.* (2017) showed that even in models with well-represented MJO convection the bias in the mean zonal wind can still lead to poorly simulated MJO teleconnection patterns.

In this work, we focus on the impact of the MJO on midlatitude variability through tropical-extratropical teleconnections. We first show that the MJO is a dominant driver of daily midlatitude variability. We then address whether MJO biases in climate models are also reflected in the simulated midlatitude atmospheric variability. The paper is organized as follows. In section 2, the data and methods are described. In section 3, we investigate the observed connection between the leading mode of variability of extratropical geopotential height and the MJO. In section 4, biases in model-simulated geopotential height variability are linked to

biases in modeled MJO convective heating through cross spectrum analysis. We then conclude the paper in Section 5.

6.2 DATA AND METHOD

6.2.1 Reanalysis

We utilize daily data from the European Centre for Medium-Range Weather Forceats (ECMWF) third generation reanalysis product (ERA-Interim, *Dee at al.* (2011)) from 1979 to 2017 as our observational reference. The 500hPa geopotential height (Z500) is used as the diagnostic variable for tropical-extratropical teleconnections. Since tropical-extratropical teleconnections are typically characterized by a barotropic structure, the exact tropospheric level used does not substantially influence our results (not shown). Precipitation data from ERA-Interim is used to represent tropical convective activity in order to maintain a consistent data set across the precipitation and Z500 variables. Anomalous Z500 and precipitation fields are derived by removing the linear trend and the first three harmonics of the annual cycle at each grid point. Both Z500 and precipitation are interpolated to a horizontal resolution of $2.5^o \times 2.5^o$ and daily temporal resolution for comparison with the climate model fields. Unless otherwise specified, we only use data within the extended boreal winter (November-March).

6.2.2 CMIP5 dataset

A list of the 22 CMIP5 models used in this study is provided in Table 1. These 22 models exhibit varying ability to simulate MJO convection, and we exploit this in our study. We utilize the Historical simulations (specifically, years 1950-2004, *Taylor et al.* (2012)). Different models contain different ensemble sizes, and thus we only use the first ensemble member of each model to ensure equal weight across models. All model fields are interpolated to a horizontal resolution of $2.5^o \times 2.5^o$ and daily temporal resolution. Similar to the observational data, we only use the data in the extended boreal winter (November-March) since the north hemisphere teleconnection signals are stronger in the boreal winter than the boreal summer.

6.2.3 MJO indices

The Real-time MJO Multivariate (RMM) index is used as a proxy for MJO activity within the reanalysis. Typically, the RMM indices are derived by calculating the combined EOF of three equatorial-averaged (15^oS-15^oN) variables: 200 hPa zonal wind, 850 hPa zonal wind and outgoing long wave radiation (OLR). The RMM1 and RMM2 indices are then defined as the first two principal components of the first two leading

EOFs (see *Wheeler and Hendon* (2004) for details). However, since we wish to compare MJO behaviour within the CMIP5 climate models, we construct the RMM indices with slightly different atmospheric fields. Specifically, we utilize 250 hPa zonal wind, 850 hPa zonal wind and the precipitation from ERA-Interim due to a lack of daily OLR in many of the CMIP5 models. In general, model MJO activity can be defined by the first two leading modes of the combined EOFs, which is consistent with *Ahn et al.* (2017). The reason to use RMM instead of OLR-based MJO index is because some models fail to capture MJO signals without the aid of the wind component. The derived MJO index in the reanalysis is highly correlated with the original RMM indices of *Wheeler and Hendon* (2004) (i.e. ~ 0.8 for whole timeseries and > 0.95 for strong MJO events). We similarly define RMM1 and RMM2 indices across the 22 CMIP5 climate model simulations. The MJO phase is defined computing the angle using $tan^{-1}(\frac{RMM2}{RMM1})$ and mapping it to one of eight MJO phases (see *Wheeler and Hendon* (2004)), which correspond to different geographical locations of MJO convection from Eastern Indian Ocean to the Central Pacific. In this study, an MJO event is defined when $\sqrt{RMM1^2 + RMM2^2}$ is greater than 1 standard deviation.

6.3 THE CONSISTENT MODULATION OF EXTRATROPICAL CIRCULATIONS BY MJO

In this section, we examine the observed relationship between the dominant modes of extratropical variability and MJO activity. In contrast to many previous studies who base their analysis on composites or lag-regression analysis using an MJO index, we conduct a double-blind test here. Specifically, we calculate the leading modes of daily extratropical geopotential heights without cognizance of any MJO information. Furthermore, we know that the calculation of the MJO indices (RMM1 and RMM2) does not directly utilize information about the leading modes of the extratropical variability. Thus, demonstrating that the derived extratropical modes have a strong relationship to the MJO indices provides strong evidence that the MJO plays a dominant role in modulating daily extratropical variability.

Figures 6.1(a) and 6.2(a) show the two leading EOFs of daily Z500 in the domain of $150^o E - 90^o W$ and $20^o N - 80^o N$. The variance explained by the first two EOFs is significantly higher than that of the third EOF (not shown; *North et al.* (1982)). EOF1 (Fig. 6.1a) shows a dipole pattern with one center located near the Aleutians and the other center located over North America. The North Pacific center is spatially collocated with the location of the Aleutian low, where the daily Z500 has the largest variance (*Rodionov et al.* 2005). EOF2 (Fig. 6.2a) shows a typical PNA pattern with wave-train spanning from the subtropical Pacific to the Gulf of Alaska and the eastern United States.

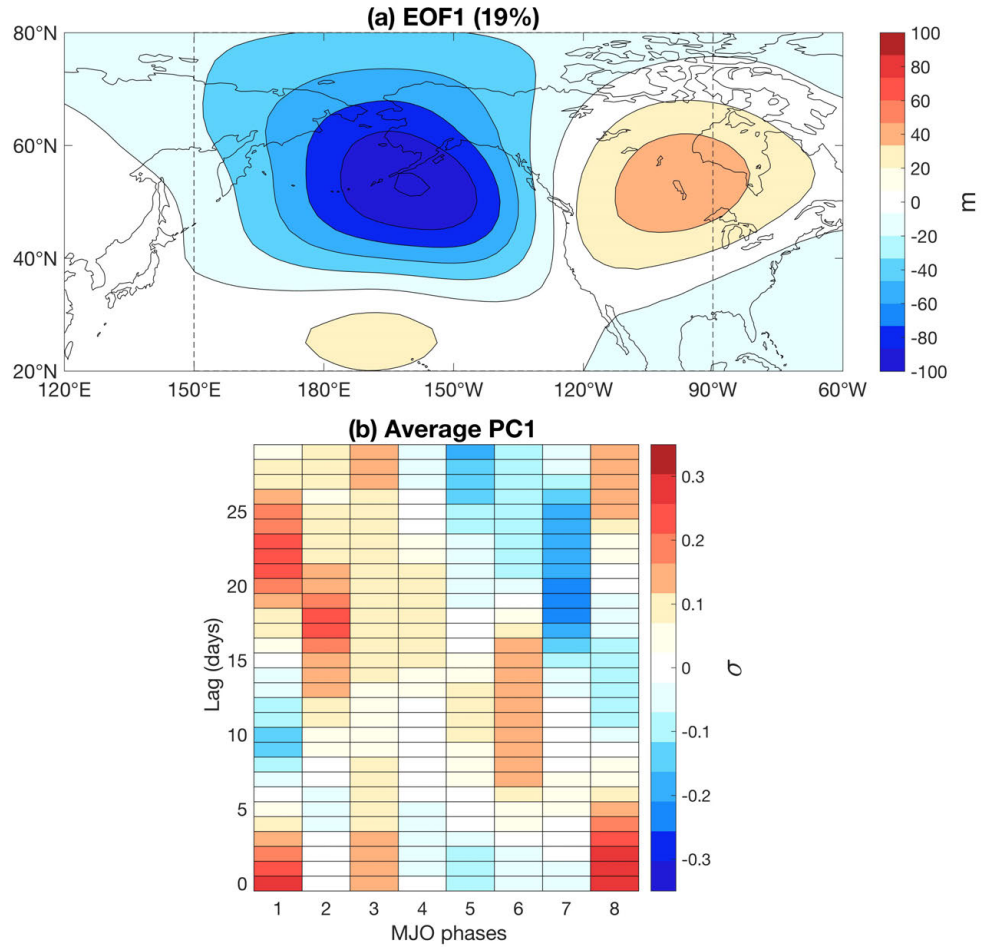

Fig. 6.1. (a) The first EOF of daily geopotential height in the domain of $150^o E - 90^o W$ and $20^o N - 80^o N$ (b) The corresponding principle component averaged over MJO phases and time lags

By projecting the daily Z500 anomalies onto EOF1 and EOF2, the corresponding daily PC time series can be derived (PC1 and PC2, respectively). The averaged PCs as a function of MJO phase and lag are shown in Figures 6.1(b) and 6.2(b), where an n-day lag indicates the average PC value n days after all MJO events of a given phase. Red colors correspond to positive average PC values while the blue colors represent negative average PC values. A significant difference between Figures 6.1(b) and 6.2(b) is found. PC1 amplitudes are relatively small for all phase/lag combinations, while PC2 shows much larger amplitudes and two clear stripes running from the upper-left to the bottom-right of hte plot. These stripes capture a coherent relationship between the MJO and midlatitude EOF2. For example, the red shading for phase 2, lag 10-15 days indicates that if the MJO is in phase 2, the likelihood of a strong EOF2 is increased approximately two weeks later. The analysis presented in Figures 6.1 and 6.2 suggest that while EOF1 is nearly independent of the MJO, EOF2 is closely related to MJO activity.

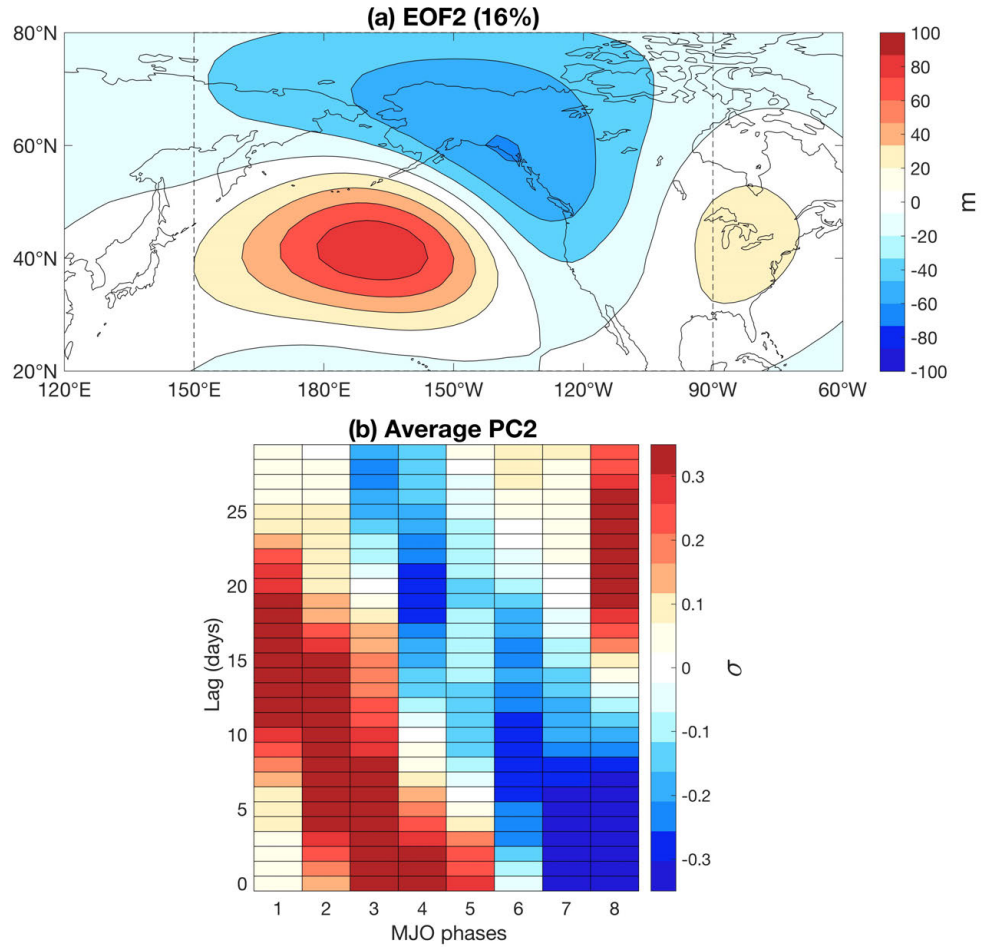

Fig. 6.2. (a) The second EOF of daily geopotential height in the domain of $150^o E - 90^o W$ and $20^o N - 80^o N$ (b) The corresponding principle component averaged over MJO phases and time lags

To further quantify the relationship between the MJO and the leading extratropical modes, we calculate the squared coherence between MJO time series and the two PCs. The result is shown in Figure 6.3. The squared coherence is a frequency-domain analog of the squared correlation coefficient, which can identify the frequencies over which two time series most strongly co-vary. Different from lag correlations, the amplitude of squared coherence is not influenced by the phase difference between the two time series. In this study, we choose 150 days as a chunk size and each chunk is centered on each winter (November-March). Thus, 37-years of data yield 37 degrees of freedom for each frequency band with a 99% confidence interval of approximately 0.11. The solid line in Figure 6.3 shows the squared coherence between the leading EOFs of extratropical geopotential height and the MJO RMM indices. The shaded regions denote the 30-90 day periods and the dashed line denotes the 99% confidence level. Only PC2 shows significant squared coherence with the MJO indices (Figure 6.3b,c) and the region with maximum squared coherence is found

on intraseasonal time scales. This result supports our earlier finding that EOF2 denotes an extratropical response to the MJO while EOF1 is independent of the MJO. It also implies the MJO's impact on extratropical variability is so large that it emerges as the second leading EOF over the region.

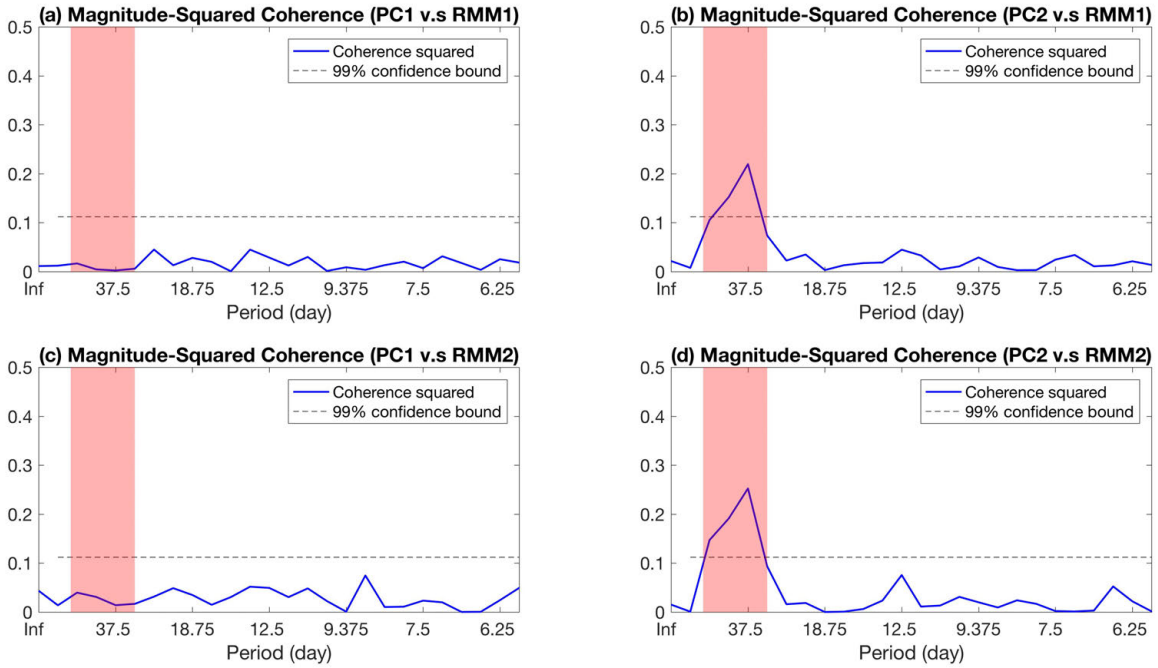

Fig. 6.3. The magnitude-squared coherence (blue solid line) between (a) RMM1 vs. PC1 (b) RMM1 vs. PC2 (c) RMM2 vs. PC1 and (d) RMM2 vs. PC2. Dashed line: 99% confidence interval. Shading: 30-90 days periods.

With these observational results in mind, we next address the extent to which these relationships are simulated across state-of-the-art climate models. Since climate models are known to have varying issues with simulating MJO, biases in the simulated MJO may be reflected in the extratropical variability if the MJO also plays a dominant role in influencing the extratropical circulations within the models. Thus, we next conduct similar analyses over 22 CMIP5 models.

6.4 MJO TELECONNECTIONS IN CMIP5 MODELS

To visualize the MJO representation within the different CMIP5 models, Figure 6.4 shows Hovmöller diagrams of the MJO phase composited precipitation anomalies averaged over the tropical band (15^oS-15^oN). ERA-Interim MJO precipitation (upper-left of Figure 6.4) around the eastern Indian Ocean ($\sim 60^oE$) strengthens in the warm pool Pacific ($\sim 120^oE$) and decays around the International Date Line ($\sim 180^oE$). In contrast, many CMIP5 models fail to capture the continuous eastward propagation of MJO convection and

exhibit a nearly stationary pattern (e.g. FGOALS-s2) or discontinuous propagation (e.g. CMCC-CESM). The feature of discontinuous propagation is especially apparent over the Maritime Continent, which is associated with the well-known "Maritime Continent Barrier" (*Zhang and Ling* 2017). To quantify the ability of each model to simulate the MJO, we define an MJO skill score for each model based on the pattern correlation between the observed Hovmöller precipitation pattern and the simulated pattern (those in Figure 6.4). This skill score has also been used in previous MJO diagnostic study (*Ahn et al.* 2017).

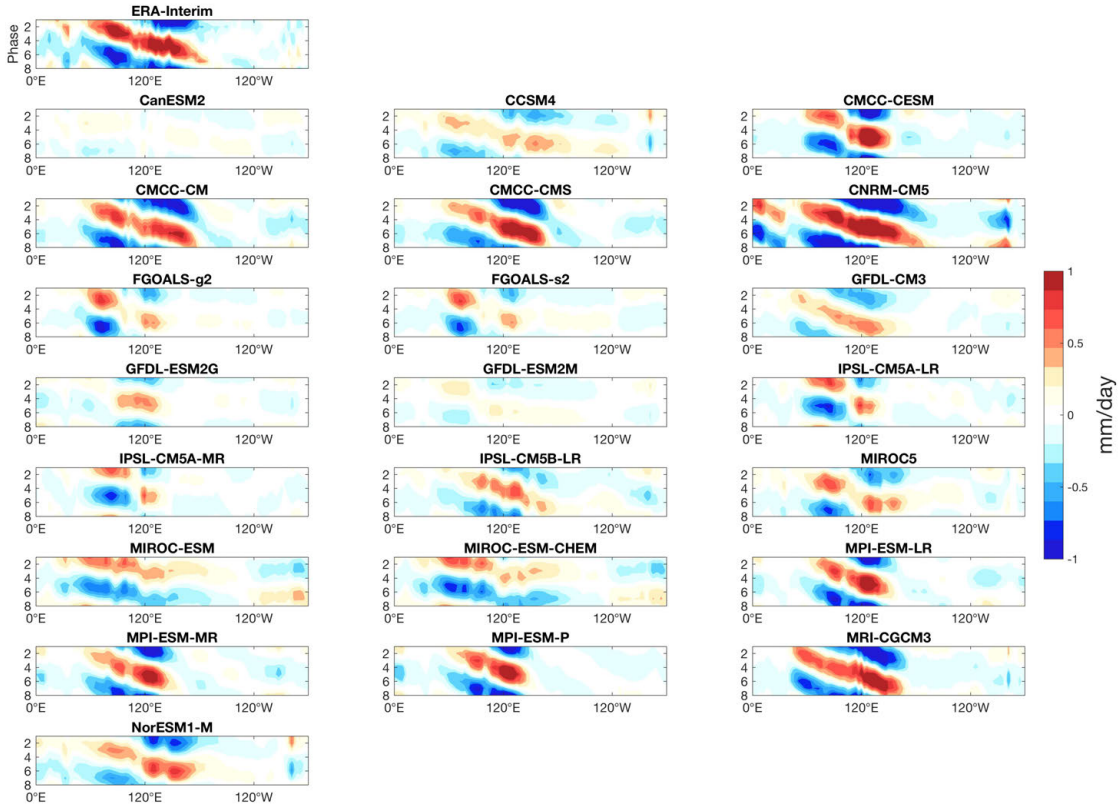

Fig. 6.4. The MJO phase composite precipitation in ERA-Interim and 45 CMIP5 simulations. Unit=mm·day^{-1}

Figure 6.5 shows each model's MJO skill score plotted against the domain-averaged ($20^o N$–$80^o N$,$150^o E$–$120^o W$) intraseasonal variance of extratropical Z500 anomalies. The number in each dot corresponds to the model number given in Table 1. The red dots are five models with strongest domain-averaged intraseasonal variance of Z500 and blue dots are the five models with the smallest variance. In Figure 6.5, models with higher MJO skill tend to also be the models showing stronger intraseasonal Z500 variance. A similar but

less strong relationship is found when we replace the intraseasonal Z500 variance with daily Z500 variance (appendix Figure A2) since a large portion of the total variance is determined by the intraseasonal variation. Even if a model is characterized by strong intraseasonal Z500 variance, it does not necessarily indicate it is coming from MJO activity. Thus, to ensure that the relationship in Figure 6.5 is truly due to tropical MJO variability, a similar double-blind test as done for the reanalysis is repeated with the CMIP5 dataset.

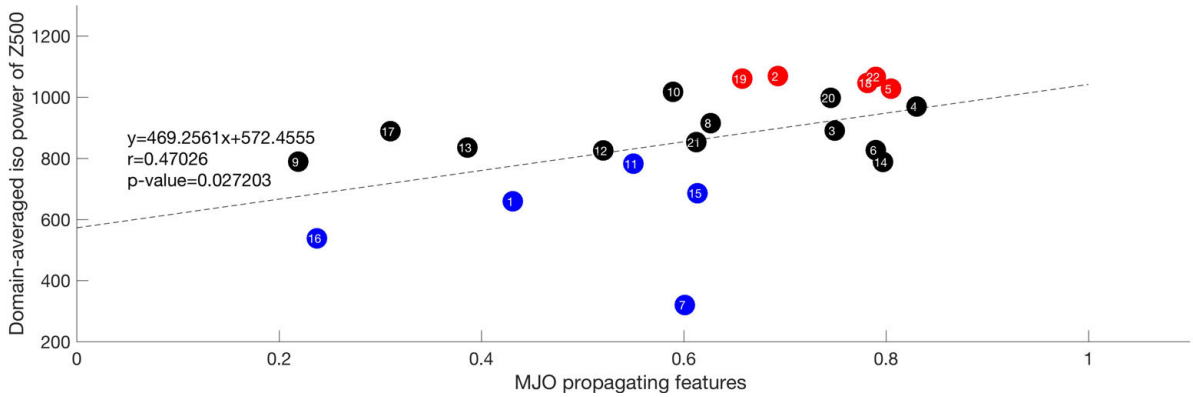

Fig. 6.5. The domain-averaged ($20^o N - 80^o N$,$150^o E - 120^o W$) intraseasonal variance of the extratropical Z500 versus the MJO simulation skills. The number in each dot corresponds to the model number given in table 1.

For each CMIP5 model simulation, we calculate the first 3 leading EOFs of the daily Z500 in the extratropical Pacific and North America region. To identify which leading EOF is associated with the model's MJO, we first calculate the composite PCs from each model as a function of MJO phase and time lag as done in Figures 6.1b and 6.2b for the reanalysis. Based on these composite PCs, the EOF characterized by the strongest composite PC amplitude (averaged over all phases and lags) is selected as the model's leading mode of variability modulated by the model's MJO. Additional analysis confirms that using the top 3 EOFs is enough to capture each model's MJO teleconnection.

We select the top and bottom five models which show the strongest intraseasonal Z500 variance (red and blue dots in Figure 6.5, respectively). Figure 6.6 shows the MJO phase-lag-composited PCs of the identified leading EOFs for the top five (upper panel) and bottom five (lower panel) climate models. For the top five models with the largest intraseasonal z500 variance (upper panel), almost every model shows a tilted two-stripe pattern, which is similar to what we found in observations. However, in the models with small intraseasonal Z500 variance (lower panel), the tilting stripe patterns are absent, showing instead either a vertical stripe (e.g. CanESM2, FGOALS-g2 and GFDL-ESM2M) or small amplitudes (e.g. MIROC-ESM). The vertical stripes indicate that the identified leading mode of extratropical Z500 modulated by the model

MJO shows a timescale longer than the EOF2 in the observations, which is consistent with the model having a nearly stationary MJO (as seen in Figure 6.4).

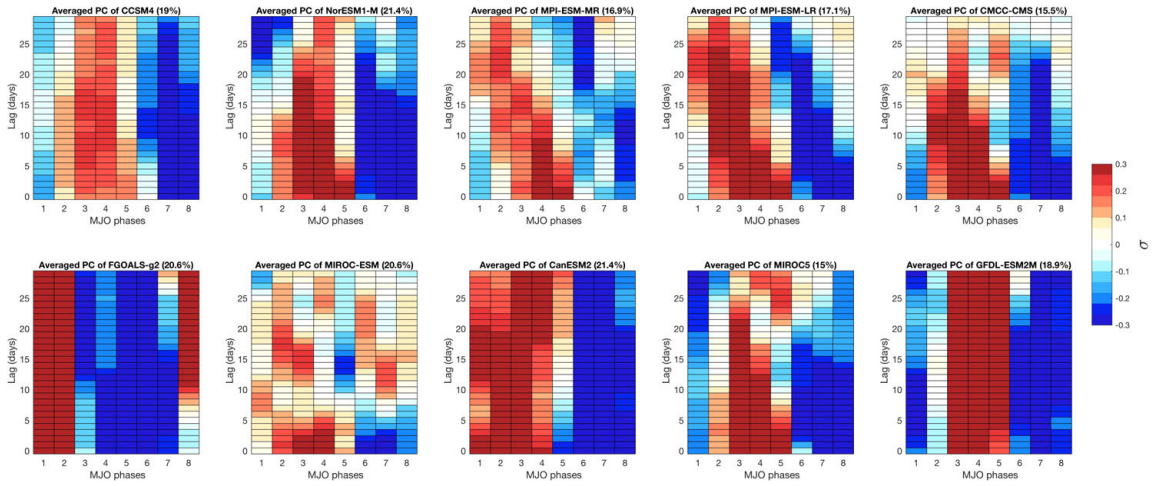

Fig. 6.6. The MJO phase and lag composited PCs of the leading EOFs for five models with strongest intraseasonal Z500 variance (upper panel) and five models with weakest intraseasonal Z500 variance (lower panel).

To further support these model findings, we apply cross-spectrum analysis to the PCs of the daily Z500 EOFs and MJO indices for the different CMIP5 models. Similar to Figure 6.3, two squared-coherence curves can be generated because there are two RMMs. Here, we only show the result of the averaged squared coherence across these two RMMs since the two curves give us similar results. Figure 6.7a displays the mean squared coherence across the five models with the strongest intraseasonal Z500 variance and Figure 6.7b displays the mean squared coherence for the five models with the weakest intraseasonal Z500 variance. The solid line is the multi-model mean and the shading shows the model spread. Similar to reanalysis, the models characterized by strong intraseasonal Z500 variance (Figure 6.7a) show high squared coherence on intraseasonal timescales between the MJO and the leading EOFs of Z500. In contrast, the models with weak intraseasonal Z500 variance (Figure 6.7b) show high squared coherence on the time scales longer than 75 days, indicating a lower-frequency signal. One possible explanation is that the identified leading modes of Z500 are forced by other processes, in addition to the MJO. Regardless, Figures 6.6 and 6.7 support the conclusion that model biases in MJO convection are reflected in the simulated leading modes of extratropical variability.

It is worth mentioning that all of the MJO-influenced extratropical EOFs across all models explain more than 15% of the daily Z500 variance over the North Pacific (shown in parentheses of Figure 6.6), regardless

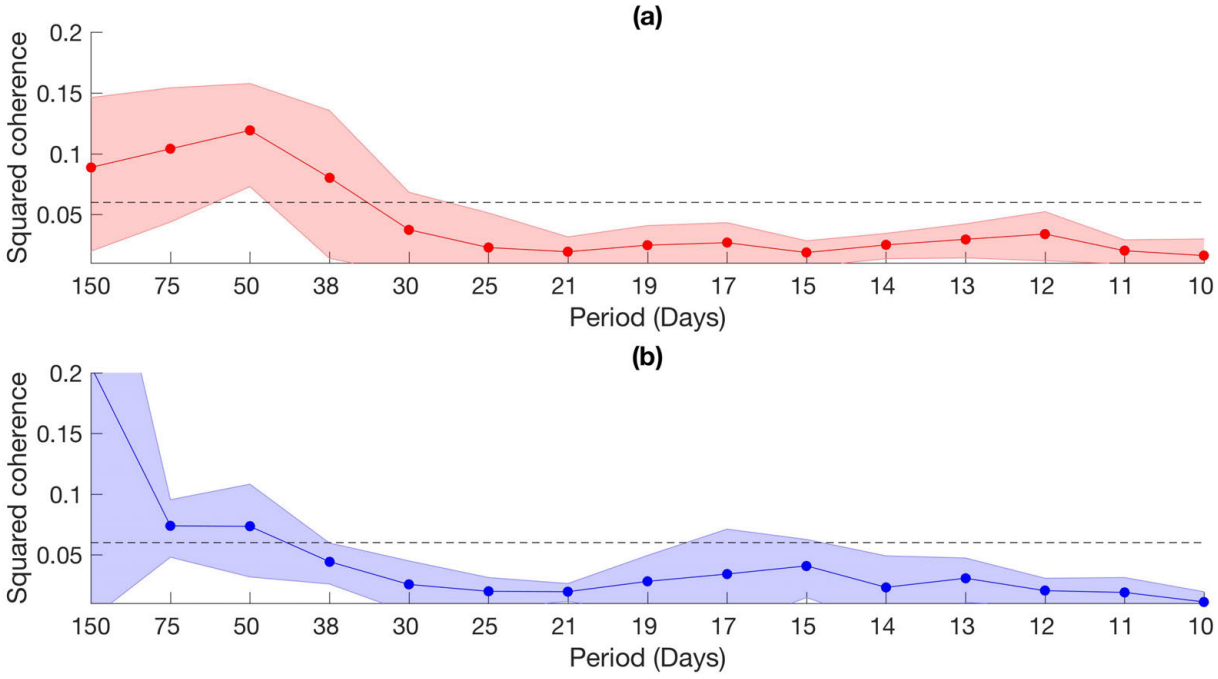

Fig. 6.7. The squared coherence between the PCs of the leading EOFs and the MJO time series. Top figure is for the five models with strongest intraseasonal Z500 variance. Bottom figure is for the five models with weakest intraseasonal Z500 variance. Solid line is the multi-model mean and the shading shows the range of model spread. The dashed line is the 95% cinfidence interval.

of the MJO simulation skill. This indicates that while model biases in MJO simulation can lead to the biases in winter-time extratropical variance, the MJO plays a dominant role in modulating the daily extratropical variations across all CMIP5 models.

6.5 CONCLUSIONS AND DISCUSSIONS

The relationship between the MJO and leading modes of extratropical variability are examined in reanalysis and 22 CMIP5 climate models. We demonstrate that the second leading mode of variability of daily geopotential height is associated with the MJO and can be identified without prior knowledge of the MJO. These results highlight the dominant role of the MJO in driving midlatitude variability. Similar relationships are found in the CMIP5 climate model simulations regardless of MJO convection representation. However, models characterized by higher MJO skill also exhibit larger intraseasonal Z500 variance in the extratropical Pacific and North America. Models characterized by lower MJO skill exhibit decreased intraseasonal variance. Using cross-spectrum analysis, we demonstrate that the well-known model bias of nearly stationary MJO convection is reflected in the simulated leading modes of extratropical variability.

Our results highlight the role of MJO biases in driving biases in extratropical variability within climate models. However, many other processes likely contribute to difference in extratropical variability across models. For example, *Henderson et al.* (2017) demonstrated that even models with well-represented MJO activity can poorly simulate the associated teleconnection patterns due to biases in the basic state circulation. This suggests that to improve the simulations of extratropical weather in climate models, we need to consider both local and remote influence as a whole. These factors associated with possible biases in extratropical basic states are beyond the scope of the analysis in this study and require additional future research.

Table 6.1. CMIP5 models evaluated and the corresponding institutions

	Models	Corresponding Institutions
1	CanESM2	Canadian Centre for Climate Modeling and Analysis
2	CCSM4	National Center for Atmospheric Research
3	CMCC-CESM	Centro Euro-Mediterraneo sui Cambiamenti Climatici
4	CMCC-CM	Centro Euro-Mediterraneo sui Cambiamenti Climatici
5	CMCC-CMS	Centro Euro-Mediterraneo sui Cambiamenti Climatici
6	CNRM-CM5	Centre National de la Recherche Scientifique/Météo-France
7	FGOALS-g2	Institute of Atmospheric Physics, Chinese Academy of Sciences
8	FGOALS-s2	Institute of Atmospheric Physics, Chinese Academy of Sciences
9	GFDL-CM3	NOAA/Geophysical Fluid Dynamics Laboratory
10	GFDL-ESM2G	NOAA/Geophysical Fluid Dynamics Laboratory
11	GFDL-ESM2M	NOAA/Geophysical Fluid Dynamics Laboratory
12	IPSL-CM5A-LR	L'Institute Pieere-Simon Laplace, France
13	IPSL-CM5A-MR	L'Institute Pieere-Simon Laplace, France
14	IPSL-CM5B-LR	L'Institute Pieere-Simon Laplace, France
15	MIROC5	Atmosphere and Ocean Research Institute (AORI), National Institute for Enviromental Studies(NIES), and JAMSTEC, Japan
16	MIROC-ESM	Atmosphere and Ocean Research Institute (AORI), National Institute for Enviromental Studies(NIES), and JAMSTEC, Japan
17	MIROC-ESM-CHEM	Atmosphere and Ocean Research Institute (AORI), National Institute for Enviromental Studies(NIES), and JAMSTEC, Japan
18	MPI-ESM-LR	Max-Planck-Institut für Meteorologie
19	MPI-ESM-MR	Max-Planck-Institut für Meteorologie
20	MPI-ESM-P	Max-Planck-Institut für Meteorologie
21	MRI-ESM-CGCM3	Meteorological Research Institute, Japan
22	NorESM1-M	Norwegian Climate Centre, Norway

CHAPTER 7

Conclusions and Discussions

In this dissertation, we seek to add to the understanding of the role by which the robust MJO teleconnection signals impact the predictions of extratropical circulations. This research starts with a diagnostic metric, pattern consistency, which frames the connection between the robustness of MJO teleconnection signals and the model prediction skill of extratropical geopotential height on subseasonal to seasonal timescales. We show that this diagnostic metric is characterized by a MJO-phase dependent feature, which can be explained by a linear Rossby wave theory. Similar framework can also be used to explain the ENSO-induced interannual variability of MJO teleconnection pattern consistency. In the second half of this dissertation, we explore the application of the concept of MJO teleconnection pattern consistency. A special emphasis is devoted to the influence of past MJO phases on the future state of extratropical circulations, which provides insights into empirical predictions of extratropical weather based on MJO information. At the end of this thesis, we return to a basic but fundamental question: How important the MJO is compared to other drivers of extratropical variability? We enlighten the dominant role of MJO in influencing the extratropical circulations in both climate models output and observations. Due to MJO's strong modulation in the extratropical circulations, we demonstrate the biases in model MJO convection is reflected in the MJO-driven extratropical leading mode.

7.1 PATTERN CONSISTENCY OF MJO TELECONNECTIONS

In chapter 2, the diagnostic metric, pattern consistency, is developed based on the paired pattern correlations, which provides an accessible and approachable way to diagnose the robustness of MJO teleconnection signals. In this study, we demonstrate that MJO convection can produce a robust modulation of extratropical geopotential height in a certain phase/lag (e.g. phase 2/3 lag 10-15 or phase 6/7 lag 10-15). This phase-dependent modulation is reflected in an MJO phase and forecast lead dependence in ECMWF hindcast model ensemble agreements and prediction skills, where higher pattern consistency corresponds to higher ensemble agreements and better prediction skills of extratropical geopotential height.

7.2 DYNAMICS OF MJO TELECONNECTION PATTERN CONSISTENCY

In chapter 3, by employing two sets of perturbed simulations in a linear baroclinic model, we examine why specific MJO phases favor a more consistent teleconnection pattern while others do not. The results indicate that the robustness of MJO teleconnection is a function of MJO phases. Teleconnection patterns during MJO phases 2, 3, 6 and 7 are less sensitive to modest variation of basic states and MJO forcing compared to other phases. This phase-dependent feature can be explained by the constructive (destructive) interference of Robby wave signals emanating from each side of the subtropical jet. Heating location test given in section 3.4.2, indicates the constructive (destructive) interference is present most frequently when MJO heating is characterized by a dipole (symmetric) pattern on each side of the Maritime Continent.

In chapter 4, we explore the key mechanisms determining variability in MJO teleconnection pattern over different ENSO states. By conducting ensemble simulations in a linear baroclinic model with alternately fixing or varying MJO forcing or basic states, the impact of these factors is isolated. We demonstrate the pattern consistency is dramatically decreased during El Niño years compared to ENSO neutral years and La Niña years. From basic state perspective, the southeastward extension of the subtropical jet in El Niño years decreases the poleward propagating Rossby wave signals, which is consistent with the decreased pattern consistency of MJO teleconnection, while the La Niño is characterized by an opposite feature. From the MJO forcing perspective, both El Niño and La Niña year MJO forcing generate a less-dipole like Rossby wave source pattern across the subtropical jet, which reduces the constructive interference by the Rossby signals emanating from both centers and reduces the consistency of MJO teleconnection patterns. Thus, the joint influence from basic states and MJO forcing leads to a dramatic decrease in the pattern consistency during El Niño years while modest change can be found in La Niña years.

7.3 THE ACCUMULATED INFLUENCE OF PAST MJO

In chapter 5, we study the impact of past MJO on future states of extratropical circulations, which provides additional insight into empirical predictions and diagnostic analysis based solely on the present state (e.g. initial state or lag 0) of MJO information. Using both logistic regression models and a linear baroclinic model, the result indicates that approximately 15 additional lags information importantly impact the future states. However, the "additional lags" given above is also characterized by an MJO phase-dependent feature. We find that only phases generate robust MJO teleconnection patterns (e.g. phases 2, 3, 6 and 7) can benefit

the prediction of extratropical circulations, while other phases do not. This can be explained by the nature of logistic regression model, where the model can only learn consistent relationship in the training data.

7.4 THE DOMINANT ROLE OF MJO FOR EXTRATROPICAL CIRCULATIONS

In chapter 6, the importance of MJO compared to other driver of extratropical variability is examined in the observations and 22 climate models. We demonstrate the second leading EOF of the extratropical geopotential height closely co-varies with MJO activities and can be identified without cognizance of any MJO information. This result indicates the dominant role of MJO in influencing extratropical circulations. A similar feature can be found in 22 CMIP5 models regardless of the MJO simulation skills. However, due to this strong relationship between extratropical circulations and MJO, a well-known model biases of stationary MJO convection is also reflected in the simulated leading modes of extratropical variability.

This dissertation thoroughly examines the role of MJO teleconnection pattern consistency from a variety of perspectives. However, a number of unanswered questions still exist. First, all of the theories used in this dissertation are based on linear Rossby wave dynamics. The stationary Rossby wave generated by the MJO forcing can interact with the subtropical jet and change the jet patterns in a short period (e.g. intraseasonal timescales). How does the non-linearity change the results in this dissertation is still an ongoing research. Second, the analysis in chapter 5 uses logistic regression model, which is one of the simplest neural networks. What is unclear, however, is if the phase dependence of results will hold for neural networks with more complicated architectures since the prediction power of neural networks strongly depends on the model architectures.

7.5 FUTURE WORK

Considering that the anthropogenic global warming will likely be continued in the coming decades, it is of great interest to the research and forecast community to understand the possible changes in MJO teleconnections as well as the MJO teleconnection patten consistency in a warmer climate. As the climate warms, it is anticipated that both the behavior of MJO convection and the basic state in the tropics and extratropics will change. From the basic state perspective, an ENSO-like warming pattern is projected in a number of climate models(*Takahashi2011 et al.* 2011), which is characterized by southeastward extension of subtropical jet (*Neelin et al.* 2013) and higher static stability (*Wolding et al.* 2017). From the MJO forcing perspective, the MJO convection is expected to be taller due to higher tropopause (*Chang et al.* 2015; *Wolding et al.* 2017) and the MJO phase speed is projected to be faster based on linear moisture

wave framework(*Adames et al.* 2017; *Rushley et al.* 2019). Studying how the joint influence from all of these factors on the consistency of MJO teleconnection can provide tangible, societally relevant benefits in both short and long terms. Insights gained from this future work will help guide current effort aimed at understanding the mechanism in determining the subseasonal to seasonal prediction in the future.

REFERENCES

Adames, Á. F., and D. Kim (2016), The MJO as a dispersive, convectively coupled moisture wave: Theory and observations *J. Atmos. Sci.* 73, 913–941.

Adames, A. F., D. Kim, A. H. Sobel, A. Del Genio, and J. Wu, 2017: Characterization of moist processes associated with changes in the MJO with increasing CO2. *J. Adv. Model. Earth Syst*., **9**, 2946–2967.

Ahn, M.-S., and Coauthors, 2017: MJO simulation in CMIP5 climate models: MJO skill metrics and process-oriented diagnostics. *Climate Dyn*., **49**, 4023–4045.

Baggett, C. F., E. A. Barnes, E. D. Maloney, and B. D. Mundhenk (2017), Advancing atmospheric river forecasts into subseasonal-to-seasonal time scales *Geophys. Res. Lett.* 44, 7528–7536

Baggett, C. F., K. M. Nardi, S. J. Childs, S. N. Zito, E. A. Barnes, and E. D. Maloney, 2018: Skillful Five Week Forecasts of Tornado and Hail Activity, *J. Geophy. Res.-Atmos*., **123**, 12,661–12,675.

Berggren, R., B. Bolin, and C.-G. Rossby (1949), An aerological study of zonal motion, its perturbations and break-down *Tellus* 1, 14–37

Bjerknes, J., 1969: Atmospheric Teleconnections from the Equatorial Pacific. *Mon. Weather. Rev*., **97**, 163—172

Black, R. X., 1997: Deducing Anomalous Wave Source Regions during the Life Cycles of Persistent Flow Anomalies. *J. Atmos. Sci*., **54**, 895—907

Cassou, C., 2008: Intraseasonal interaction between the Madden-Julian oscillation and the North Atlantic Oscillation. *Nature*, **455**, 523–527

Chang, C.-W. J., W.-L. Tseng, H.-H. Hsu,N. Keenlyside, and B.-J. Tsuang (2015),The Madden-Julian Oscillation in awarmer world, *Geophys. Res. Lett*.,**42**,6034–6042

Chen, F., and J. Dudhia (2001), Coupling an advanced land surface–hydrology model with the Penn State–NCAR MM5 modeling system. Part I: Model implementation and sensitivity *Mon. Wea. Rev.* 129, 569–585.

Ching, L., C.-H. Sui, and M.-J. Yang (2010), An analysis of the multiscale nature of tropical cyclone activities in June 2004: Climate background *J. Geophys. Res. Atmos.* 115.

Christiansen, B., 2019: Analysis of Ensemble Mean Forecasts: The Blessings of High Dimensionality. *Mon. Wea. Rev*., **147**, 1699–1712

Dee, D. P., and Coauthors, 2011: The ERA-Interim reanalysis: configuration and performance of the data assimilation system. *Quart. J. Roy. Meteor. Soc*., **137**, 553—597

De Souza, E. B., and T. Ambrizzi, 2006: Modulation of the intraseasonal rainfall over tropical Brazil by the Madden-Julian oscillation. *Int. J. Climatol*., **26**, 1759–1776.

Fauchereau, N., B. Pohl, and A. Lorrey, 2016: Extratropical Impacts of the Madden–Julian Oscillation over New Zealand from a Weather Regime Perspective. *J. Clim*, **29**, 2161–2175

Ferranti, L., T. N. Palmer, F. Molteni, and E. Klinker, 1989: Tropical-Extratropical Interaction Associated with the 30–60 Day Oscillation and Its Impact on Medium and Extended Range Prediction. *J. Atmos. Sci*., **47**, 2177—2199

Flatau, M. and Y. Kim, 2013: Interaction between the MJO and Polar Circulations. *J. Clim*, **26**, 3562–3574

Gill, A. E., 1980: Some simple solutions for heat-induced tropical circulation. *Quart. J. Roy. Meteor. Soc*., **106**, 447–462

Hamill, T. M., and G. N. Kiladis (2014), Skill of the MJO and Northern Hemisphere blocking in GEFS medium-range reforecasts. *Mon. Wea. Rev.* 142, 868–885.

Held, I. M., S. W. Lyons, and S. Nigam, 1988: Transients and the Extratropical Response to El Niño. *J. Atmos. Sci*., **142**, 163–174.

Henderson, S. A., E. D. Maloney, and E. A. Barnes (2016), The influence of the Madden–Julian oscillation on Northern Hemisphere winter blocking *J. Clim* 29, 4597–4616.

Henderson, S. A., E. D. Maloney, and S.-W. Son (2017), Madden-Julian oscillation Pacific teleconnections: The impact of the basic state and MJO representation in general circulation models *J. Clim*

Henderson, S. A., and E. D. Maloney, 2018: The impact of the Madden-Julian Oscillation on high-latitude winter blocking during El Niño-Southern oscillation events. *J. Clim*., **31**, 5293–5318.

Hendon, H. H., and M. L. Salby (1994), The life cycle of the Madden-Julian Oscillation *J. Atmos. Sci.* 51, 2225–2237.

Hendon, H. H., B. Liebmann, M. Newman, J. D. Glick, and J. Schemm (2000), Medium-range forecast errors associated with active episodes of the Madden–Julian oscillation *Mon. Wea. Rev.* 128, 69–86

Hendon, H. H., C. Zhang, and J. D. Glick, 1999: Interannual Variation of the Madden–Julian Oscillation during Austral Summer. *J. Clim*., **12**, 2538—2550.

Hendon, H. H., M. C. Wheeler, and C. Zhang, 2007: Seasonal Dependence of the MJO–ENSO Relationship. *J. Clim*, **20**, 531–543

Hirota, N., and M. Takahashi, 2012: A tripolar pattern as an internal mode of the East Asian summer monsoon. *Climate Dyn.*., 39, 2219–2238.

Hoskins, B. J., and D. J. Karoly (1981), The steady linear response of a spherical atmosphere to thermal and orographic forcing. *J. Atmos. Sci.* 38, 1179–1196

Hoskins, B.J. and T. Ambrizzi, 1993: Rossby Wave Propagation on a Realistic Longitudinally Varying Flow. *J. Atmos. Sci.*, **50**, 1661–1671

Hsu, H.-H., 1996: Global View of the intraseasonal Oscillation during Northern Winter. *J. Clim.*, **9**, 2386–2406

Hung, M., J. Lin, W. Wang, D. Kim, T. Shinoda, and S.J. Weaver, 2013: MJO and Convectively Coupled Equatorial Waves Simulated by CMIP5 Climate Models. *J. Clim*, **26**, 6185–6214

Infanti, J. M., and B. P. Kirtman (2016), North American rainfall and temperature Prediction response to the diversity of ENSO. *Climate Dyn.* 46, 3007–3023.

Jiang, X., et al. (2015), Vertical structure and physical processes of the Madden-Julian oscillation: Exploring key model physics in climate simulations, *J. Geophys. Res. Atmos.*, **120**, 4718–4748.

Jin, F., 1997: An Equatorial Ocean Recharge Paradigm for ENSO. Part I: Conceptual Model. *J. Atmos. Sci.,* **54**, 811–829

Jin, F.-F., L.-L. Pan, and M. Watanabe, 2006: Dynamics of Synoptic Eddy and Low-Frequency Flow Interaction. Part I: A Linear Closure. *J. Atmos. Sci.*, **63**, 1677–1694

Jin, F.-F., J. Boucharel, and I.-I. Lin (2014), Eastern Pacific tropical cyclones intensified by El Niño delivery of subsurface ocean heat *Nature* 516, 82–85.

Kanamori, H., T. Yasunari, and K. Kuraji, 2013: Modulation of the Diurnal Cycle of Rainfall Associated with the MJO Observed by a Dense Hourly Rain Gauge Network at Sarawak, Borneo. *J. Clim.*, **26**, 4858–4875

Karoly, D.-J., : Rossby wave propagation in a barotropic atmosphere. *Dyn. Atmos. Ocean.*., **7**, 111–125

Kiladis G. N., J. Dias, K. H. Straub, M. C. Wheeler, S. N. Tulich, K. Kikuchi, K. M. Weickmann, M. J. Ventrice (2014), A comparison of OLR and circulation based indices for tracking the MJO. *Mon. Wea. Rev.* 128, 1697–1715

Kim, B.-M., G.-H. Lim, and K.-Y. Kim (2006), A new look at the midlatitude–MJO teleconnection in the Northern Hemisphere winter *Quart. J. Roy. Meteor. Soc.* 132, 485–503

Kim, J.-H., C.-H. Ho, H.-S. Kim, C.-H. Sui, and S. K. Park, 2008: Systematic Variation of Summertime Tropical Cyclone Activity in the Western North Pacific in Relation to the Madden–Julian Oscillation. *J. Clim.*, **21**, 1171–1191.

Kim, H., D. Kim, F. Vitart, V.E. Toma, J. Kug, and P.J. Webster (2016), MJO propagation across the Maritime Continent in the ECMWF ensemble prediction system *J. Clim* 29, 3973–3988

Kimoto, M., F.-F. Jin, and M. Watanabe, 2001: Zonal—eddy coupling and a neutral mode theory for the Arctic Oscillation. *Geophys. Res. Lett*., **28**, 737—740

Lawrence, D. M., and P. J. Webster, 2002: The Boreal Summer Intraseasonal Oscillation: Relationship between Northward and Eastward Movement of Convection. *J. Atmos. Sci*., **59**, 1593–1606.

Liebmann, B., H. H. Hendon, and J. D. Glick, 1994: The Relationship Between Tropical Cyclones of the Western Pacific and Indian Oceans and the Madden-Julian Oscillation. *J. Meteor. Soc*., **72**, 401–412.

Lin, H. (2018). Predicting the dominant patterns of subseasonal variability of wintertime surface air temperature in extratropical northernhemisphere. *Geophys. Res. Lett* ,45, 4381–4389

Madden, R. A., and P. R. Julian, 1971: Detection of a 40—50 Day Oscillation in the Zonal Wind in the Tropical Pacific. *J. Atmos. Sci*., **28**, 702—708.

Maloney, E. D., and D. L. Hartmann, 2000: Modulation of hurricane activity in the gulf of mexico by the madden-julian oscillation. *Science*., **287**, 2002–2004.

Masato, G., B. Hoskins, and T. J. Woollings (2012), Wave-breaking characteristics of midlatitude blocking. *Quart. J. Roy. Meteor. Soc.* 138, 1285–1296

Matthews, A. J., B. J. Hoskins, and M. Masutani, 2004: The global response to tropical heating in the Madden-Julian oscillation during the northern winter. *Quart. J. Roy. Meteor. Soc*., **130**, 1991-–2011.

Moon, J.-Y., B. Wang, and K.-J. Ha (2011), ENSO regulation of MJO teleconnection *Climate Dyn.* 37, 1133–1149

Moore, A. M., and R. Kleeman, 1999: Stochastic forcing of ENSO by the intraseasonal oscillation. *J. Clim*, **12**, 1199–1220.

Mori, M., and M. Watanabe, 2008: The Growth and Triggering Mechanisms of the PNA: A MJO–PNA Coherence. *J. Meteor. Soc. Japan*., **86**, 213—236

Mundhenk, B. D., E. A. Barnes, and E. D. Maloney, 2016: All-Season Climatology and Variability of Atmospheric River Frequencies over the North Pacific. *J. Clim*., **29**, 4885–4903.

Mundhenk, B. D., E. A. Barnes, E. D. Maloney, and C. F. Baggett, 2018: Skillful subseasonal prediction of atmospheric river activity based on the Madden-Julian oscillation and the Quasi-Biennial oscillation. *npj. Clim. Atmos. Sci.,* **1**.

Neelin, J.D., B. Langenbrunner, J.E. Meyerson, A. Hall, and N. Berg, 2013: California Winter Precipitation Change under Global Warming in the Coupled Model Intercomparison Project Phase 5 Ensemble. *J.*

Climate, **26**, 6238—6256

North, G.R., T.L. Bell, R.F. Cahalan, and F.J. Moeng, 1982: Sampling Errors in the Estimation of Empirical Orthogonal Functions. *Mon. Wea. Rev.*, **110**, 699–706

Peatman, S. C., A. J. Matthews, and D. P. Stevens (2015), Propagation of the Madden–Julian oscillation and scale interaction with the diurnal cycle in a high-resolution GCM *Climate Dyn.* 45, 2901–2918

Pohl, B. and A.J. Matthews, 2007: Observed Changes in the Lifetime and Amplitude of the Madden–Julian Oscillation Associated with Interannual ENSO Sea Surface Temperature Anomalies. *J. Clim.,* **20**, 2659–2674

Rushley, S.S., D. Kim, and A.F. Adames, 2019: Changes in the MJO under Greenhouse Gas–Induced Warming in CMIP5 Models. *J. Clim.*, **32**, 803–821

Rienecker, M. M., M. J. Suarez, R. Gelaro, R. Todling, J. BacmeisterE. Liu, M. G. Bosilovich, S. D. Schubert, L. Takacs, G. Kim, S. Bloom, J. Chen, D. Collins, A. Conaty, A. da Silva, W. Gu, J. Joiner, R. D. Koster, R. Lucchesi, A. Molod, T. Owens, S. Pawson, P. Pegion, C. R. Redder, R. Reichle, F. R. Robertson, A. G. Ruddick, M. Sienkiewicz, and J. Woollen (2011),Merra: NASA's Modern-Era Retrospective Analysis for research and applications *J. Clim.*, **24**, 3624–3648

Rodionov, S.N., J.E. Overland, and N.A. Bond, 2005: The Aleutian Low and Winter Climatic Conditions in the Bering Sea. Part I: Classification. *J. Clim*, **18**, 160–177

Sardeshmukh, P.-D. and B.-J. Hoskins, 1988: The Generation of Global Rotational Flow by Steady Idealized Tropical Divergence. *J. Atmos. Sci.*, **45**, 1228–1251

Seo, K.-H., and H.-J. Lee (2017), Mechanisms for a PNA-like teleconnection pattern in response to the MJO *J. Atmos. Sci.* 74, 1767–1781

Simmons, A. J., J. M. Wallace, and G. W. Branstator, 1983: Barotropic Wave Propagation and Instability, and Atmospheric Teleconnection Patterns. *J. Atmos. Sci.*, **40**, 1363—1392.

Slade, S.A. and E.D. Maloney, 2013: An Intraseasonal Prediction Model of Atlantic and East Pacific Tropical Cyclone Genesis. *Mon. Wea. Rev.*, **141**, 1925–1942

Son, S., Y. Lim, C. Yoo, H.H. Hendon, and J. Kim (2017), Stratospheric Control of the Madden–Julian Oscillation. *J. Clim* 30, 1909–1922

Souza, E. B., and T. Ambrizzi, 2006: Modulation of the intraseasonal rainfall over tropical Brazil by the Madden–Julian oscillation. *Int. J. Climatol.*, **26**, 1759–1776.

Sui, C.-H., and K.-M. Lau, 1992: Multiscale Phenomena in the Tropical Atmosphere over the Western Pacific. *Mon. Weather Rev.*, **120**, 407—430.

Takahashi, C., N. Sato, A. Seiki, K. Yoneyama, and R. Shirooka, 2011: Projected future change of MJO and its extratropical teleconnection in East Asia during the northern winter simulated in IPCC AR4 models. *SOLA*, **7**, 201–204, doi:10.2151/sola.2011-051

Taylor, K.E., R.J. Stouffer, and G.A. Meehl, 2012: An Overview of CMIP5 and the Experiment Design. *Bull. Amer. Meteor. Soc*., **93**, 485–498

Tseng, K. -C., E. A. Barnes and E. D. Maloney, 2018: Prediction of the midlatitude response to strong Madden-Julian oscillation events on S2S timescales. *Geophys. Res. Lett*., **45**, 463–470.

Tseng, K., E. Maloney, and E. Barnes, 2019: The Consistency of MJO Teleconnection Patterns: An Explanation Using Linear Rossby Wave Theory. *J. Clim*., **32**, 531–548

Vitart, F., and F. Molteni (2010), Simulation of the Madden–Julian oscillation and its teleconnections in the ECMWF forecast system *Quart. J. Roy. Meteor. Soc.* 136, 842–855

Vitart, F. (2014), Evolution of ECMWF sub-seasonal forecast skill scores *Quart. J. Roy. Meteor. Soc.* 140, 1889–1899

Vitart, F., et al. (2017), The subseasonal to seasonal (S2S) prediction project database *Bull. Am. Meteorol. Soc.* 98(1), 163-173

Waliser, D. E., K. M. Lau, W. Stern, and C. Jones (2003), Potential predictability of the Madden–Julian oscillation. *Bull. Amer. Meteor. Soc.* 84, 33–50

Wallace, J. M., and D. S. Gutzler (1981), Teleconnections in the geopotential height field during the Northern Hemisphere winter *Mon. Wea. Rev.* 109, 784–812

Watanabe M., and M. Kimoto, 2000: Atmosphere-ocean thermal coupling in the North Atlantic: A positive feedback. *Quart. J. Roy. Meteor. Soc*., **126**, 3343-–3369

Watanabe, M., and F.-F. Jin, 2004: Dynamical Prototype of the Arctic Oscillation as Revealed by aNeutral Singular Vector. *J. Clim*., **17**, 2119-–2138.

Wolding, B. O., E. D. Maloney. S. A. Henderson, and M. Branson, 2017: Climate Change and the Madden-Julian Oscillation: A Vertically Resolved Weak Temperature Gradient Analysis. *J. Adv. Modeling Earth Sys*., **9**, doi:10.1002/2016MS000843.

Wheeler, M.C., H.H. Hendon, S. Cleland, H. Meinke, and A. Donald, 2009: Impacts of the Madden–Julian Oscillation on Australian Rainfall and Circulation. *J. Clim*, **22**, 1482–1498,

Wheeler, M.C. and H.H. Hendon, 2004: An All-Season Real-Time Multivariate MJO Index: Development of an Index for Monitoring and Prediction. *Mon. Wea. Rev*., **132**, 1917–1932

Wilks, D. S. (2016), Statistical methods in the atmospheric sciences. Elsevier, 676 pp

Yanai, M., S. Esbensen, and J.-H. Chu, 1973: Determination of Bulk Properties of Tropical Cloud Clusters from Large-Scale Heat and Moisture Budgets. *J. Atmos. Sci*., **30**, 611—627

Yoo, C., S. Lee, and S. B. Feldstein, 2012: Mechanisms of Arctic Surface Air Temperature Change in Response to the Madden–Julian Oscillation. *J. Clim*., **25**, 5777-–5790

Zhang, C. and J. Ling, 2017: Barrier Effect of the Indo-Pacific Maritime Continent on the MJO: Perspectives from Tracking MJO Precipitation. *J. Clim*., **30**, 3439–3459

APPENDIX

Additional information for logistic regression model, CMIP5 analysis and area-weighted pattern correlation

A1 DETAILED DESCRIPTIONS ABOUT LOGISTIC REGRESSION

In this appendix, we provide detailed descriptions about logistic regression model used in chapter 5. The contents in this appendix include (1) loss function (2) regularization and (3) gradient descent optimizer.

$$J_\tau = \frac{1}{m}\sum_{i=1}^{m}[-y_{i,\tau}^{true} \times log(sign(Z500)_{i,\tau}^{predict}) - (1-y_{i,\tau}^{true}) \times log(1-sign(Z500)_{i,\tau}^{predict})] \quad \text{(A1)}$$

J_τ is the "loss" of the logistic regression model, y_τ^{true} denotes the actual (true) value of $sign(Z500)_{i,\tau}^{predict}$, and the summation shows that J_τ is derived as an average over m events. Smaller values of J_τ indicate a better model, i.e.a model with lower loss and higher prediction skill. The advantage of using cross entropy is that the loss (i.e. J_τ) grows exponentially if the model incorrectly predicts the logistic value, providing a larger penalty than the root mean square error.

Regularization is a technique used to prevent a trained model from over-fitting, which ultimately reduces the error for unseen (out of sample) data. Regularization most often involves adding an additional term to the loss function, as shown below.

$$\begin{aligned} J_\tau = \frac{1}{m}\sum_{i=1}^{m}[&-y_{i,\tau}^{true} \times log(sign(Z500)_{i,\tau}^{predict}) - (1-y_{i,\tau}^{true}) \times log(1-sign(Z500)_{i,\tau}^{predict})] \\ &+ \frac{\lambda}{2m}(w_{OMI1_0}^2 + w_{OMI2_0}^2) \end{aligned} \quad \text{(A2)}$$

Equation A2 is nearly identical to Equation A1 except that it includes an additional term, the regularization term. λ is a positive value (to be explained later in the appendix), and $w_{OMI1_0,\tau}$ and $w_{OMI2_0,\tau}$ are the regression coefficients shown in Equation A1. The regularization term is always positive or zero, with larger values of $w_{OMI1_0,\tau}$ and $w_{OMI2_0,\tau}$ leading to a larger loss J_τ. Thus, this regularization term ensures that the coefficients remain small, reducing the chance of over-fitting. However, a model with too large a regularization term will force the regression coefficients to near-zero, resulting in a poor predictive model.

We use "gradient descent" to optimize our model to identify the best coefficients for prediction, and the proper amplitude of regularization (i.e. λ). Although gradient descent is the common method for training

neural networks, we include its formulation here for completeness. Specifically, the regression coefficients and bias unit are updated during the training process as follows:

$$
\begin{aligned}
w_{OMI1_0,\tau}^{(j+1)} &= w_{OMI1_0,\tau}^{(j)} - \eta \frac{\partial J_\tau}{\partial w_{OMI1_0,\tau}^{(j)}} \\
w_{OMI2_0,\tau}^{(j+1)} &= w_{OMI2_0,\tau}^{(j)} - \eta \frac{\partial J_\tau}{\partial w_{OMI2_0,\tau}^{(j)}} \\
b_\tau^{(j+1)} &= b_\tau^{(j)} - \eta \frac{\partial J_\tau}{\partial b_\tau^{(j)}}
\end{aligned}
\tag{A3}
$$

The superscript $j+1$ indicates the $(j+1)$th step of the training, or updating of the coefficients. The most right hand terms are the gradients of the loss function with respect to the coefficients and bias. The minus signs represents the down gradient direction, specifying that the coefficients should be updated in the direction to reduce the loss. η is the learning rate parameter, which indicates the amount to adjust the coefficients with each iteration.

The gradients of the loss function can be analytically derived by plugging equation A2 into equation A3:

$$
\begin{aligned}
w_{OMI1_0,\tau}^{(j+1)} &= (1-\eta\frac{\lambda}{m}) w_{OMI1_0,\tau}^{(j)} - \eta \frac{1}{m} \sum_{i=1}^{m} (sign(Z500)_{i,\tau}^{predict} - y_{i,\tau}^{true}) w_{OMI1_0,\tau}^{(j)} \\
w_{OMI2_0,\tau}^{(j+1)} &= (1-\eta\frac{\lambda}{m}) w_{OMI2_0,\tau}^{(j)} - \eta \frac{1}{m} \sum_{i=1}^{m} (sign(Z500)_{i,\tau}^{predict} - y_{i,\tau}^{true}) w_{OMI2_0,\tau}^{(j)} \\
b_\tau^{(j+1)} &= b_\tau^{(j)} - \eta \frac{1}{m} \sum_{i=1}^{m} (sign(Z500)_{i,\tau}^{predict} - y_{i,\tau}^{true}) b_\tau^{(j)}
\end{aligned}
\tag{A4}
$$

Using equation A4, one can iteratively train the logistic regression model to optimize the regression coefficients and the bias term. We train over our training set 40 times (40 epochs), and additionally perform 20 cross validation cycles (i.e. resample our data 20 times) for the training and testing sets. Each training set contains 2/3 of the total data and the rest is used as the testing set. The final loss for a given model is defined as the average loss for the testing data sets over all 20 cross validations.

As noted previously, when we increase the number of input variables, the logistic regression model is more likely to get into the condition of overfitting. Thus, a regularization term is used in this study. Here, we use logistic regression models with $k = -20$ and others like $k = 0$ and τ spanning from 0 to 30 in equation 4 to demonstrate how the amplitude of regularization influences models' prediction skill.

The choice of the regularizaiton term λ must be chosen before the final training of the model. Figure A1 shows the loss (cross entropy) of the logistic regression model for $k = -20$ averaged over lags 0-30 for 20 different epochs as a function of the regularization term for one particular grid point. Error bars

denote plus/minus one standard deviation of the cross entropy across the 20 training/testing sets. Results for other values of k are similar, and so we only show results for $k = -20$ here. Figure A1 shows that the average loss has a local minimum when $(1-\eta\frac{\lambda}{m}) = 0.75$ (or $\eta\frac{\lambda}{m} = 0.25$) and higher loss function on both ends. This behaviour is consistent with the previous discussion that too large or too small of a regularization term can degrade the performance of the predictive model. Thus, we choose the regularization term that leads to the minimum loss, namely $1-\eta\frac{\lambda}{m} = 0.75$. The models in other extratropical regions exhibit similar dependencies on λ (not shown).

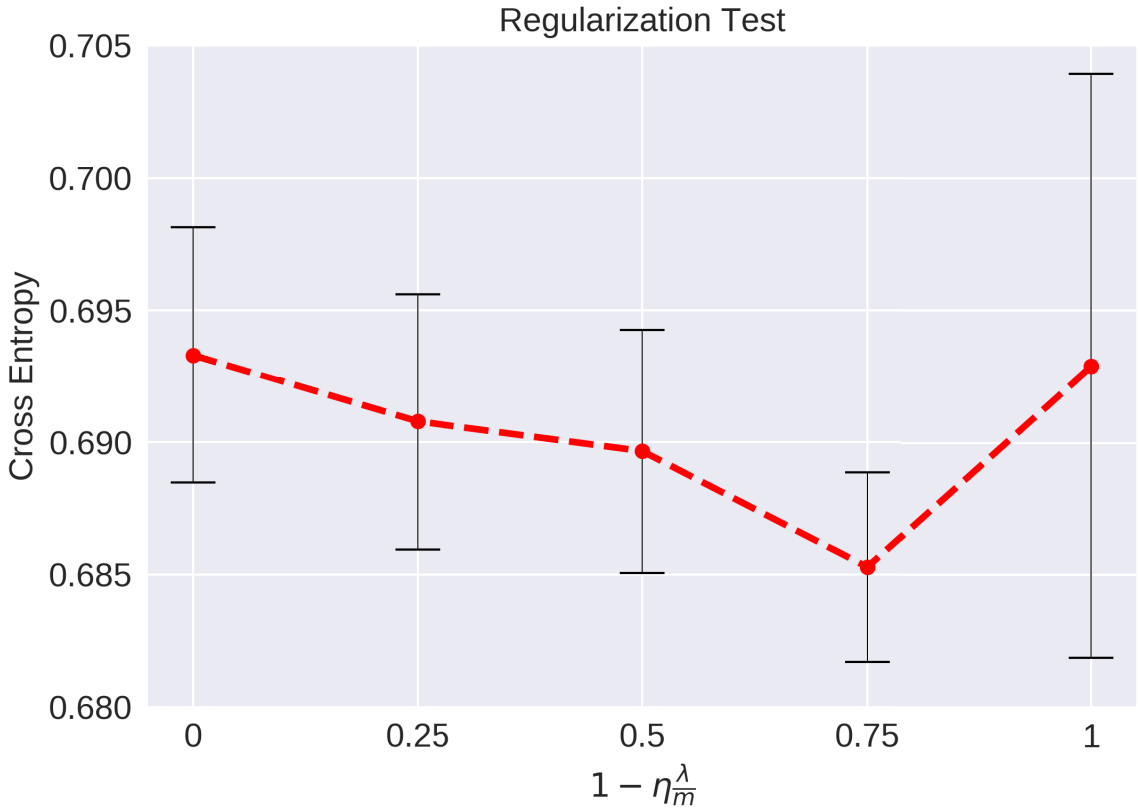

Fig. A1. The average loss (cross entropy) of the logistic regression model for $k = -20$ averaged over lags 0-30 for 20 different training/testing sets as a function of the regularization term. This example is for the model at the grid point $150^o E$ and $70^o N$. Error bars denote plus/minus one standard deviation across the 20 training/testing sets.

A2 THE MJO SKILL SCORES VS TOTAL Z500 VARIANCE

In this appendix, we quantify the relationship between MJO skill scores and the extratropical geopotential height variance. The result is shown in Figure A2. In Figure A2, the total Z500 variance is derived by averaging the variance of Z500 over the regions of 20^oN-80^oN,150^oE-120^oW and over the whole time series from 1950 to 2004. The definition of MJO skill scores is identical to Figure 6.5. The result of Figure A2 is similar to Figure 6.5 except the correlation coefficient is smaller than the correlation coefficient in Figure 6.5.

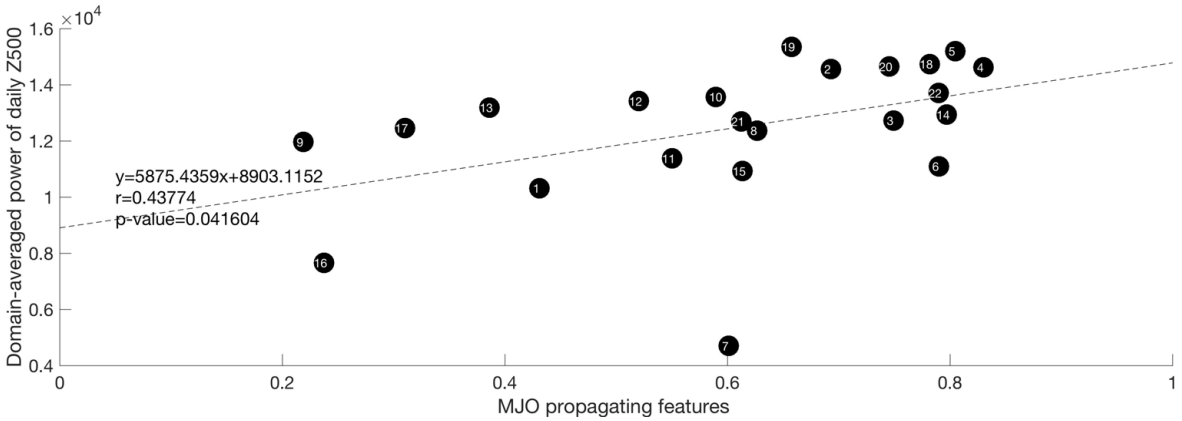

Fig. A2. The domain-averaged (20^oN-80^oN,150^oE-120^oW) total variance of the extratropical Z500 versus the MJO simulation skills. The number in each dot corresponds to the model number given in table 6.1.

A3 AREA-WEIGHTED PATTERN CORRELATION

In this appendix, the formulation for the area weighted pattern correlation (used in chapter 2, 3 and 4) is provided. For two given MJO events i,j, the area-weighted correlation, $\rho_{i,j}$, follows the formulation of A5.

$$\rho_{i,j} = \frac{\sum_k Z500_{i,k} \times Z500_{j,k} \times cos(\phi_k)}{\sum_k [\sqrt{Z500_{i,k} Z500_{i,k} cos(\phi_k)}] \sum_k [\sqrt{Z500_{j,k} Z500_{j,k} cos(\phi_k)}]} \tag{A5}$$

Where the subscript k indicates the value of Z500 anomaly in kth location and the corresponding latitude is ϕ_k.